EXPERIMENTAL AND COMPUTATIONAL INVESTIGATION OF METABOLIC DEMANDS ON NEURONAL RESPONSES TO FOCUSED ULTRASOUND STIMULATION

by

Monica La Russa Gertz

A Dissertation
Submitted to the
Graduate Faculty
of
George Mason University
in Partial Fulfillment of
The Requirements for the Degree
of
Doctor of Philosophy
Neuroscience

Committee:

_____	Dr. J. Robert Cressman, Dissertation Committee Chair
_____	Dr. Kim Blackwell, Committee Member
_____	Dr. Parag Chitnis, Committee Member
_____	Dr. Nathalia Peixoto, Committee Member
_____	Dr. Saleet Jafri, Department Chairperson
_____	Dr. Donna M. Fox, Associate Dean, Office of Student Affairs & Special Programs, College of Science
_____	Dr. Fernando R. Miralles-Wilhelm, Dean, College of Science
Date: _____	Fall Semester 2020 George Mason University Fairfax, VA

Experimental and Computational Investigation of Metabolic Demands on Neuronal Responses to Focused Ultrasound Stimulation

A Dissertation submitted in partial fulfillment of the requirements for the degree of Doctor of Philosophy at George Mason University

by

Monica La Russa Gertz
Bachelor of Science in Chemistry
George Mason University, 2011

Director: John Robert Cressman, Associate Professor
College of Science

Fall Semester 2020
George Mason University
Fairfax, VA

DEDICATION

This is dedicated to the strong and courageous women of my family: My beloved great aunt Anatilde Ruiz Alvarado, who has been my support since the day I was born, and who taught me everything I know about perseverance and ingenuity. My mother, Irma Concepción González who gave me the very best that she could, and my grandmother María Ruiz Alvarado who gave me the love and warmth needed to thrive. But especially to my great grandmother María de Jesús Alvarado Siva, who sacrificed her health and safety to ensure that her children had a better life than she did, and who instilled a strong sense of dedication, love and kindness in them that was later bestowed onto me.

ACKNOWLEDGEMENTS

I thank my advisor, Dr. John Robert Cressman for his guidance and amazing support in writing this dissertation. I also thank my committee members: Dr. Kim (Avrama) Blackwell for her excellent guidance and feedback in neuroscience and all other aspects of this PhD process, Dr. Parag Chitnis for his mentorship in acoustics, and Dr. Nathalia Peixoto for her mentorship in neural engineering. I especially thank my beloved husband Michael Gertz for his patience and endless support of my studies as well as for the time he spent copy editing this manuscript and bringing food to my desk so that I could keep working. I also thank my son Alexander Gertz for being the best lab assistant ever. Finally, I am grateful to the National Science Foundation Graduate Research Fellowship Program for granting me the funding to pursue this degree. Without it, this may not have been possible.

TABLE OF CONTENTS

Page

LIST OF TABLES

LIST OF FIGURES

LIST OF EQUATIONS

LIST OF ABBREVIATIONS

Acoustic Radiation Force ..... ARF
Action Potential ..... AP
Blood-Brain Barrier ..... BBB
Central Nervous System ..... CNS
Compound Action Potential ..... CAP
Deionized ..... DI
Electroencephalogram ..... EEG
Electromyography ..... EMG
Electron Transport Chain ..... ETC
Fetal Bovine Serum ..... FBS
Fluorinated Ethylene Propylene ..... FEP
Focused Ultrasound ..... FUS
Food and Drug Administration ..... FDA
Functional Magnetic Resonance Imaging ..... fMRI
Graphical User Interface ..... GUI
High-Intensity Focused Ultrasound ..... HIFU
Horse Serum ..... HS
Institutionally Approved Animal Care and Use ..... IACUC
Interstimulus Interval ..... ISI
Local Field Potential ..... LFP
Long-Term Potentiation ..... LTP
Mechanical Index ..... MI
Micro-Electrode Array ..... MEA
National Institutes of Health ..... NIH
Non-Invasive Brain Stimulation ..... NIBS
Peripheral Nervous System ..... PNS
Phosphate Buffer Saline ..... PBS
Poly-D-lysine ..... PDL
Polyoxymethylene ..... POM
Polyvinyl Chloride ..... PVC
Post-Stimulus Time Histogram ..... PSTH
Pt(II) Octaethyl Porphine Ketone ..... PtOEPK
Pulse Duration ..... PD
Pulse Repetition Frequency ..... PRF
Temporal Interference ..... TI
Tetrahydrofuran ..... THF
Thermal Index ..... TI
Tone Burst Duration ..... TBD
Tone Burst Interval ..... TBI
Transcranial Alternating Current Stimulation ..... tACS

Transcranial Direct Current Stimulation.....tDCS
Transcranial Electric Stimulation .....tES
Transcranial Magnetic Stimulation..... TMS
Transcranial Random Noise Stimulation.....tRNS
Transmission Duration..... TD

ABSTRACT

EXPERIMENTAL AND COMPUTATIONAL INVESTIGATION OF METABOLIC DEMANDS ON NEURONAL RESPONSES TO FOCUSED ULTRASOUND STIMULATION

Monica La Russa Gertz, Ph.D.

George Mason University, 2020

Dissertation Committee Chair: Dr. John Robert Cressman

Focused ultrasound (FUS) presents the ability to non-invasively modulate neuronal activity with greater resolution and penetration than other methods, making it an attractive mode of stimulation both in basic research and clinically. Yet no one has investigated the local metabolic demands of neuronal response to FUS. Subtle changes in metabolism have profound effects on neuronal activity ranging from enhanced excitability to quiescence. Understanding the metabolic landscape of neuronal stimulation can lead to enhanced methods of modulation including greater safety and efficacy. This dissertation presents the first experiments characterizing ionic and metabolic responses to increased energy demands in acoustic stimulation of neuronal tissue. It also presents a novel model of neuronal tissue that incorporates conductance-based membrane dynamics with electric, diffusive, volumetric, and metabolic dynamics. The model investigates the coupling between these mechanisms and acoustic radiation force as a source of neuronal

response to acoustic stimulation with respect to energy dissipation and ionic redistribution in cellular electrochemical gradients. We performed extracellular measurements of potassium and oxygen in response to both electrical and acoustic stimulation, then validated the model against the experimental results. The experiments revealed a disparity between oxygen and potassium changes in response to FUS and electrical stimulation, indicating different metabolic demands between both modalities. We further applied model predictions to modulate neuronal responses to electrical stimulation ultrasonically, yielding a statistically significant pulse repetition frequency-dependent increase in local field potentials. Additionally, our computational model indicates that ionic redistribution due to acoustic radiation force is largely responsible for the observed effects, thereby opening a new avenue of investigation for mechanisms.

CHAPTER ONE: A BRIEF OVERVIEW OF THE BIOLOGICAL EFFECTS OF FOCUSED ULTRASOUND

Introduction

Brain stimulation techniques that provide precise neural manipulation of individual cells or of specific brain areas with high spatial resolution, are vital tools to elucidate neurological processes ranging in scale from entire systems, down to cellular levels. These techniques range from highly invasive methods for use purely in basic science to non-invasive methods with translational potential to the clinical setting. Between these two major divisions, there is a near inverse relationship between the level of target specificity and the degree of invasiveness. Finding safe, non-invasive methods of brain stimulation with high specificity is paramount to propelling basic studies of neural function in both animal models and healthy humans, thereby increasing the translation potential of this field, and bringing new therapies to the beside faster.

Invasive brain stimulation techniques

Invasive methods, such as optogenetics (Boyden, 2011), targeted micro-stimulation (Histed, Bonin, & Reid, 2009), and pharmacological intervention via local injection (Amiez, Joseph, & Procyk, 2006) work well in animal models. However, these methods are not translatable to human studies. Though deep brain stimulation has been effective for the treatment of diseases such as Parkinson's and epilepsy in the clinical setting (Perlmutter & Mink, 2006), it is also not a viable option for probing neural function in healthy subjects (Blackmore, Shrivastava, Sallet, Butler, & Cleveland, 2019).

Non-invasive brain stimulation tools

Methods of non-invasive brain stimulation (NIBS) (Polanía, Nitsche, & Ruff, 2018) are highly desirable tools to investigate neural activity and brain function in healthy humans. The two mainstays of NIBS in both clinical and basic studies are transcranial electric stimulation (tES) (Polanía et al., 2018) and transcranial magnetic stimulation (TMS) (Walsh & Cowey, 2000). tES comprises several different techniques including transcranial direct current stimulation (tDCS) (Nitsche et al., 2008), alternating current stimulation (tACS) (Herrmann, Rach, Neuling, & Strüber, 2013) and random noise stimulation (tRNS) (Terney, Chaieb, Moliadze, Antal, & Paulus, 2008) (Reed & Cohen Kadosh, 2018). All tES techniques involve the delivery of weak currents through the brain between external electrodes on the scalp. Whereas TMS is based on electromagnetic induction and uses a magnetic coil to produce electric currents inside the brain.

Though tES and TMS are both considered safe methods, they have limitations. Both methods produce highly diffuse electric fields that affect multiple biologically distinct regions of the brain resulting in low spatial resolution, even if the electrode size is reduced (DaSilva et al., 2015). TMS has multiple configurations including ring, figure-8 and H-coil that provide different resolutions. Yet all three configurations still produce diffuse fields, with volumes on the order of several cm^3, that decay exponentially from the brain surface and are therefore limited to the cortical surface. (Deng, Lisanby, & Peterchev, 2013), though the H-coil may provide potential for stimulating deeper brain

targets (Zangen, Roth, Voller, & Hallett, 2005). Moreover, TMS is further limited by patient discomfort associated with some protocols (Rossi et al., 2009).

A third, and more recent, electrically-based NIBS modality, is temporal interference (TI). TI can stimulate neurons at greater depth in the brain without activating tissue at the surface, using multiple high-frequency electric fields that only cause neural activation at intersecting points, where the interference delivers a lower frequency stimulus at the appropriate range required to stimulate neurons (Grossman et al., 2017). Though this technique can potentially be scaled for human application, to date it has only been demonstrated in mice (S. Lee, Lee, Park, & Im, 2020). This brings us to focused ultrasound as an ideal non-invasive method with high spatial resolution that is already in clinical use for non-stimulatory procedures.

What is FUS and how has it been used?

Focused ultrasound (FUS) is a method based on the transduction of sound waves above the range of human detection that can non-invasively deliver mechanical forces, in the form of an acoustic pressure wave, to cells deep within the body. Depending on the specific parameters used, its application to living tissue can induce numerous thermal and mechanical biological effects (bioeffects) (Haar, 2010). Though sound is defined as waves of compression and rarefaction propagated through an elastic medium, FUS is analogous to light passing through a magnifying glass, where incident beams of sound can be focused deeply and precisely within tissue using an acoustic lens. With this method, the diameter of the focal area can be large or small, depending on the design of the lens and the driving frequency. Moreover, bioeffects can be produced only at the

focal point where the beams converge. The individual beams passing through tissue outside of the focal point leave the tissue intact, yielding numerous and extensive bioeffects with high spatial resolution and specificity as compared to other non-invasive methods.

FUS was first used in the brain to thermally ablate a discrete area of tissue to form a lesion (W. J. Fry, Barnard, Fry, Krumins, & Brennan, 1955). Thermal ablation uses high-intensity focused ultrasound (HIFU) to permanently destroy a region of tissue. It can be used to treat neurological disorders, such as essential tremors in Parkinson's disease (Lipsman, Mainprize, Schwartz, Hynynen, & Lozano, 2014; Wang, Dallapiazza, & Elias, 2015), or brain cancers (Martin et al., 2014). However, in pulsed mode, FUS can be used in combination with auxiliary agents to open the blood-brain barrier (BBB) (Hynynen, McDannold, Sheikov, Jolesz, & Vykhodtseva, 2005; McDannold, Arvanitis, Vykhodtseva, & Livingstone, 2012; Sheikov, McDannold, Sharma, & Hynynen, 2008) and locally deliver therapies ranging from small molecule drugs (Treat et al., 2007) to viral vectors (Alonso et al., 2013). HIFU has also been used for pharmacological neuromodulation of specific brain targets (Airan et al., 2017). Though much of the current clinical work is in the area of tissue ablation and drug delivery, there is growing interest in using FUS to reversibly modulate neural activity in the central nervous system (CNS) and peripheral nervous system (PNS) (Focused Ultrasound Foundation, 2016).

FUS in neuromodulation

At lower intensities FUS can directly modulate neuronal activity (Khraiche, Phillips, Jackson, & Muthuswamy, 2008; Tufail et al., 2010; Tyler et al., 2008a) without

the use of any additional agents and may offer alternative approaches to existing methods of neuromodulation. However, some of the main barriers to the incorporation of FUS as a neuromodulatory tool in clinical settings include: 1) understanding the mechanisms underlying the transduction of acoustic waves into neuronal activity; 2) the safety of the platform both thermally and mechanically; 3) targeted delivery of FUS; and 4) monitoring to ensure successful targeting (Blackmore et al., 2019).

General Mechanisms

While the exact mechanisms of neuromodulation via FUS are not fully understood, a general overview of potential mechanisms underlying the actions of ultrasound on neuronal excitability is provided in this chapter.

The bioeffects produced by FUS interactions with tissue can be attributed to two main mechanisms: mechanical and thermal. Though the mechanical effects of focused ultrasound are thought to dominate neuromodulation, there is also evidence of neuromodulation at temperatures below the thermal ablation threshold. The biological outcomes of these thermal and mechanical effects are determined by the tissue characteristics and the acoustic parameters of FUS, which will be discussed in greater detail later in this chapter (Focused Ultrasound Foundation, 2016; Tyler, 2011).

Mechanical Mechanisms

The most prominent mechanical contributors to neuromodulation are: acoustic radiation force (ARF) and cavitation; both of which are well studied topics (Dalecki, 2004; Mike D. Menz et al., 2019). Here, we provide a brief overview of the key parameters.

Acoustic Radiation Force.

ARF is a physical phenomenon that results when an acoustic wave interacts with an obstacle placed along its path. In general, the force exerted on the obstacle is evaluated by integrating the acoustic radiation pressure from the sonic wave over its time-varying surface. In tissue, attenuation removes the momentum of the wave resulting in a net force on the tissue (Palmeri & Nightingale, 2011).

Cavitation.

Acoustic cavitation is the generation of bubbles within tissue as the rarefaction phase of the acoustic wave exceeds a threshold (Plesset & Prosperetti, 1977). Cavitation occurs when the changes in pressure, due to the traveling sound waves, create oscillating points of rarefaction and compression in the tissue. If the magnitude of these changes is high enough or oscillations are slow enough, dissolved gasses will come out of solution to form bubbles in the tissue (Focused Ultrasound Foundation, 2016; Tyler, 2011). The threshold for acoustic cavitation depends on the peak negative pressure, frequency and duration of the FUS beam, and is also sensitive to the tissue properties. The pulsed mode of FUS deposits very low energy into the tissue resulting in very little heat dissipation. However, the pulsing effect will also create large pressure changes in the tissue that can induce cavitation.

The phenomenon is divided into stable and inertial cavitation. Stable cavitation can be described as the sustainable oscillation of bubble size as the pressure changes at the focal point which can result in acoustic emissions, jetting, and streaming (Coussios & Roy, 2008; Focused Ultrasound Foundation, 2016; Thomas, Farny, Coussios, Roy, &

Holt, 2005). The continuous oscillating pressure of a bubble against the cell membrane can increase membrane permeability or induce intracellular responses resulting in a bioeffect (Focused Ultrasound Foundation, 2016). Inertial cavitation is the rapid growth and violent collapse of bubbles that results in tissue destruction (Focused Ultrasound Foundation, 2016). Though inertial cavitation has some clinical applications, it is something to be avoided in the case of neuromodulation (Focused Ultrasound Foundation, 2016). One way to avoid large pressure changes is by increasing the frequency. By decreasing the time spent in negative pressure, there is a decreased probability that dissolved gas will come out of solution to form bubbles resulting in cavitation. This will be described in greater detail in the safety section.

Other factors contributing to mechanical neuromodulation

Acoustic streaming also contributes to mechanically-based bioeffects either alone or in combination with stable cavitation. Acoustic streaming can lead to the formation of microjets that penetrate the membrane, as well as eddies and turbulence that can affect membrane interactions on the surface. Tyler, 2011 proposes a continuum mechanics hypothesis in which ultrasound can, modulate neuronal activity through combinations of pressure, fluid, and membrane interactions in addition to acoustic radiation force. These include Bernoulli effects, and other fluid-dynamics that arise from acoustic impedance mismatches between fluids and tissues of different densities (Tyler, 2011).

Ion channels can contribute to mechanical effects indirectly as well. Nearly all ion channels are mechanically sensitive to some degree, including classic voltage-gated channels. Some neurotransmitter receptors also respond to stretch (Tyler, 2012).

Thermal Mechanisms

Absorption of FUS waves leads to temperature increases at the focal point, which may also result in thermal neuromodulation depending on the incident waveform. The thermal effects are determined by the amount of acoustic energy absorbed by the tissue within a given time window (Focused Ultrasound Foundation, 2016). A focused continuous wave of ultrasound will transfer large amounts of energy to tissue which is then dissipated as heat. The intensity and the duration of the exposure can induce effects ranging from local hyperthermia, which produces low heat using a lower intensity over a long exposure, to thermal ablation which produces enough heat from the high intensity to denature proteins within seconds (Focused Ultrasound Foundation, 2016). Thermal effects of focused ultrasound can also be used to induce neuromodulation. Temperature changes of just a few degrees can affect neural activity, altering the amplitude and duration of action potentials (APs), excitation thresholds, spiking rates and afterhyperpolarization behaviors, (Chapman, 1967; Guttman, 1966; J. C. F. Lee, Callaway, & Foehring, 2005; Thompson, Masukawa, & Prince, 1985). Neuronal signals may also be temporarily suppressed in areas where tissue temperature has been raised slightly. Though the mechanism is not known, it is possibly due impaired protein/lipid interactions. (Focused Ultrasound Foundation, 2016; Tyler, 2011). Certain ion channels are also known to exhibit thermal sensitivity (Cesare, Moriondo, Vellani, & Mcnaughton, 1999).

Factors Affecting Biological Outcomes

The bioeffects produced by these two main mechanisms are dependent on the combination of acoustic parameters and tissue characteristics.

Acoustic Parameters.

Acoustic parameters include: mode (continuous wave versus pulsed), transmission duration, and power. However, frequency and intensity are influencing factors specific to neuronal stimulation versus other tissue types. Depending on the combination of acoustic parameters, FUS can either stimulate or suppress neuronal responses. With respect to tissue characteristics, acoustic impedance, and attenuation of FUS for a given tissue type must also be taken into account when considering how FUS fields affect neuronal response. (Focused Ultrasound Foundation, 2016; Tyler, 2011).

All the parameters are interrelated therefore, a change in one parameter will change the entire output. As described earlier, mode determines primarily (though not necessarily) whether thermal or mechanical effects are induced due to the amount of energy that is deposited in the tissue. Transmission duration can amplify the effects of the mode in conjunction with intensity, which is the rate at which energy passes through the focal point. For example, a continuous wave at a high intensity for a short duration will ablate tissue, versus pulsed waves at high intensity for a short duration will induce a neuronal response. Since power (the rate at which energy is transferred) is a factor of intensity, then assuming the diameter of the focal point is constant, there is a direct relationship between an increase in power and an increase in neuronal response to stimulation (M. D. Menz, Oralkan, Khuri-Yakub, & Baccus, 2013).

Frequency affects both lateral resolution and intensity at the focal point (Ng & Swanevelder, 2011). In order to understand the effects of frequency on these two parameters, some terms must be defined and the process of focusing must be briefly explained (Figure 1). Lateral resolution is high when the near-zone length is long (Ng & Swanevelder, 2011). The near-zone length is the point at which sound beams converge to their narrowest width. Factors that increase near-zone length include: short wavelength (or high frequency, since frequency and wavelength are inversely related), and large aperture (large acoustic lens diameter (D)). The process of focusing creates a focal region within the near zone. Focusing shortens the near-zone length to a value called the focal length. The width of a focused beam is determined by factors in the following equation: Width of focused beam = focal length * wavelength / aperture. Therefore, high lateral resolution as a result of a narrow, focused beam is obtained by: a short focal length, short wavelength (or high frequency) and wide aperture. The higher the lateral resolution, the smaller the cross-sectional diameter of the beam, therefore intensity will increase at constant power (Ng & Swanevelder, 2011). Understanding this relationship, along with the effects of tissue characteristics below, is essential in learning to balance and optimize stimulation parameters that yield high specificity and good physiological responses.

It is important to note that a modulatory acoustic experiment can be comprised of multiple “levels” which have an additive contribution toward the total intensity applied to the tissue. The fundamental unit of an acoustic experiment is the cycle (or period), which is the reciprocal of the central frequency of the transducer measured in (M)Hz. The amount of positive pressure in a cycle is determined by the duty cycle, which is expressed

as a percentage of the total cycle. If using the pulsed mode, pulse duration (PD) is the time in which the pulse is on and is determined by the number of cycles in a pulse. This comprises the first "level" of the experiment (Figure 2). Each pulse can then be repeated a variable number of times at a given frequency. This frequency is the pulse repetition frequency (PRF) also measured in Hz. The length of time it takes to repeat a given number of pulses at this frequency is the tone burst duration (TBD), which is the second "level" of a protocol. The third "level" of a protocol is the transmission duration, which is the total length of the protocol. Here, the tone burst can be repeated a variable number of times at given interval. The interstimulus interval (ISI) is the time between tone bursts, whereas the tone burst interval (TBI) is the sum of the ISI and the TBD. The transmission duration (TD) is the total time for a variable number of TBIs to be repeated.

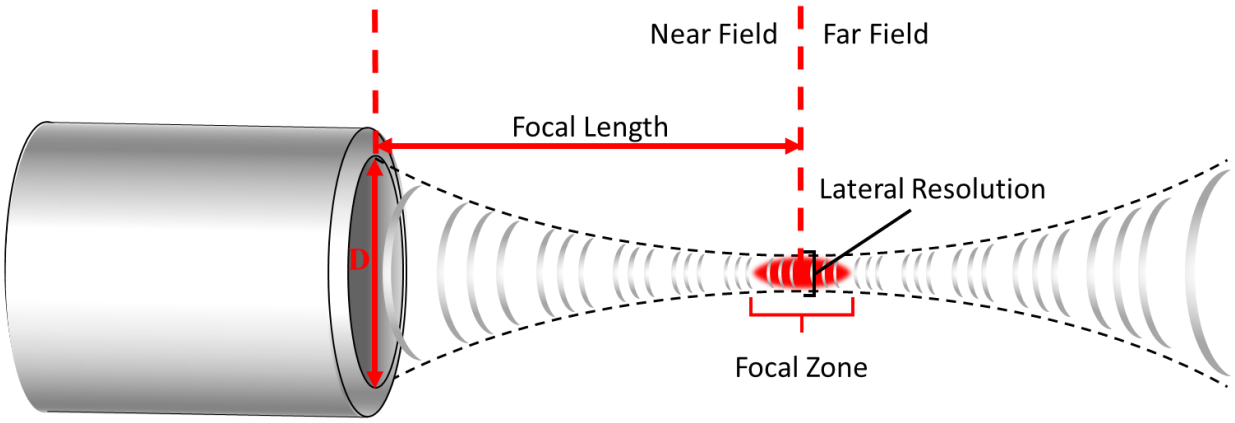

Figure 1: Schematic of the acoustic field generated by a focused ultrasound transducer.

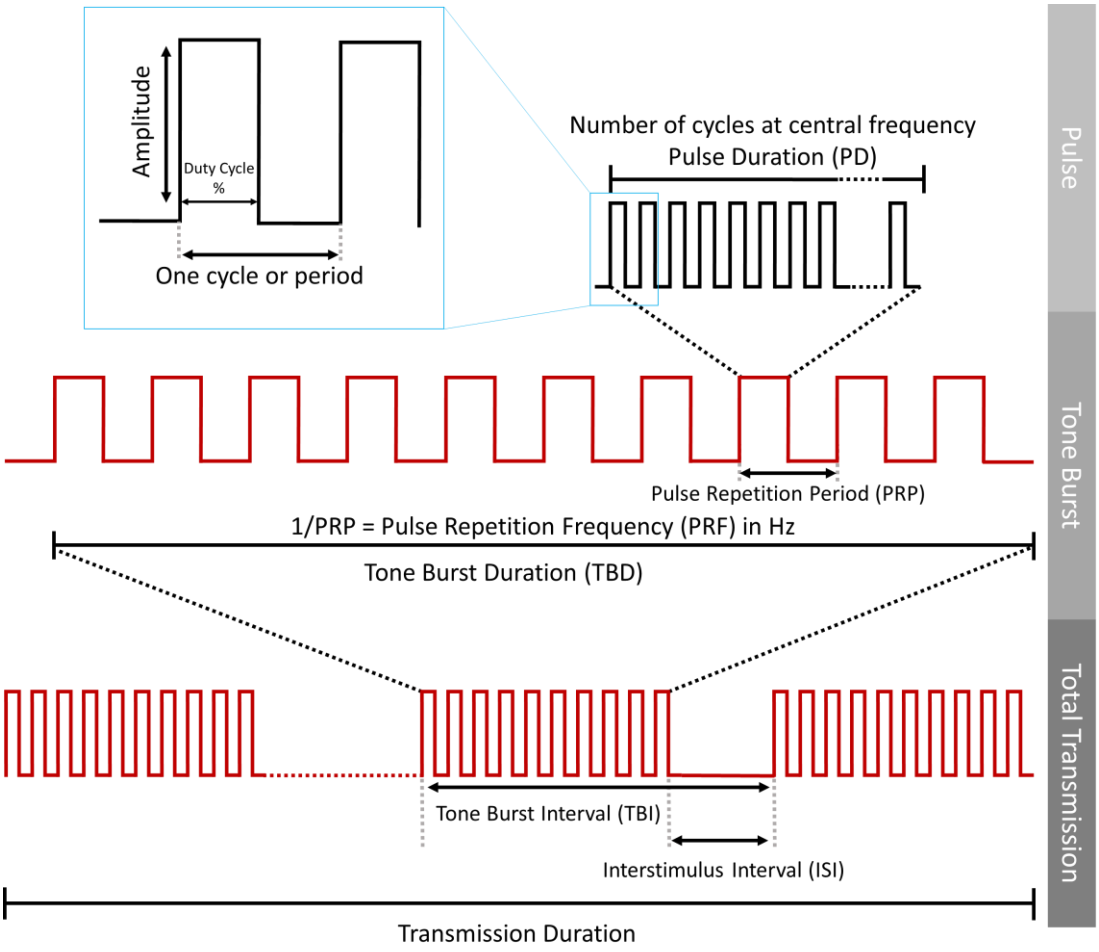

Figure 2: Schematic of Ultrasound Sequences.

Tissue Characteristics.

These include acoustic impedance and attenuation. Acoustic impedance can be considered the product of the tissue density and the speed of sound. An acoustic impedance mismatch is the difference in impedance between two different mediums which establishes a boundary condition (Tyler, 2011). These boundary conditions at cellular interfaces are more susceptible to radiation forces and shear stresses that lead to

acoustic streaming, microjets, turbulence, and Bernoulli effects that are thought to underlie many bioeffects of ultrasound. Attenuation of sound waves at tissue interfaces must also be taken into account. This includes absorption (conversion to heat), reflection and scattering of the sound at tissue boundary conditions, with absorption being the main factor contributing to attenuation (Tyler, 2011).

Applications of FUS

The bioeffects produced by FUS can be divided into three main types of applications: Tissue destruction, targeted drug delivery, and a large group of other applications which includes: vascular interactions, oncotherapies, immunomodulation, stem cell homing, and most pertinent, neuromodulation (Focused Ultrasound Foundation, 2016). This chapter will focus exclusively on neuromodulation.

Prior and Currents Studies in FUS-Based Neuromodulation

Studies have shown that the mechanical and thermal effects of focused ultrasound can reversibly stimulate or suppress neural activity in the central nervous system (CNS) or in the peripheral nervous system (PNS), depending on the acoustic parameters applied.

Central Nervous System.

FUS has been shown to induce both excitatory and suppressive responses in the CNS. Suppressed neural activity was first evoked by Fry, Ades and Fry, 1958; first reversibly, and then permanently, by increasing the intensity. Suppression of activity has also been achieved using pulsed mode to induce spreading depolarization waves in rats (Koroleva, Vykhodtseva, & Elagin, 1986). Furthermore, electrophysiological recordings of local field potential (LFP) by Bachtold *et al.*, 1998, demonstrated both excitation and

suppression of electrically evoked field potentials in hippocampal slices. Bachtold *et al.*, 1998, demonstrated both excitation and suppression of electrically evoked field potentials in hippocampal slices. William J Tyler *et al.*, 2008 elicited action potentials in response to FUS pulses in whole-cell patch clamp recordings of CA1 pyramidal neurons. Experiments on microelectrode arrays of primary hippocampal neurons also induced increased firing rates in response to both single and multiple FUS pulses (Choi et al., 2013; Khraiche et al., 2008; H. B. Kim et al., 2017).

Excitatory responses have also been reported in vivo. (Tufail et al., 2010) demonstrated increased cortical spiking in LFP recordings in response to FUS stimulation of the motor cortex and hippocampus in anaesthetized mice. These responses were also attenuated pharmacologically, consistent with the results from hippocampal slice experiments (Tyler et al., 2008b). Other studies have also stimulated the motor cortex in rodents using motor responses and electromyography (EMG) to quantify the robustness of a response with the goal of determining the most effective range of stimulation parameters (Gulick, Li, Kleim, & Towe, 2017; Han, Kim, Kim, Shin, & Youn, 2018; H. A. S. Kamimura et al., 2016; H. Kim, Chiu, Lee, Fischer, & Yoo, 2014a; King, Brown, Newsome, & Pauly, 2013; King, Brown, & Pauly, 2014; G. F. Li et al., 2016; Mehić et al., 2014a; Ye, Brown, & Pauly, 2016; Yoo, Kim, Min, Franck, & Park, 2011; Younan et al., 2013a). A key finding from these studies is that there is an inverse relationship between EMG response amplitude and carrier frequency in the low MHz range between 0.25 and 0.65 MHz with respect to the threshold intensity required to produce a response (H. Kim, Chiu, Lee, Fischer, & Yoo, 2014b; King et al., 2013; Tufail et al., 2010; Ye et

al., 2016). Two different explanations have been investigated to account for this frequency dependence: cavitation and focal diameter. (Church, Labuda, & Nightingale, 2015) proposed a cavitation-based mechanism as the probability of cavitation is inversely related to frequency. Focal diameter is also inversely related to frequency therefore the volume of stimulated tissue may drive the overall motor response. (M. Menz et al., 2017) presented a model incorporating these two factors. The model showed good agreement with in vivo mouse data consistent with an ARF mechanism, whereby higher frequencies are more effective at inducing a local response but stimulate smaller volumes of tissue and therefore require higher intensities to modulate neuronal responses. Other FUS parameters such as PRF, burst duty cycle, and burst duration have also been investigated. (King et al., 2013) elicited greater responses by increasing the PRF in the range of 100-3000 Hz. Whereas (H. Kim et al., 2014b) obtained the lowest intensity threshold for eliciting a motor response by manipulating the burst duty cycle and burst duration.

There is conflicting evidence in several parameters, including mode, intensity, and frequency. Studies comparing pulsed mode to continuous wave have reported conflicting results with regards to efficacy in producing motor responses (H. Kim et al., 2014b; King et al., 2013). The relationship between stimulation intensity and response rates or magnitude has also been found to be either inverse (Tufail et al., 2010), direct (H. Kamimura et al., 2015; Mehić et al., 2014a), or all-or-none (King et al., 2013). Furthermore, attempts to target specific parts of the motor cortex have produced different muscular responses (G. F. Li et al., 2016).

Different mechanisms exist for coupling acoustic energy into neural activity at different frequencies. For example, in a study by (M. D. Menz et al., 2013) demonstrated that FUS stimulation at much higher frequency (43 MHz) can mediate modulatory effects. Their study evoked strong responses in ganglion cells of isolated salamander retinas in response to FUS stimulation. The responses were inhibited when synaptic transmission was blocked, indicating that FUS responses required synaptic transmission. Cavitation is unlikely at 43 MHz, therefore a mechanism based on ARF may provide a better explanation of the results. Conversely, a study by (Gulick et al., 2017) demonstrated that at 0.2 MHz, motor movements in response to FUS stimulation displayed a 3 s refractory period, indicating that a recovery time was required, which is consistent with a cavitation-based mechanism.

The high variability in many of these studies is likely to involve many different factors including: anatomical differences in animal subjects, differences in experimental setup, and unaccounted or unexpected interactions between different inhibitory and stimulatory networks. Anesthesia is another important factor that has been found to significantly alter experimental results during FUS stimulation. It has been shown that responses can only be evoked under a light state of anesthesia (King et al., 2013; Younan et al., 2013a).

FUS neuromodulation in the CNS has also been studied in humans. The first human study of neuromodulation in the brain by (Hameroff et al., 2013) placed an 8 MHz diagnostic imaging probe over the posterior frontal cortex for 15 s of volunteers who suffered from chronic pain. The subjects reported improvements in mood, but not pain.

At 8 MHz, too much acoustic energy would be attenuated by the skull, therefore subsequent studies preferentially use sub-megahertz frequencies. (Legon et al., 2014b) attenuated induced SEPs in healthy volunteers by stimulating the primary somatosensory cortex (S1) with FUS. Moreover, the study noted improvements in two-point touch and frequency discrimination tasks after FUS modulation. (Mueller, Legon, Opitz, Sato, & Tyler, 2014) also found modulation of both intrinsic and evoked electroencephalogram (EEG) dynamics. This combined body of work demonstrates that FUS can modulate cortical processes in humans non-invasively.

(W. Lee, Chung, Jung, Song, & Yoo, 2016; W. Lee et al., 2015) was able to induce peripheral sensations in volunteers by stimulating either the hand S1, secondary somatosensory cortex, or both areas simultaneously with FUS. Subjects reported perceptions ranging from itching and coolness to tingling and numbness in between the axillary region and the fingertips. The wide range of the induced sensations is likely due to a misalignment of the FUS beam to the target region, which is a prominent problem in scaling studies from smaller animals to humans as was highlighted in another study by (W. Lee, Lee, et al., 2016) which experienced similar problems with misalignment of the FUS to the primary visual cortex of sheep. However, phosphene perception was induced in the participants who received properly focused stimulation which resulted in EEG modulation. Activation of the target site as well as activity in connected visual, and higher order cognitive pathways were also confirmed through simultaneous functional magnetic resonance imaging (fMRI) mapping.

(Ai, Mueller, Grant, Eryaman, & Legon, 2016) also investigated FUS stimulation to cortical and sub-cortical regions in conjunction with simultaneous fMRI and were able to detect cortical activity close to the transducer. Moreover, (Legon, Ai, Bansal, & Mueller, 2018) were also able to suppress SEP components and reduce performance for a two-point discrimination task by targeting of deeper, thalamic regions.

Peripheral Nervous System.

Much work has also been done with respect to FUS neuromodulation in the peripheral nervous system (PNS). Similar to CNS studies, it was also discovered that FUS stimulation of the peripheral nerves could initially increase spiking activity and then depress spontaneous activity first reversibly, then permanently, while conduction velocities increased with the applied acoustic dose (W. J. Fry, Wulff, Tucker, & Fry, 1950; Lele, 1963; Young & Henneman, 1961). (Lele, 1963) was also able to replicate both types of acoustic results by applying heat only, which suggested a thermal mechanism.

Can these FUS effects be used to suppress pain in clinical applications? Studies have shown that differential blocking of mammalian nerves occurs in response to acoustic exposure. C fibers, which carry pain signals from receptors, are the most responsive whereas A-a fibers are the least sensitive (Legon, Rowlands, Opitz, Sato, & Tyler, 2012; Lele, 1963; Young & Henneman, 1961).

Other studies have also confirmed these findings, showing the same pattern of initial increase of evoked potential amplitudes before a subsequent decrease at higher intensities, which have also been attributed to thermal effects (Colucci, Strichartz, Jolesz,

Vykhodtseva, & Hynynen, 2009; Foley, Little, & Vaezy, 2008; Tsui, Wang, & Huang, 2005). However, short pulses that do not produce a significant thermal rise have also been shown to enhance or suppress electrically evoked compound action potentials (CAPs), depending on the time between the acoustic pulse and electrically evoked CAP (Mihran, Barnes, & Wachtel, 1990). The lack of thermal increase along with reductions in conduction velocities suggests a mechanical effect, as conduction velocities are expected to increase with temperature (Juan, González, Albors, Ward, & Irazoqui, 2014; Lele, 1963; Wahab et al., 2012).

ARF and cavitation have both been proposed as mechanisms for FUS modulation of the PNS. (Wahab et al., 2012) showed that cumulative ARF has an inverse relationship with reductions in conduction velocities and AP amplitudes following electrical stimulation via an electrode, whereas (C. J. Wright, Rothwell, & Saffari, 2015; Christopher J. Wright, Haqshenas, Rothwell, & Saffari, 2017) demonstrated in ex vivo crab axons, that de novo APs could only be elicited in the presence of cavitation. (Wahab et al., 2012) also found that the minimum pressure required to induce direct AP generation was 1.8 MPa at 0.67 MHz compare to the lowest pressures required to modulate electrically induced APs (0.1 MPa). An in vivo study in mice by (Downs et al., 2018), also required higher pressures to induce EMG activity and visible muscle responses to acoustic stimulation of the sciatic nerve, where a regeneration interval improved responses to subsequent stimulations. The high pressures with longer recovery times in these studies suggest cavitation as mechanism for generating de novo APs in peripheral nerves.

On the other hand, studies made by Gavrilov et al. propose that ARF is the mechanism behind tactile sensation. Experiments in a mechanoreceptor known as the Pacinian corpuscle, showed AP generation following acoustic exposure, with increasing potential amplitudes as the intensity was increased (Gavrilov, Gersuni, Ilyinsky, Tsirulnikov, & Shchekanov, 1977). This was adapted from their previous human study, in which a range of tactile sensations were elicited by short FUS pulses on the hand or forearm (Gavrilov, Gersuni, Ilyinski, Tsirulnikov, & Shchekanov, 1977).

Safety

Safe use of FUS neuromodulation in the CNS and PNS is critical not only with respect to its future as a non-invasive clinical procedure, but also to ensure the development of relevant basic research that will propel the field forward.

Safety Guidelines and Parameters

The safety of ultrasound in diagnostic imaging has been extensively studied (Duck, 2008). The three main metrics of interest are: intensity, mechanical index (MI) and thermal index (TI). MI is defined as the ratio of peak rarefaction pressure in MPa to the square root of the frequency in MHz (Duck, 1997). It is a measure of the probability of mechanical damage occurring within tissue due to the degree of cavitation produced (Apfel & Holland, 1991). TI is a measure of the temperature change resulting from the energy deposited in the tissue. It is a defined as the ratio of the acoustic power exposed to the tissue (W) to the power required to raise the tissue by 1°C (Wdeg) (Duck, 1997).

With this in mind, the Food and Drug Administration (FDA) guidelines for diagnostic ultrasound imaging devices, are as follows: the I_{SPTA} must not exceed 720

mW/cm2, the I_{SPPA} must not exceed 190 W/cm2, the TI must not exceed 6 and the MI must not exceed 1.9 (Duck, 2007). However, it may be possible to exceed recommended diagnostic MI limit for the purpose of neuromodulation, though not recommended until extensive safety studies have been validated in both CNS and PNS (Blackmore et al., 2019).

Acoustic Parameters

Table 1 and Table 2, adapted from a review by (Blackmore et al., 2019), list the studies in the literature where FUS was used for neuromodulation in the CNS and PNS, respectively, without any exogenous agents, highlighting the key findings along with any reported safety information. Both tables are divided by subject type. Table 1 lists experiments performed in the CNS and Table 2 lists experiments performed in the PNS. Of the studies that reported safety outcomes, most found that there were no adverse effects to the tissue or subject. However, there were some that did report detrimental effects after sonication in either the CNS or PNS. These include: small microhemorrhage for repetitive stimulation in the CNS of sheep (W. Lee, Lee, et al., 2016) and increased levels of damage as intensity increased up to complete axonal degeneration and necrosis in the PNS (rat sciatic nerve) (Foley et al., 2008). Other groups reported additional instances of damage in the PNS including: damage in the mouse sciatic nerve (Downs et al., 2018), morphological changes in myelination development in rat dorsal nerve root, enlargement of periaxonal space, abnormal morphology of nodes of Ranvier, and demyelination (Ellisman, Palmer, & André, 1987) as well as varying levels of damage to the bullfrog sciatic nerve, depending on intensity (Colucci et al., 2009).

Table 1: Ultrasound Neuromodulation Studies in CNS
Adapted from (Blackmore et al., 2019)

Study	Organism & target	Key findings	Safety
Human			
Legon et al. (2018b)	Human (M1)	Combined US and magnetic stimulation. US inhibits amplitude of single-pulse TMS-induced MEPs and reduces reaction times during stimulus response task.	N/A
Legon et al. (2018a)	Human (Thalamus)	Modulation of sub-cortical nuclei. Attenuation of P14 SEP amplitude. Reduction in performance of discrimination task.	N/A
Lee et al. (2016b)	Human (V1)	Phosphene perception. fMRI: activation of V1, visual pathways & cognitive processes. Modulation of VEPs.	Neurological examination, MRI follow up (0, 2, 4 wk) and follow-up interviews (2 mo): no abnormal findings across all participants.
Lee et al. (2016a)	Human (S1, S2)	Elicitation of tactile sensations on hand and arm. Simultaneous S1/S2 stimulation.	No adverse changes or discomfort in mental/physical status across all individuals.
Ai et al. (2016)	Human (M1, S1, caudate)	fMRI responses in sensorimotor & caudate regions.	N/A
Lee et al. (2015)	Human (S1)	Elicitation of peripheral sensations on hand and arm. Modulation of SEPs.	Neurologic and neuroradiologic assessment did

Study	Organism & target	Key findings	Safety
			not show any safety concerns.
Mueller et al. (2014)	Human (S1)	Modulation of EEG dynamics, including phase and phase rate in beta and gamma bands.	N/A
Legon et al. (2014)	Human (S1)	Modulation of SEPs and alpha, beta and gamma frequency bands. Improvement in discrimination tasks.	N/A
Hameroff et al. (2013) *	Human (Posterior frontal cortex)	Improvement in mood scores. Small pain reduction but not significant.	One subject experienced a headache, which quickly resolved. No other side effects up to 4 mo after the study.
Non-Human Primates (NHP)			
Kubanek et al. (2017)	NHP Frontal Eye Field (FEF)	US stimulation to left (right) FEF shifted animals' choices to rightward (leftward) target.	No long-term bias in animals choices after 8 d of stimulation of each region.
Wattiez et al. (2017)	NHP (FEF)	Single neuron recordings in SEF: activity changes following US stimulation of FEF. ~40% of neurons modulated.	N/A
Deffieux et al. (2013)	NHP (FEF)	Increased latencies in antisaccade task.	Stimulation effect was transient (no significant effects observed on the following control trials).
Rodent			
Guo et al. (2018)	Guinea Pig (Various including A1, S1)	US response due to indirect cochlear fluid pathway rather than direct activation. Similar activity in A1, SC1	N/A

Study	Organism & target	Key findings	Safety
		recorded irrespective of target location. US-evoked activity eliminated by removal of cochlear fluid.	
Fisher and Gumenchuk (2018)	Mouse (Cortex)	Reduction in latency and increased Ca 2+ response following electrical stimulation with US pre-treatment.	Histology: no changes in distribution of glial fibrillary acidic protein or evans blue – no neural injury or BBB opening.
Sato et al. (2018)	Mouse (Visual cortex)	Widespread neural activation through indirect auditory mechanism. Contralateral visual cortex had similar response kinetics to targeted side, but auditory cortex showed contralateral bias. Chemical deafening greatly reduced motor outputs.	N/A
Li et al. (2016)	Mouse (Motor cortex)	Increased specificity and decreased latencies at 5 MHz compared with 1 MHz.	Histology (H&E): no evidence of tissue bleeding or cell necrosis.
Kamimura et al. (2016, 2015)	Mouse (Motor & cognitive areas)	Limb movement and eyeball dilation.	Histology (H&E): no damage.
Moore et al. (2015)	Mouse (Somatosensory cortex)	US and optogenetic responses have similar form for pyramidal neurons, but not interneurons, but amplitudes 10- to 20-fold lower for US.	N/A
Ye et al. (2015)	Mouse (Motor cortex)	Success rate decreases with frequency for given intensity. Focal spot size	N/A

Study	Organism & target	Key findings	Safety
		did not have consistent effect on success rates; most of the variance can be explained by frequency. Success strongly correlated with cavitation index and particle displacement but not ARF.	
King et al. (2014)	Mouse (Motor cortex)	Differences in EMG response (magnitude and latency) following rostral or caudal stimulation.	N/A
King et al. (2013)	Mouse (Motor cortex)	EMG motor responses. Anesthesia levels important. CW as effective as pulsed US. All or nothing responses. Responses occur due to stimulus onset (within 30–100 ms). Required intensity increases with frequency. Success rate increases with PRF from 100–3000 Hz. Key variable appears to be integral of amplitude over a time interval of 50 to 150 ms.	N/A
King et al. (2013)	Mouse (Motor cortex)	EMG motor responses. Anesthesia levels important. CW as effective as pulsed US. All or nothing responses. Responses occur due to stimulus onset (within 30–100 ms). Required intensity increases with frequency. Success rate increases with PRF from 100–3000 Hz. Key variable appears to be	N/A

Study	Organism & target	Key findings	Safety
		integral of amplitude over a time interval of 50 to 150 ms.	
Tufail et al. (2010)	Mouse (Motor cortex & hippocampus)	Increased cortical spiking. TTX blocked US-evoked activity. Mean failure rate increased from 0.25–5 MHz. Lower frequencies & I sppas give more robust EMG responses. Evoked potentials in hippocampus followed by 3 s afterdischarge containing gamma, sharp wave ripple oscillations and increase in spike frequency. Increase in BDNF.	No evidence of BBB opening. No change in density of apoptotic glial cells or neurons. No differences in synapse density or cortical neuropil ultra-structure. No neurologic abnormalities during rotorod and wire-hanging tasks.
Han et al. (2018)	Rat (Motor cortex) & Cell cultures	Response robustness increased with intensity and linked with shorter latencies. Ketamine reduced Ca 2+ transients in dose-dependent manner by up to 82%.	Histology (H&E): no obvious damage, morphologic changes, tissue bleeding, or cytoplasmic swelling.
Gulick et al. (2017)	Rat (Motor cortex)	Long-term modulation of electrical stimulation: reduced hind limb responses. Direct motor response had 3 s refractory period.	No behavioral changes observed following stimulation.
Lee et al. (2017)	Rat	–	Histology (H&E, TUNEL assay): no cell necrosis.
Darvas et al. (2016)	Rat	EEG signal at the frequency of the US PRF was induced along with demodulated activity in gamma & beta bands: potential use of US to tag	N/A

Study	Organism & target	Key findings	Safety
		deep regions for EEG-based mapping.	
Yu et al. (2016)	Rat	Localization of induced brain activity using electrophysiologic source imaging.	N/A
Kim et al. (2015)	Rat (Visual cortex)	VEP magnitude suppression/enhancement dependent on intensity and BD. Threshold intensity to elicit response.	N/A
Mehić et al. (2014)	Rat (Motor cortex)	Comparison of planar, focused and modulated-focused source using 1.75 and 2.25 MHz to generate a 0.5 MHz difference frequency. Large variance in responses. Robustness of motor movement scaled with Ispta.	All histology samples showed no damage to brain tissue.
Younan et al. (2013)	Rat	Motor responses: tail, fore and hind limbs, eye, single whisker. Pressure threshold for response dependent on anesthesia levels. Rat skull distributes field across whole brain and introduces pressure hot spots due to reverberations.	No change in behavior or weight was observed.
Yang et al. (2012)	Rat (Thalamus)	Reduction in extracellular GABA for at least 2 h following sonication. No change in glutamate levels.	Histology showed no abnormal findings at either the focus or along the beam path.
Kim et al. (2017)	Ex vivo: Hippocampal slice	Microelectrode Array (MEA): region and threshold-specific increased spike activity	N/A

Study	Organism & target	Key findings	Safety
		during and after US stimulation.	
Yoo et al. (2011b)	Rat (Thalamus)	Reduction in anesthesia times following FUS (up to 20 min).	N/A
Min et al. (2011a)	Rat (Thalamus)	Reduction in EEG theta bursts after epileptic seizure induction.	Histology: no tissue damage (H&E) or DNA fragmentation (TUNEL).
Min et al. (2011b)	Rat (Thalamus)	Increase in extracellular dopamine and serotonin levels for at least 2 h post-sonication.	N/A
Koroleva et al. (1986)	Rat (Cerebral cortex & hippocampus)	Direct current potential changes and spreading depression waves.	N/A
Choi et al. (2013)	in vitro: Rat hippocampal neurons	MEA: increased spiking and bursting. Effect observed post exposure. Largest firing rate at 0.8 MPa, decreased at higher pressures.	N/A
Tyler et al. (2008)	Ex vivo: Hippocampal slices and isolated mouse brain	US-induced APs during whole-cell current clamp recordings in CA1 pyramidal neurons. Triggering of voltage-gated Na + and Ca 2+ channels, vesicle exocytosis and synaptic transmission. Addition of TTX and Cd 2+ blocked Na + and Ca 2+ transients, respectively.	Repeated stimulation (36–48 h) did not alter fine membrane structure.
Khraiche et al. (2008)	in vitro: Hippocampal slices	MEA: US can excite neurons and increase firing rates.	N/A
Bachtold et al. (1998)	Ex vivo: Hippocampal slices	Enhancement and depression of electrically evoked potentials.	N/A

Study	Organism & target	Key findings	Safety
Rinaldi et al. (1991)	Ex vivo: Hippocampal slices	Depression of electrically evoked potentials.	N/A
Miscellaneous			
Prieto et al. (2018)	Cell cultures	Patch clamp recordings: activation of Piezol but not Na V1.2 through membrane stress as a result of acoustic streaming.	N/A
Kubanek et al. (2018)	Caenorhabditis Elegans	MEC-4, a pore-forming subunit expressed in touch receptor neurons required for US-evoked behaviors. TRP-4 response due to background genetic mutation. 50% BDC and 300–1000 Hz PRF produce optimal response rates.	N/A
Ballantine et al. (1960)	Cat (Edinger-Westphal nucleus)	Temporary dilation of eye.	No lesions observed.
Fry et al. (1958)	Cat (LGN)	Reversible suppression of VEPs.	No histologically detectable lesions.
Dallapiazza et al. (2018)	Pig (Thalamus)	Reversible suppression of SEPs. Selective activation of sub-nuclei within somatosensory thalamus.	Histology: no gross or microscopic tissue damage.
Daniels et al. (2018)	Pig (AC)	AEP suppression.	N/A
Yoo et al. (2011a)	Rabbit (Somatomotor & visual areas)	Bimodal modulation: excitation of motor response and suppression of p30 VEP component. EEG signals confirmed by BOLD fMRI.	Histology did not reveal any tissue damage. No TUNEL positive apoptotic cells or VAF positive ischemic cells

Study	Organism & target	Key findings	Safety
			were found. No increase in gadolinium signal, suggesting no BBB disruption.
Menz et al. (2017)	Ex vivo: Isolated salamander retina	US stimulation results in micron-scale displacements. Efficacy increased with frequency, consistent with an ARF-mediated mechanism.	N/A
Menz et al. (2013)	Ex vivo: Isolated salamander retina	US evoked strong response similar to visual response but with shorter latencies. US activated other cells beyond photoreceptors. PRF 15 Hz to 1 MHz had no effect on responses; only temporal-averaged power important.	N/A
Lee et al. (2016c)	Sheep (SM1, V1)	SM1: EMG response of contralateral hind leg. V1: VEPs.	Histology: small microhemorrhage for repetitive stimulation (≥ 500 stimulations delivered at 1 s intervals). Damage not seen at longer ISIs. Post-sonication behavior normal.

Table 2: Ultrasound Neuromodulation in PNS.
Adapted from (Blackmore et al., 2019)

Study	Organism & target	Key findings	Safety
Human			
Lee et al. (2014)	Human (Fingertip)	Induction of different peripheral sensations (thermal, vibrotactile and nociception) depending on US parameters. CW did not induce sensations. Thermal responses maximum over a band of intensities (I_{sppa} = 10–30 Wcm^{-2}), whereas for vibrotactile and nociception, response rate increased with intensity. Greater response rate at 350 kHz than 650 kHz.	No short-term or long-term tissue damage to sonicated finger.
Legon et al. (2012)	Human (Fingertip)	US induced evoked potentials similar to other stimulus modalities. The waveform can be adjusted to preferentially stimulate different fibers (Aβ, Aδ and C) and the subsequent somatosensory neural circuits as confirmed by fMRI.	N/A
Dickey et al. (2012)	Human (Fingertip)	Sigmoidal response rate with increasing intensity. High specificity	No psychological or physiologic changes (assessed by questionnaire).

Study	Organism & target	Key findings	Safety
		(participants ability to determine when US applied) indicates unique tactile sensations induced by US. Response correlates with density of mechanoreceptors.	
Gavrilov et al. (1977a)	Human (Hand, forearm)	Increasing intensity: Tactile, temperature and, finally, pain sensations. At deeper targets, only pain elicited. Longer stimuli (>100 ms), sensations present at start and end of waveform. Temperature sensations dependent on temperature of water bath that hand is immersed in. Cavitation detected before onset of pain sensations.	N/A
Rodent			
Downs et al. (2018)	Mouse (Sciatic nerve)	EMG activity and visible muscle activation for p > 3.2 MPa and BDC > 35%. A break period of 20–30 s improved the next stimulation success rate to 92%. Latencies similar to electrical stimulation.	Histology: no damage detected for successful US stimulation parameters or negative control groups. Damage observed for positive control (5.4 MPa, 90% BDC, 1 kHz PRF, 0.5 s BD) and for PL > 30 ms at 5.7 MPa.

Study	Organism & target	Key findings	Safety
Casella et al. (2017)	Rat (Posterior tibial nerve)	Inhibition of rhythmic bladder contractions. Longer latency and refractory periods compared with electrical stimulation.	N/A
Ni et al. (2016)	Rat (Sciatic nerve)	Improved regeneration and functional recovery following crush injury. BDNF levels increased for first 2 wk following treatment.	N/A
Juan et al. (2014)	Rat (Vagus nerve)	Decrease in electrically evoked CAPs; effect increased in magnitude with I spta. Decrease in conduction velocities.	N/A
Tych et al. (2013)	Rat (Sciatic nerve)	US threshold for paw withdrawal reduced for neuropathic tissue compared with sham surgery tissue.	N/A
Kim et al. (2012)	Rat (Abducens nerve)	Eyeball movement.	Histology (H&E, trypan blue): no damage or BBB disruption.
Foley et al. (2008)	Rat (Sciatic nerve)	Increased reduction in CMAPs with intensity. CMAP amplitude recovered by 28 d in all but highest intensity, which showed no recovery.	Histology: increased levels of damage as intensity increased up to complete axonal degeneration and necrosis.

Study	Organism & target	Key findings	Safety
Ellisman et al. (1987)	Rat (Dorsal nerve roots)	Electron microscope: morphologic changes in rats at myelination development stage (3–5 d old)—enlargement of periaxonal space, abnormal morphology of nodes of Ranvier and demyelination.	See Key Findings.
Miscellaneous			
Gavrilov et al. (1977b)	Cat (Pacinian corpuscle), Frog (Ear labyrinth)	APs induced in Pacinian corpuscle for intensities in range 0.1–4.2 Wcm −2. Amplitude of receptor potentials increased with intensity. Evoked potentials in frog auditory brain at intensities as low as 0.01 W cm −2 similar in shape to sonic stimuli.	N/A
Lele (1963)	Cat, Monkey, Human, Earthworm.	Progressive US dose leads to initial AP amplitude enhancement, then reversible and finally irreversible depression. Conduction velocities increase with dose. Physiologic effects reproduced by heat application.	Enhancement/reversible depression: undistinguishable from unirradiated nerves. Irreversible depression: nodularity, fragmentation of axis cylinders restricted to irradiated section of nerve (indistinguishable from heat damage). Prolonged, intense US irradiation without rise

Study	Organism & target	Key findings	Safety
			in nerve surface temperature without apparent physiologic and anatomic effects.
Young and Henneman (1961)	Cat (Saphenous nerve)	Differential blocking of mammalian nerves. C-fibers most responsive. A-a least sensitive. Reversible and then permanent block with increasing US dose.	N/A
Wahab et al. (2012)	Earthworm (Giant Axon)	Cumulative ARF negatively correlated to reduction in conduction velocity and AP amplitude. At low impulses, enhancement in amplitude before dropping at longer exposure times. Final changes semi-permanent: no recovery within 15 min.	Semi-permanent effects in reduction of AP amplitudes following repeated single pulse sonications 100 times a second for over 200 s.
Wright et al. (2017, 2015)	ex vivo: Crab (Leg nerve axon)	Unpredictable responses with slight preference for first stimulus. Lowest intensity for successful stimulation was 100 Wcm −2 (1.8 MPa) at 0.67 MHz. No responses at 1.1 or 2 MHz. Cavitation signals detected for all successful	N/A

Study	Organism & target	Key findings	Safety
		stimuli; afterdischarge at 230 Wcm −2 resulting in reduced CAPs – probably due to cavitation-induced membrane rupture.	
Colucci et al. (2009)	ex vivo: Bullfrog (Sciatic nerve)	1.986 MHz: reduction in CAP amplitude, thermal effect matched by experiments varying water bath temperature. 0.661 MHz: discrepancy with thermal effects. Pulsed US: initial small increase in CAP then reduction.	Histology (H&E): 1.986 MHz, little or no damage consistent with thermal effects. 0.661 MHz, varying levels of damage depending on intensity. At higher intensities evidence of cavitation.
Tsui et al. (2005)	ex vivo: Bullfrog (Sciatic nerve)	Increased conduction velocity with power. Amplitude increased by 9% at 1 W but then decreased at higher powers.	N/A
Schelling et al. (1994) *	ex vivo: Frog (Sciatic nerve)	CAPs generated similar in shape but lower in amplitude than electrically induced CAPs. Movement away from the focus prevented CAP generation until air bubbles where added.	N/A
Mihran et al. (1990)	ex vivo: Frog (Sciatic nerve)	Latency of applied US results in different responses: enhancement or	N/A

Study	Organism & target	Key findings	Safety
		suppression of electrically induced CAP. Required BD to induce response reduced as intensity increases.	
Fry et al. (1950)	ex vivo: Crayfish (Ventral nerve)	Increased spiking and then reversible depression of spontaneous activity.	N/A

Thermal Effects with Respect to Safety

Though (Lele, 1963) demonstrated that changes in temperature alone were sufficient to induce neuronal modulation in the peripheral nervous system, and several other studies showed the same, most of the recent studies show that temperature rises are negligible (Blackmore et al., 2019; Khraiche et al., 2008; W. Lee, Kim, et al., 2016; Tufail et al., 2010). Therefore, thermal effects are not considered to contribute to FUS neuromodulation. The only caveat is a study by (H. A. S. Kamimura et al., 2016), which reported a temperature rise of 7°C in brain tissue as a result of thermal diffusion from the cranium, indicating that unintentional neuromodulation might occur as a result of heat diffusion from the surrounding bone tissue.

Conclusion

Though much work has been done in the field to date, there are still many inconsistencies and gaps in knowledge that need to be addressed. Equipment, sample preparations, and animal protocols need to be standardized, as they have been in more

established fields such as microbiology and electrophysiology. Mechanisms have been narrowed down to main components such as ARF and cavitation, but the details of how these work, particularly ARF, still elude us. Validated safety parameters specific to neuromodulation are also needed. Many of these gaps can be filled with computational models that can address these needs, and guide future experiments, as we will discuss in the next chapters.

CHAPTER TWO: ENERGY CONSTRAINTS ON NEURONAL STIMULATION

This chapter is the first of two papers that investigate the metabolic demands of neuronal stimulation. We begin here by developing the techniques of simultaneous oxygen and potassium measurements in ex vivo hippocampal slices. We drive the system using electrical stimulation to gain an understanding of neuronal metabolic response to high energy demands and use these results to develop a metabolic module in a computational model that will in turn help to interpret the experimental results.

Abstract

Neuronal systems process information mainly through generation and transmission of action potentials, synaptic transduction, and dendritic summation. These processes are primarily driven by the dissipation of energy stored in the cell's electrochemical gradients, which are in turn, maintained through metabolic mechanisms. Altered gradients can significantly affect cellular function, and ultimately lead to the failure of neuronal signaling, resulting in pathological conditions such as epilepsy. To elucidate the metabolic constraints on neuronal activity, we investigated these both computationally and experimentally. A Hodgkin-Huxley, conductance-based model incorporating ionic dynamics with membrane potential dynamics and metabolic dynamics was validated against experimental results performed in the CA1 region of acute rat hippocampal slices. Extracellular measurements of potassium and oxygen in response to supraphysiological electrical stimulation (2 s duration) at intervals ranging from 1 min to 10 s, revealed two main phenomena: 1) a second steady state for oxygen

after it has reached a maximum level of consumption and 2) a potassium maximum in time that appears at the shortest stimulation interval when the system is being driven hardest. In order to replicate the features of the data the model revealed the existence of an intrinsic activity dependent metabolic shift between neuronal and glial cells, that may work in concert with, or even provide some explanation for the well-known Crabtree effect.

Introduction

Neuronal systems process information mainly through generation and transmission of action potentials, synaptic transduction, and dendritic summation. These processes are primarily driven by the dissipation of energy stored in the cell's electrochemical gradients. In normal signaling, neuronal gradients are reestablished through the phosphorylation of the sodium/potassium pump (Na^+/K^+ ATPase), which results in the conversion of ATP to ADP. However, the brain consumes energy at a rate 10 times faster than the rest of the body, and more than half of this energy is used by Na^+/K^+ ATPase (Baeza-Lehnert et al., 2019; Harris, Jolivet, & Attwell, 2012; Silver & Erecinska, 1994). Moreover, neurons are unique in that they have limited intracellular energy stores but experience acute and unpredictable increases in energy demand (Baeza-Lehnert et al., 2019) which can cause these gradients to become depleted either through excessive increases in energy dissipation, or a loss of energy injection, resulting in pathological conditions. Epileptic seizures are an example in which excessive activity reduces the ability of neuronal cells to reestablish their ionic gradients (Watts, Pocock, & Claudianos, 2018). Whereas hypoxia and hypoglycemia are examples of a loss of energy

injection. In hypoxia, a lack of oxygen decreases the production of ATP via oxidative phosphorylation to the point that the cell can no longer repolarize due to a lack of energy source to drive the Na^+/K^+ ATPase (Mathiesen et al., 2011; Wheaton & Chandel, 2011). Whereas hypoglycemia also results in low ATP production from a lack of glucose (Rehni & Dave, 2018). Because acute energy shortage has such a profound impact on neuronal function, with even small deficits of ATP leading to undesirable consequences, it is not clear how neurons can transition from the resting to active state continuously without undergoing metabolic stress.

The production of ATP used to maintain neuronal gradients is a downstream result of metabolism, which has two main components: glycolysis and oxidative phosphorylation. In the cytosol, glycolysis partially oxidizes glucose anaerobically into pyruvate. The pyruvate generated in this process can experience two fates. It can either enter the mitochondria and be further oxidized aerobically through oxidative phosphorylation in the electron transport chain (ETC), or it can be reduced anaerobically to lactate in the cytosol. The full aerobic oxidation of glucose to CO_2 and H_2O renders 30–32 ATPs (Hinkle, 2005), whereas anaerobic reduction to lactate renders only 2 ATPs.

Interestingly, it has been found that active brain tissue does not fully oxidize glucose but instead generates a local surplus of lactate. This phenomenon is termed “aerobic glycolysis” because excess glycolysis is occurring in the presence of oxygen. Normally, glycolysis is acutely suppressed by mitochondrial oxidative phosphorylation. This is commonly known as the Pasteur Effect, which is a major contributor to the balance between glycolysis and respiration. However, there are two known forms of

aerobic glycolysis: the Warburg Effect and the Crabtree Effect. Though both involve augmented lactate production in response to higher glucose/oxygen consumption ratio, they are mechanistically different (Barros et al., 2020). The Warburg Effect can be interpreted as a deficit in the capacity of mitochondrial activity to inhibit glycolysis. Whereas the Crabtree Effect is the suppression of mitochondrial oxidative metabolism by glycolysis (Barros et al., 2020). A major site of such acute aerobic glycolysis is the astrocyte. It has been proposed that fast aerobic glycolysis observed in the brain may be part of a complex relationship between neurons and astrocytes whereby neurons induce surrounding astrocytes to produce and supply lactate as a substrate, thereby not only increasing local oxygen availability for the neuron, but also shuttling lactate to the neuron for additional oxidative fuel, thus maximizing information processing as seen in Figure 25 (Barros et al., 2020). Moreover, glycolysis and mitochondrial activity have recently been proposed to be synchronized by a non-canonical mechanism involving Na+/K+ ATPase independently of adenine nucleotides and Ca^{2+} (Baeza-Lehnert et al., 2019).

In this study, we utilize the extracellular measurements of potassium and oxygen responses obtained from electrical stimulation experiments performed in the CA1 region of acute rat hippocampal slices to benchmark our Hodgkin-Huxley conductance-based model. In addition to membrane dynamics, our model also incorporates ionic dynamics as well as the metabolic dynamics described here.

We find that experimental results are consistent with our computational model that describes the effect of the non-canonical metabolic relationship between astrocytes and neurons, as well as the regulatory effects of Na^{+}/K^{+} ATPase on this relationship. We

further conclude that this model can be used to elucidate the constraints on neuronal activity in other stimulation modalities.

Results

Simultaneous measurements of oxygen and potassium reveal metabolic relationships in response to increasing stress.

Our experiments were designed to test the limits of the neuronal metabolic response system by simultaneously measuring oxygen consumption and potassium extrusion in response to electrical stimulation in the CA1 region of acute rat hippocampal slices. We drove the system to test the limits by decreasing the time intervals between stimulations until we observed a change in response behavior. The simultaneous measurements allowed us to observe various time-dependent differences in characteristic responses between oxygen and potassium in the ranges between 1 min and 10 s.

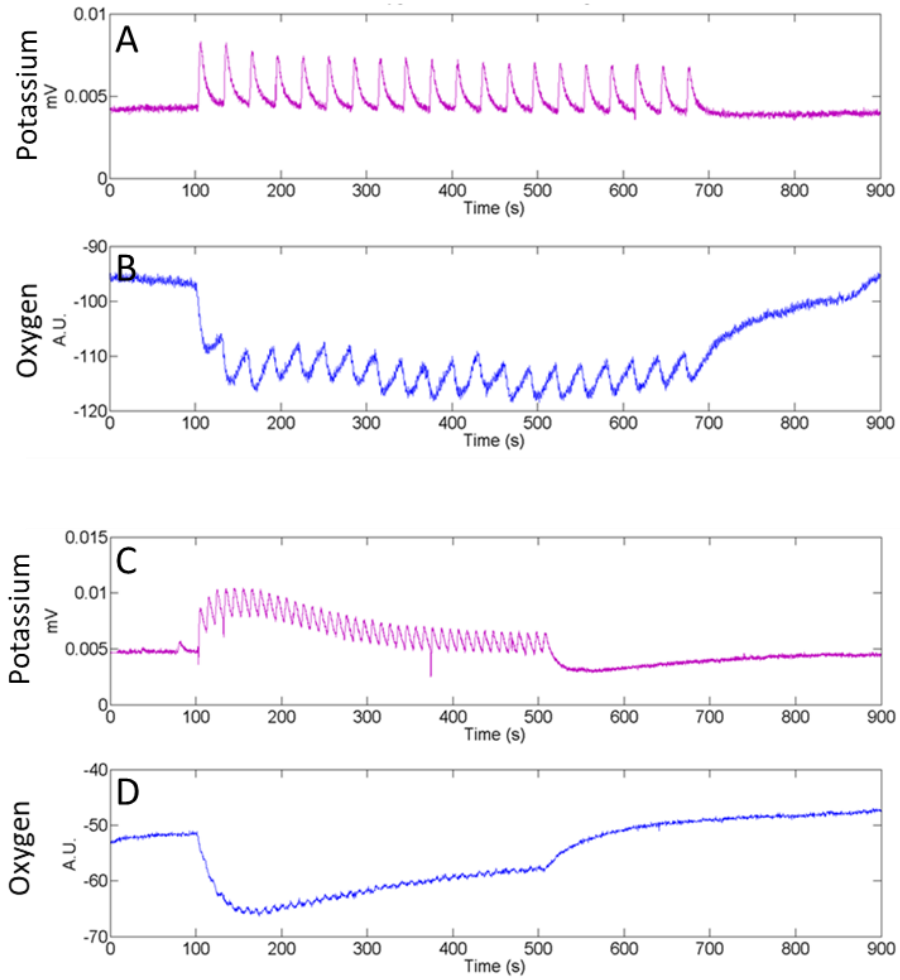

Figure 3: Representative time traces of simultaneous potassium and oxygen measurements.
Panels A-D show: A.) Potassium responses at 30-second intervals, B.) Oxygen responses at 30-second intervals, C.) Potassium responses at 10-second intervals, and D.) Oxygen responses at 10-second intervals.

Recovery ratios differ between oxygen and potassium.

We see that as stimulation intervals decrease, oxygen is the first component to fail to recover to baseline values between stimulations. By 1 min stimulation intervals, oxygen responses fail to recover completely as compared to potassium responses, which return to baseline before next stimulation (Figure 3). Figure 4 shows the averaged progression of recovery failure for oxygen as compared to potassium. At the shortest

interval of 10 s, potassium also fails to re-establish itself between stimulations. However, this failure in potassium occurs at a much higher stress level than oxygen. Moreover, at 10 s intervals, both oxygen and potassium display non-monotonic behavior and appears to reach a second steady state after the maxima, that seems to consume less oxygen and extrude less potassium for the duration of the run. Figure 5 shows that for 5 and 10 min stimulation intervals (data not shown), oxygen recovers completely between stimulations. However, below 100 s, oxygen does not even achieve 80% recovery, a very sharp decline in recovery ratio at 20 s. But potassium responses have 100% recovery until 20 s stimulations.

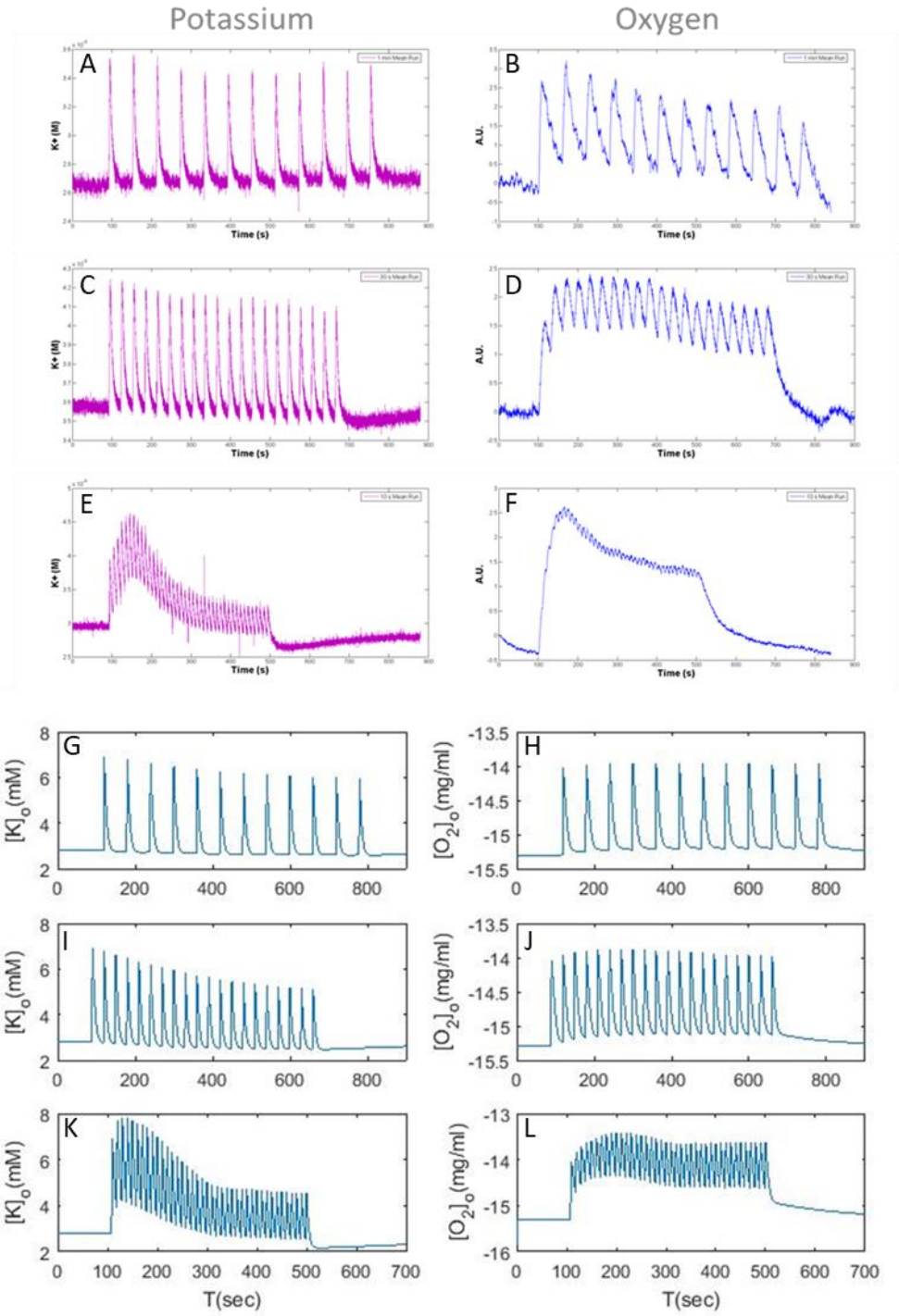

Figure 4: Averaged experimental results of O_2 and K^+ as compared to model predictions.
Panels A-F show experimental potassium and oxygen responses at 60-, 30-, and 10-second intervals. Panels G-L show computational results for potassium and oxygen at the same time intervals.

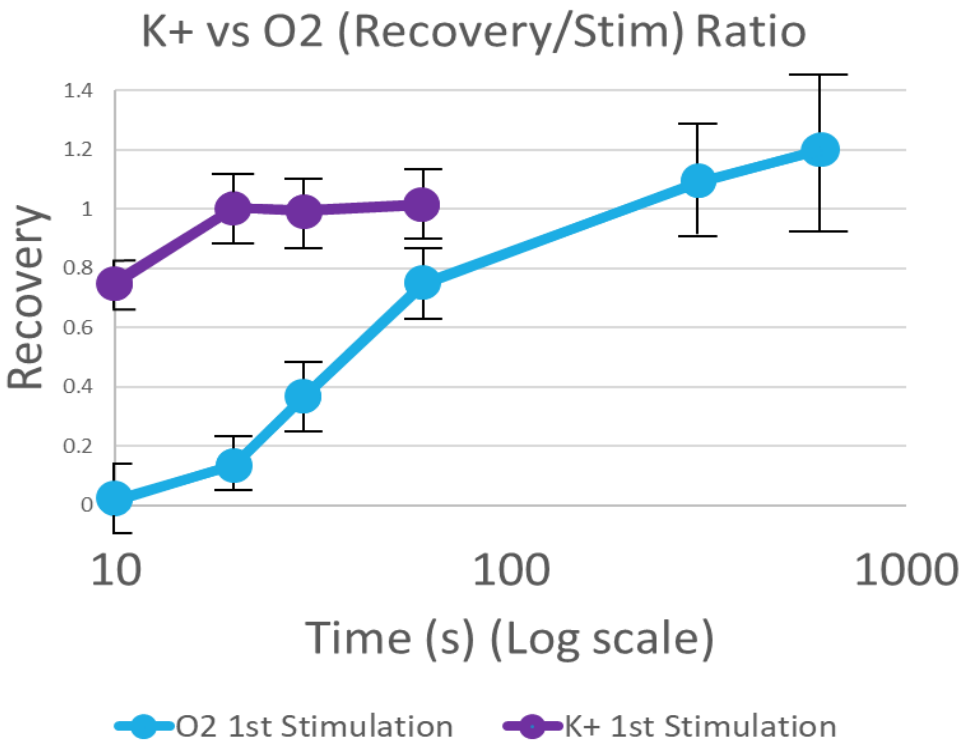

Figure 5: Recovery Ratios for potassium and oxygen.
The percent recovery from stimuli before the arrival of a subsequent stimuli as a function of the duration between stimuli. The purple shows the potassium recovery and the blue the recovery for the oxygen.

Time to reach maximum level of response differs between oxygen and potassium.

Oxygen and potassium display different behaviors in their non-monotonic responses to increased stress. Oxygen reaches a maximal consumption rate at about 70 s regardless of the stimulation interval, suggesting that the system has gone into a new regime. Potassium displays monotonic behavior for responses to stimulation intervals greater than 10 s. However, at 10 s intervals, potassium consistently reaches its maxima

approximately 10 s (equivalent to one stimulation interval), sooner than oxygen as is seen in Figure 3, Figure 4 and Figure 6.

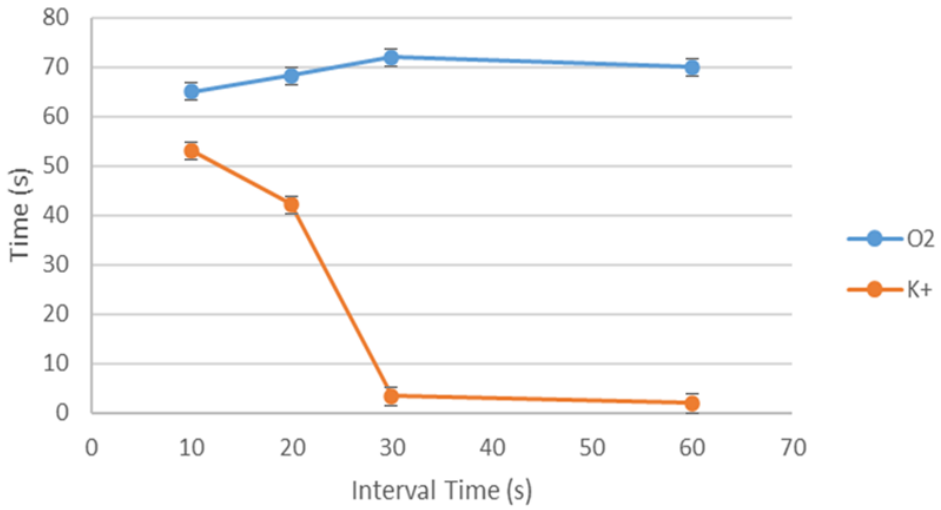

Figure 6: Time to reach maxima The time to the maximum response for the potassium and oxygen stimuli as a function of the interstimulus interval.

Simulated results reflect the same behaviors observed experimentally

The model was able to replicate the extracellular potassium response seen in the stimulation experiments (Figure 4 and Figure 7). The top right panel in Figure 7 shows the increasing potassium signal that reaches a maximum before dropping down to smaller amplitude responses near the original baseline. This behavior may be understood in terms of the progressive change in the electrical response to stimulation. In the early stages of the stimulation train each stimulation pulse produces two spikes whereas towards the end it has been reduced to a single spike per stimuli. This is the most

important effect in sculpting the response however the overall shape is also controlled by the shifting reversal potentials.

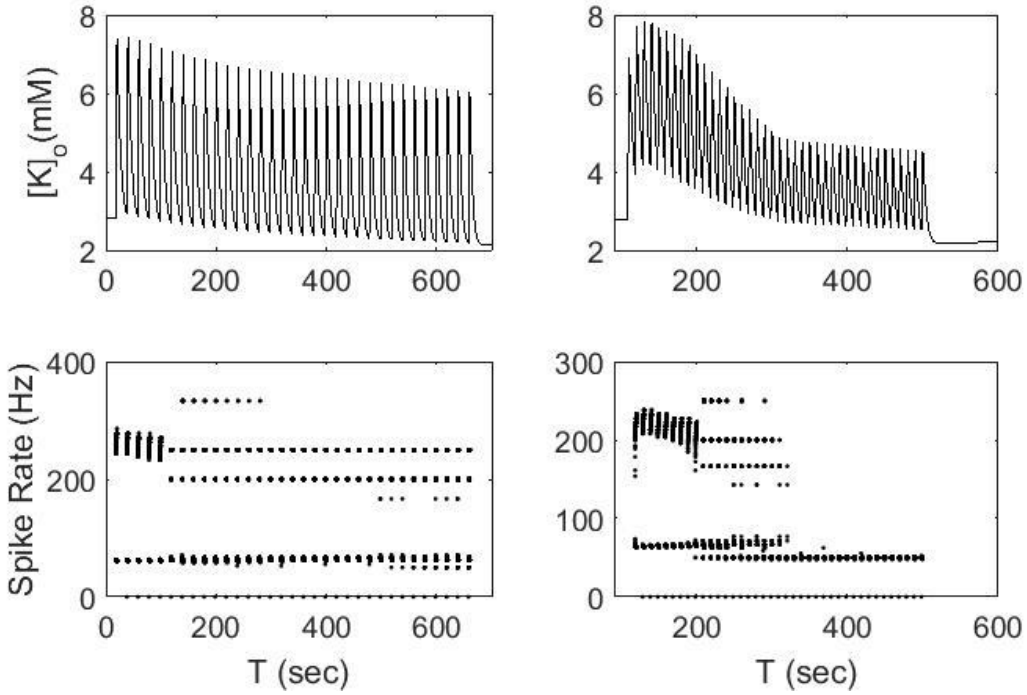

Figure 7: Potassium Recovery.
The top panles display the extracellular potassium concentration for potassium for interstimulus intervals of 20 seconds (left) and 10 seconds (right). The bottom panels show the instaneous spike rates for the stimulated neurons.

Simulated results do not require the addition of metabolic dynamics to replicate non-monotonic experimental behavior

With the model able to replicate the potassium responses we investigated whether the accompanying metabolic dynamics would provide results that were in agreement with experimental results. To begin we utilized the assumption that the ATPase was the driver for metabolic production of ATP. Therefore, we investigated the pumping rates for the

neuronal(orange) and glial(blue) cells as shown in the second row of Figure 8. For both stimulation intervals the glial cells show marked decrease in pumping activity as the stimulation progressed owing to the pumps depleting the internal sodium as seen by the yellow traces in the first row of this figure. The internal sodium levels for neurons (orange) on the other hand display a more steadily increasing pumping rate as their internal sodium rises due to action potential generation.

The last row in Figure 8 shows the sum of the glial and neuronal pumping rates after weighting their volumes, nearly two to one for the glia to the neurons. The qualitative features from the oxygen consumption from the data are captured by the model. Where for the twenty second stimulation intervals the ATP consumption reaches a steady state whereas the ten second intervals produce a maximum consumption rate that peaks shortly after the potassium as was found in the experimental results.

Next, we incorporated dynamics to emulate the well-known Crabtree effect. To summarize; this effect entails an activity mediated, perhaps extracellular potassium, switch that limits aerobic metabolism in the glia to glycolytic producing lactate that can be utilized by the neuron. We therefore used a phenomenological switching function based on the extracellular potassium concentration that simultaneously reduced the glial oxygen utilization and increased the maximum rate of oxygen utilization in the neuron. The results of these added mechanisms can be seen as the brown trace in Figure 9 where the blue trace is the result of the model before the addition of the switch.

.

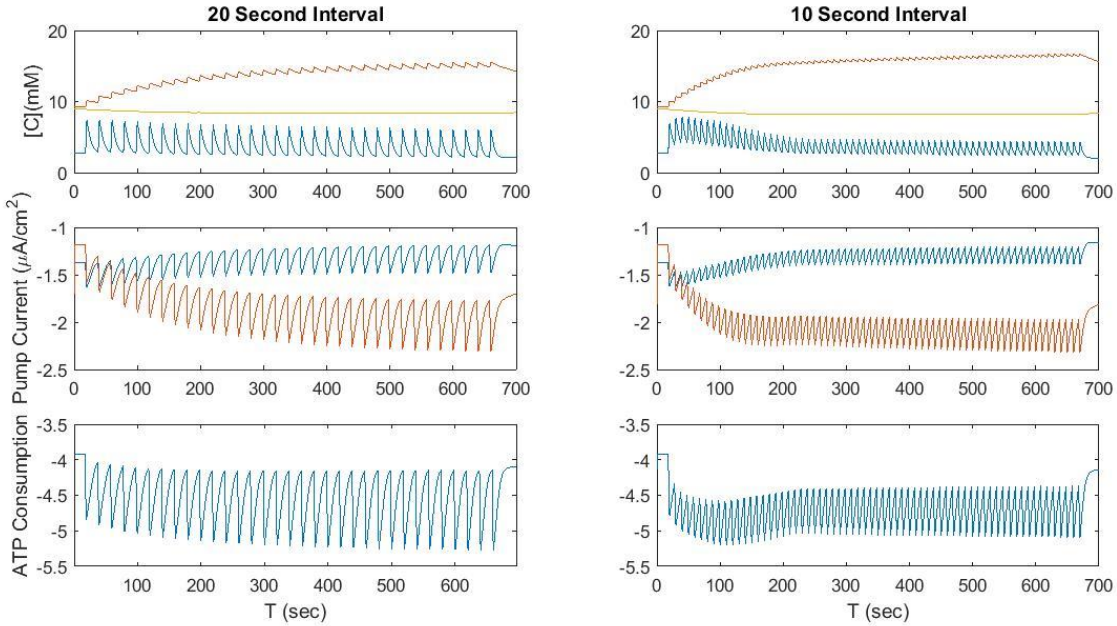

Figure 8: ATPase activty.
The top panels display the extracellular potssium concentration (blue) and the intracellular sodium concentrations for the neuron (orange) and glia (yellow) for 20 seconds (left) and 10 second (right) inter stimulus instervals. Second row of panels shows the rate of pump activty for the astrocytes (blue) and neurons (orange), and the last row shows the sum of the individual currents after weighting by their relative volumes.

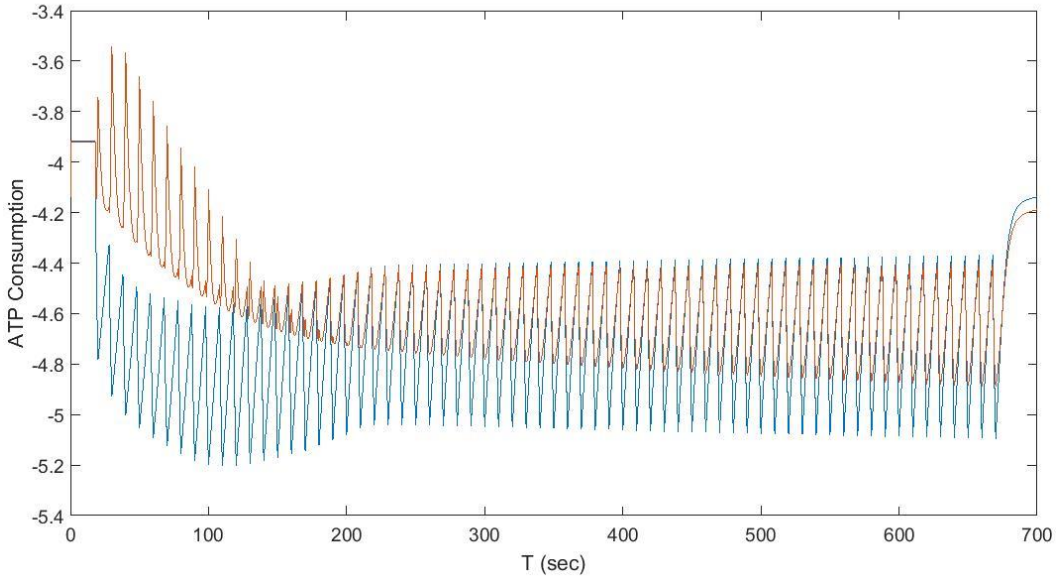

Figure 9: Canonical versus Non-canonical.
Blue curve depicts the ATP production for the canonical metaboic response, whereas the brown curve show the response when the activity-dependent metabolic swtich is imposed on the model.

Discussion

Neuronal systems are capable of producing an extremely large range of activities, but all of these are ultimately limited by the rate at which they can consume and dissipate energy in an effective manner. These bounds will provide insight into pathological conditions such as epileptic seizures, migraines, stroke, and hypoxia. We used two markers, oxygen and potassium, along with a computation model, to assess the consumption and dissipation of energy in an ex vivo preparation. We used the model to provide a mechanistic explanation of the experimental findings. Furthermore, the model provides insight into the effects of neuronal function and mechanisms of stress related metabolic shifts. In this manner we have developed a tool to understand energy limitations in neuronal systems, as it is applied in Chapter 3 to a new form of stimulation.

We demonstrated experimentally that the oxygen consumption reaches a maximum rate that appears rather sustainable as evidenced by the near steady response at 20 second intervals. Interestingly, the model suggests that this balance is only achieved on the level of the tissue, and that the increased neuronal metabolism and decreased glial metabolism balance each other before either reaches a steady state. This opposition is not produced by a complex sensing system, but a simple consequence of the neuronal and glial response to extracellular potassium. Sensitivity to extracellular potassium increases pumping due to activity induced increases in extracellular potassium in both cell types. However intracellular sodium concentrations for the two cell types goes in opposing directions as the pump is out stripped by active currents in the neuron but exceed resting leak currents in the glia. Increasing and decreasing sodium in the respective cell types ultimately controls the difference in their metabolic needs.

Unlike the oxygen, the potassium responses recover for stimulation intervals as low as 20 seconds. For 10 s intervals however, the transient response in potassium goes through a maximum before settling into a lower steady state. Our model shows that the potassium follows the spike output which first increases due to the excitatory effects of potassium accumulation and later decreases due to the hyperpolarizing effects of the increased pump rates due to sodium accumulation.

Presently the model does not incorporate ATP dependence in the pump rates, making the metabolic response incapable of affecting neuronal activity. Further analysis of the model as seen in Figure 8, shows that ATP concentrations, though capable of reaching a steady state could begin to have an effect neuronal activity.

Recent studies suggest that at rest and at moderate levels of activation, neurons consume glucose as well as lactate from astrocytes, whereas at supraphysiological stimulation (e.g. excitotoxicity), mitochondria fail, and neurons start to produce lactate. A fine balance between glycolysis and respiration in these cells is ensured by shared control of both pathways by the Na+/K+ pump (Baeza-Lehnert et al., 2019). Briefly the mechanism can be summarized by: 1.The high activity in the neuronal cells will lead to potassium accumulation which will shift metabolism from oxidative phosphorylation to primarily glycolysis in the glial cells reducing their oxygen consumption and 2. then in the neurons, their response is purely determined by the action of the pump (Barros et al., 2020). Our data does appear to demonstrate, if only transiently, that the aerobic metabolism can be driven beyond the steady state ceiling. However as stated above this maximum occurs at a similar time to the maximum in potassium and can be explained through the ionic and electric dynamics of the cell.

Methods and Materials

Animals

Male Long Evans rats, age 42 days or greater.

Slice Preparation

Each rat was anaesthetized with isoflurane and decapitated. The extracted brain was placed in an oxygenated, low Ca_2^+ ACSF semi-frozen slushy for approximately one minute prior to dissection of the hippocampus The low Ca_2^+ ACSF contained (in mM): KCl, 2.8; D-glucose, 10; NaHCO3, 26.2; NaH2PO4, 1.25; CaCl2x2H2O, 0.5; MgSO4, 7; Sucrose, 210. The isolated hippocampi were cut into 400-μm transverse slices using a

tissue chopper. The slices were temporarily placed in a chilled, oxygenated solution of the same low Ca_2^+ ACSF until all the slices had been made. The slices were then transferred using a sable paint brush to a pump-circulated incubator containing oxygenated ACSF at room temperature which was then slowly brought up to 35°C. The ACSF in the incubator contained (in mM): NaCl, 126; KCl, 2.8; NaH2PO4, 1.25; CaCl2x2H2O, 2; MgSO4, 1; NaHCO3, 26.2; D-glucose, 11. The slices were incubated for approximately 1.5 h before the recordings started. An incubated slice was transferred to a submersion-type recording chamber that had been temperature-acclimated with oxygenated ACSF of the same concentration as the incubating ACSF using gravity flow to pass the solution through an in-line heater, into the recording chamber

Apparatus

The apparatus was composed of a perfusion recording chamber, with an in-line heater (Warner Instruments, model TC-324B), mounted to an Olympus BX51 epifluorescent microscope equipped with a Retiga EXi CCD camera model Fast 1394, a Lumen 200 Fluorescence system, a Photometrics Dual View splitter, and a Ludl shutter and filter wheel (570 nm). Optical measurements of the oxygen dye required filters in the ranges of 620 and 760 nm. Potassium was measured using a Warner Instruments HiZ-223 high-impedance amplifier. Tissue was electrically stimulated using an A-M system isolated pulse stimulator (model 2100). The apparatus was housed in a fully-enclosable, light-proof Faraday cage on top of a TMC air table.

Electrode preparation.

Stimulating electrodes. Twisted pair bipolar stimulation electrodes were fabricated from 75/~m platinum wire insulated with Teflon (Medwire, Mt. Vernon, NY).

Oxygen/Reference electrodes. Oxygen-sensitive electrodes (optodes), capable of simultaneously collecting optical oxygen readings as well as electrical data were fabricated in-house, as described in Ingram et al., 2013. The optodes were constructed of pulled borosilicate glass micropipettes which were dipped in an oxygen-sensitive polymer matrix. The matrix was prepared by dissolving 22mg of polyvinyl chloride (PVC) and 44mg bis(2-ethylhexyl) ester (DOS) in 0.5 mL of tetrahydrofuran (THF) and sonicating until emulsified. Stock solutions of THF containing 0.98 mg of Pt(II) Octaethyl Porphine Ketone (PtOEPK) (Frontier Scientific) and 0.05 mg BODIPY 577/618 maleimide (Invitrogen) were added to the plasticized PVC and evaporated to 1mL (Hartmann & Trettnak, 1996). The pulled micropipettes were attached to an adapted syringe and pressurized with air to prevent the tip from being clogged with dye. Air pressure was maintained while the tip of the micropipette was dipped 10x into the dye matrix. The coated micropipettes were allowed to dry, and the tips were rinsed with deionized (DI) water to remove any excess THF. The dried micropipettes were filled with ACSF of the same composition as was present in the recording chamber and tested at the time of use to ensure a resistance of 2-8 MΩ.

Potassium-sensitive electrodes. Potassium-sensitive electrodes were also made in-house as described in (Ammann, Chao, & Simon, 1987). The electrodes were constructed of pulled borosilicate glass micropipettes *without filament*. The glass pipettes were filled with 9 μL of Sigmacote and suspended over low heat for approximately an hour. The

remaining Sigmacote was blown out of the pipette tip using tubing connected to an air supply. The pipettes were suspended over low heat for another hour and then left to dry overnight. The next day, the pipettes were inspected under a microscope to ensure that they were completely clear indicating that they were dry. Once dry, the pipettes were filled with 6 μL of Sigma-Aldrich Potassium ionophore I- cocktail B and gently back-filled with 100 mM KCl solution.

Stimulation parameters

Electrical stimulation. The stimulating electrode was placed in the region of the stratum radiatum near CA1. Stimuli were applied under computer control, in randomized sets of intervals consisting of: one stimulus per 1 min., 30 s, 20 s and 10 s, using a train burst width of 2 s, pulse duration of 1×10^{-3} s, inter-pulse period of 2.5×10^{-2} s and an output of 150 – 200 μA.

Recordings

Extracellular recordings were made by placing the optode and potassium-sensitive electrode in very close proximity to each other in the cell body layer of the CA1. Optical data were recorded using IP Lab software. Potassium and electrical data were recorded using an in-house Labview program.

Data processing and analysis

All data and statistical analysis were processed in Matlab. All statistical analyses were performed using a one-way ANOVA.

Computational Model

See Chapter 4 of this dissertation for full details.

Contributions

Performed Experiments: Monica La Russa Gertz

Developed model: John Robert Cressman, Monica La Russa Gertz, and Jay Siva

Literature search: Monica La Russa Gertz

Wrote chapter: Monica La Russa Gertz and John Robert Cressman

Edited chapter: Monica La Russa Gertz and John Robert Cressman

CHAPTER THREE: ULTRASOUND MODULATION OF NEURONAL METABOLISM AND IONIC DISTRIBUTION

This chapter is the second of two papers that investigate the metabolic demands of neuronal stimulation. In this chapter we apply the simultaneous oxygen and potassium measurement techniques that we developed and refined in the previous chapter to measure metabolic responses to FUS stimulation in hippocampal slices. We use the data acquired in the previous chapter as a point of comparison to gain an understanding of the differences in metabolic demands between the two stimulation modalities. We also expand on the earlier computational model by adding a volumetric module to describe and interpret the experimental results.

Abstract

Focused ultrasound (FUS) presents the ability to non-invasively modulate neuronal activity with greater resolution and penetration than other methods, making it an attractive platform both in basic research and clinically. Research has mainly focused on elucidating the mechanisms underlying this mode of stimulation. Yet, the metabolic effects of FUS modulation on neuronal tissue have been overlooked, though changes in metabolism have profound effects on neuronal activity. We investigated the metabolic demands of FUS modulation both experimentally and computationally. Acute rat hippocampal slices were stimulated in the CA1 region using a 35MHz focused ultrasound transducer at varying intervals, with stimulation durations ranging from 0.1 - 2 s. We used oxygen- and potassium-sensitive electrodes to measure the metabolic demands of FUS as compared to electrical stimulation. Potassium responses remained similar for both

types of stimulation. However, oxygen responses failed to recover during shorter electrical stimulation intervals, indicating greater energy requirements for electrical stimulation as compared to FUS stimulation. We also modulated neuronal responses to electrical stimulation ultrasonically, yielding a significant pulse-repetition-frequency (PRF)-dependent increase in local field potentials. We demonstrate that simulating the effect of FUS on oxygen and potassium responses requires implementing the ultrasonically induced volumetric changes that lead to osmotic changes in tissue within the focal region. We conclude that spatiotemporal ionic redistribution due to acoustic radiation force is largely responsible for the observed effects, and that metabolic demands contribute to the efficacy of FUS stimulation, thereby opening a new avenue of investigation to elucidate mechanisms.

Introduction

Focused ultrasound (FUS) presents the ability to non-invasively modulate neuronal activity accurately, safely and with greater resolution than other non-invasive methods such as transcranial magnetic stimulation and transcranial direct current stimulation. This greater resolution provides new avenues in therapies for neurological disorders in the CNS such as epilepsy (Hakimova et al., 2015) and traumatic brain injury (Bystritsky & Korb, 2015; Kubanek, Shukla, Das, Baccus, & Goodman, 2018; Monti, Schnakers, Korb, Bystritsky, & Vespa, 2016; Sanguinetti et al., 2020), among others. To date, it has been demonstrated that FUS can provide targeted and minimally invasive modulation of neuronal activity in specific areas of the brain, retina and peripheral nerves using non-ablative parameters to elicit either motor or sensory responses in humans (W.

Lee, Lee, et al., 2016; Legon et al., 2014a; Monti et al., 2016), monkeys (Deffieux et al., 2013; Wattiez et al., 2017), rats (Jiang et al., 2018; Younan et al., 2013b), mice (Y. Li et al., 2007; Mehić et al., 2014b; Tufail et al., 2010; Tyler et al., 2008a; Ye et al., 2016), and salamanders (M. Menz et al., 2017; Michael D. Menz, Oralkan, Khuri-Yakub, & Baccus, 2013). The non-invasive yet high-resolution nature of this technique makes it an excellent tool for both clinical and basic studies alike. However, our lack of understanding of the mechanisms underlying ultrasonic neuronal modulation leaves open several questions pertaining to its efficacy and safety. Though there has been substantial research into understanding these phenomena, the myriad responses ranging from excitatory to inhibitory, under different conditions, speaks to a rich landscape of modulation targets and effects. Yet, this same diversity of effects could also provide a palette for eliciting precise and graded control of neuronal responses. While several mechanisms are still being investigated, some more promising than others, no one to date has explored what effects any of these mechanisms have on neuronal oxidative metabolism and ion redistribution within and outside the neuron, which is crucial to neuronal activity and health. Understanding these metabolic and ionic effects can help to clarify some of the confounding results observed within the field.

Neurons and neuronal functions are highly sensitive to the disruption of oxygen and potassium levels, as is seen in depolarization block, which can occur as a result of hyperkalemia (elevated extracellular K+ concentration) that shifts the K+ equilibrium and the coupled resting membrane potential to depolarized levels. This effect occurs in scenarios such as: crush injuries that release large amounts of intracellular K^+ into the

extracellular space; during epileptic discharges, or impairment of the Na^+/K^+ pump (ion transport) by disruption of oxidative metabolism through hypoxia or anoxia (Watts et al., 2018). Moreover, oxidative metabolism provides most of the energy needed by the neuron in the form of ATP, which is used by the sodium/potassium pumps to re-establish and maintain the ion gradients across the membrane and is strongly correlated with evoked neural activity (Mathiesen et al., 2011). Some FUS mechanism candidates could potentially affect these two very important components of neuronal function (oxidative metabolism and ion redistribution); in particular, acoustic radiation force. Potential FUS mechanisms can be divided into two main areas: thermal and mechanical. Mechanical candidates can be further subdivided, but acoustic radiation force and stable cavitation are the most prominent within this group (Mike D. Menz et al., 2019).

In this study, we use oxygen- and potassium-sensitive electrodes to measure the metabolic demands placed on hippocampal tissue due to ionic redistributions created by FUS stimulation as compared to electrical stimulation. We also aim to elucidate potential modulatory effects based on alterations to the cellular ionic state that set the resting potential and tune excitability. We find that experimental results are consistent with a computational model that describes the effect of acoustic radiation force on ionic, metabolic and electrical responses to ultrasonically induced volumetric and osmotic changes within the focal region. We further conclude that ionic redistribution due to acoustic radiation force is a primary candidate for FUS stimulation in the absence of cavitation and places a lower metabolic burden on tissue than electrical stimulation.

Results

FUS stimulation causes duration- and intensity-based changes to extracellular oxygen and potassium

To measure changes in neuronal metabolism caused by FUS stimulation, we measured oxygen and potassium during FUS stimulation. We placed oxygen- and potassium-sensitive electrodes in the cell body layer of the CA1 region of the hippocampal slice while perfusing with oxygenated ACSF. Once we established that the slice was responsive (using electrical stimulation), we removed the stimulating electrode and began FUS stimulation. Since this is a novel approach, we tested the system using a wide range of stimulation parameters; from physiological to supraphysiological.

We found that FUS stimulation elicited simultaneous oxygen and potassium responses in the slice that persisted after stimulation had ceased. Extracellular potassium increased while extracellular oxygen decreased. Figure 10A shows the potassium [K^+] response which was converted from the voltage recordings using the Nernst equation. Figure 10B shows the simultaneous decrease in extracellular [O_2]. The fluorescence changes with the fractional change of dF/F was equivalent to a slope of 0.05 +/- 0.01 mg/mL. Figure 11A provides a detailed view of the continued rise in [K^+] after stimulation ceases.

We also found that there is a dose dependence not only with the total stimulation duration (number of tone bursts) as seen in Figure 13 but also with the spatial peak temporal average intensity (I_{SPTA}), which is dependent, in part, on the number of cycles per tone burst (i.e. 175, 350 and 700 kcycles per tone burst) Figure 12. Figure 13 shows statistically significant (ANOVA p-value ≤ 0.00001 for O_2 responses to electrical

stimulations) increases in K^+ output and O_2 consumption for increased stimulation duration at a constant I_{SPTA} and stimulation interval for the ranges between 0.1 – 2 s duration. Whereas Figure 12 appears to show a trend (significance not established) in K^+ output and O2 consumption for increasing I_{SPTA} at constant stimulation duration and interval for the ranges of 175, 350 and 700 kcycles per tone burst.

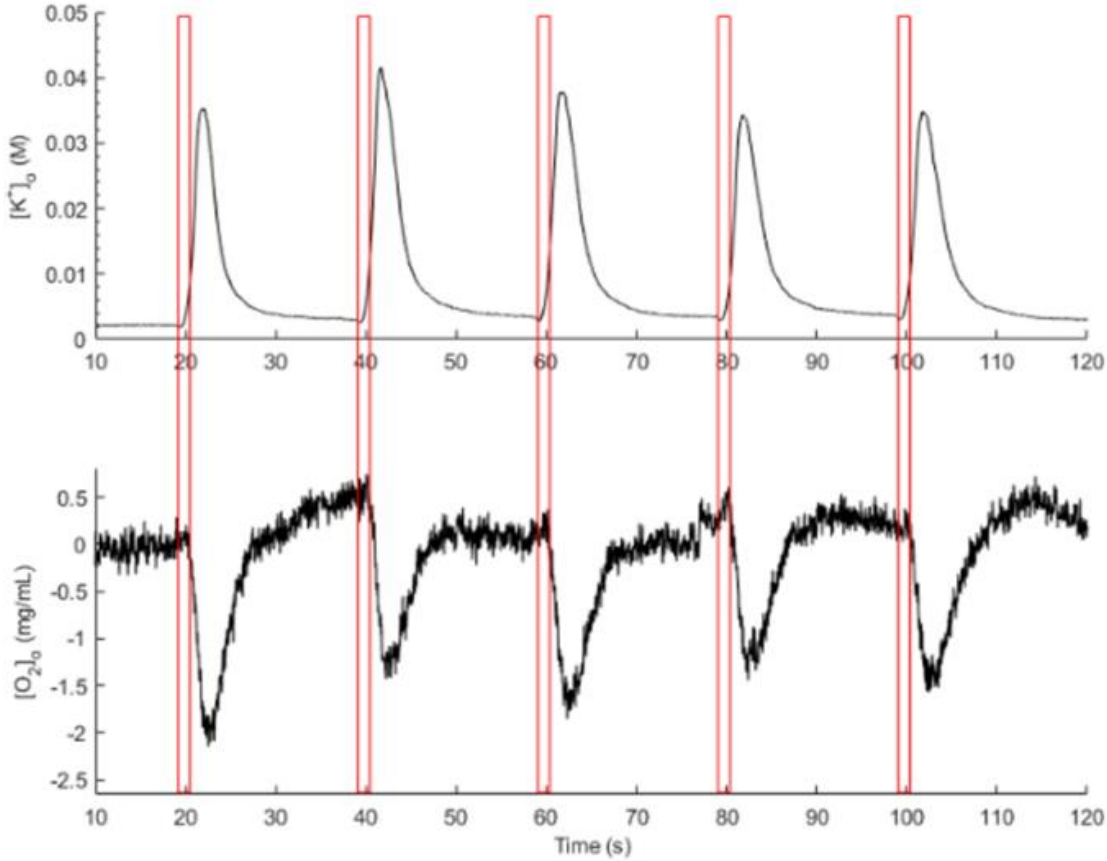

Figure 10: Simultaneous oxygen and potassium extracellular responses
Panel A and B show simultaneous recordings of potassium and oxygen changes in response to FUS stimulation. Panel A shows a representative extracellular potassium response to FUS stimulation every 20 s with a 2 s stimulation duration marked by the red boxes. Panel B shows the simultaneous extracellular O_2 response in mg/mL. Extracellular O_2 decreases as K^+ increases.

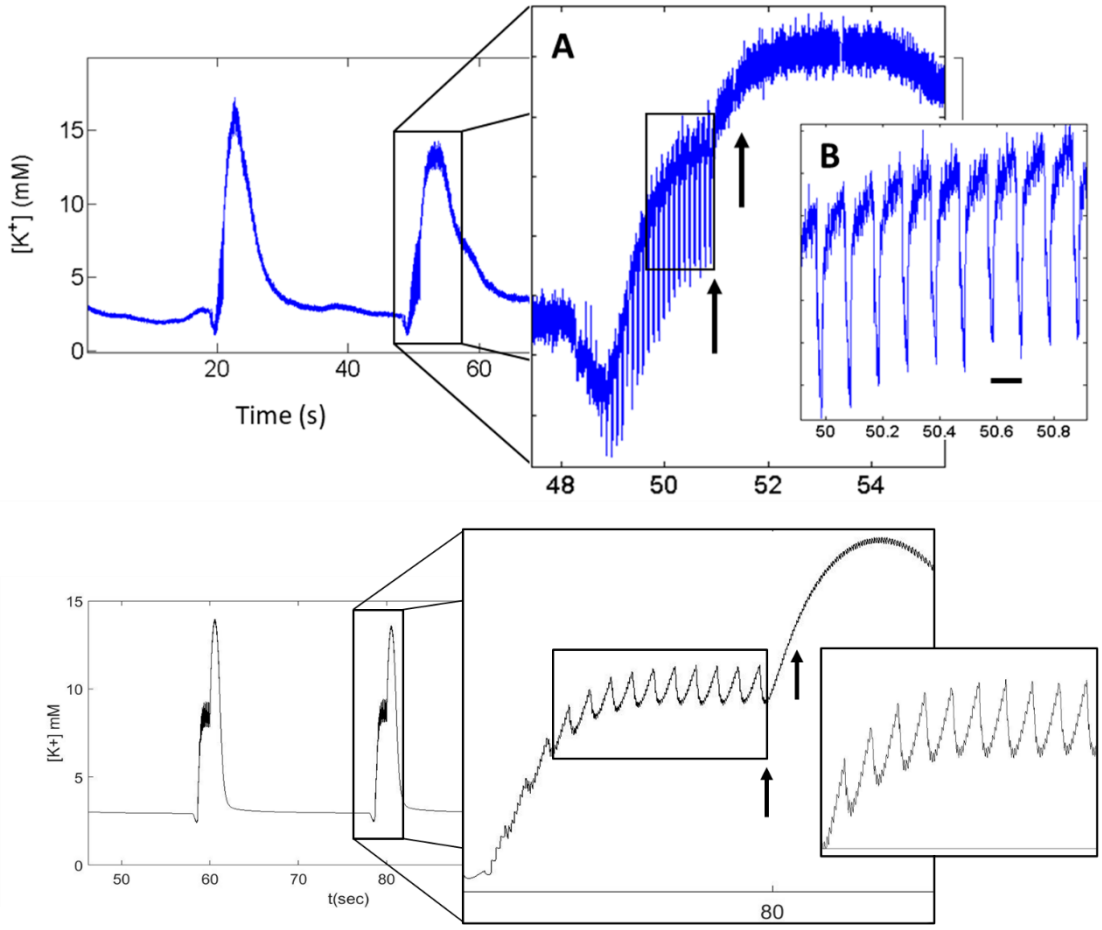

Figure 11: Extracellular potassium continues to rise after FUS stimulation ends.
Panel A shows a representative plot of experimental [K^+] response to 2 s FUS stimulation at 30 s intervals. The left arrow in inset B indicates the end of the stimulation train burst. The right arrow in inset B shows where the potassium response continues to rise after stimulation ends. Inset C shows a close-up of the fast oscillations of [K^+] corresponding to the 10 Hz stimulation. The black bar indicates 0.1 s. Panel D shows the simulated result of the same FUS parameters. Insets E and F show the same behavior as seen in panels B and C of the experimental time trace.

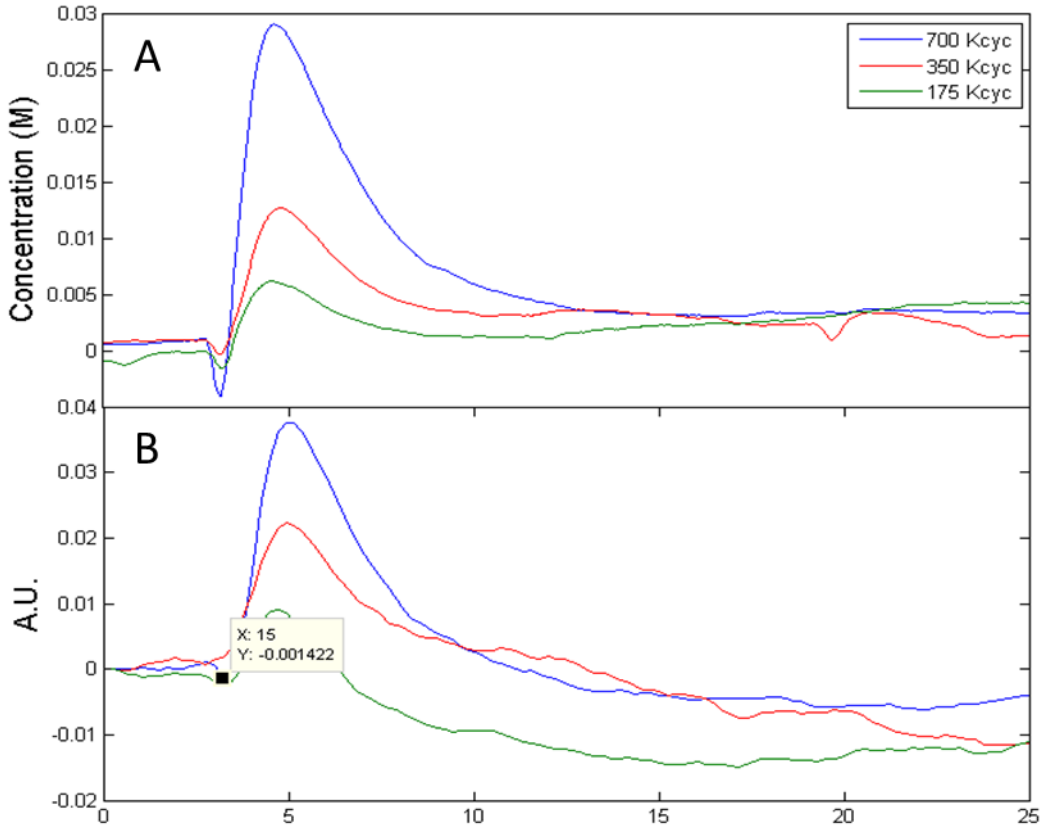

Figure 12: FUS response is dependent on intensity.
Panels A and B show the averaged means for K+ and O2 time traces respectively in response to 700, 350 and 175 kcycle FUS stimulation.

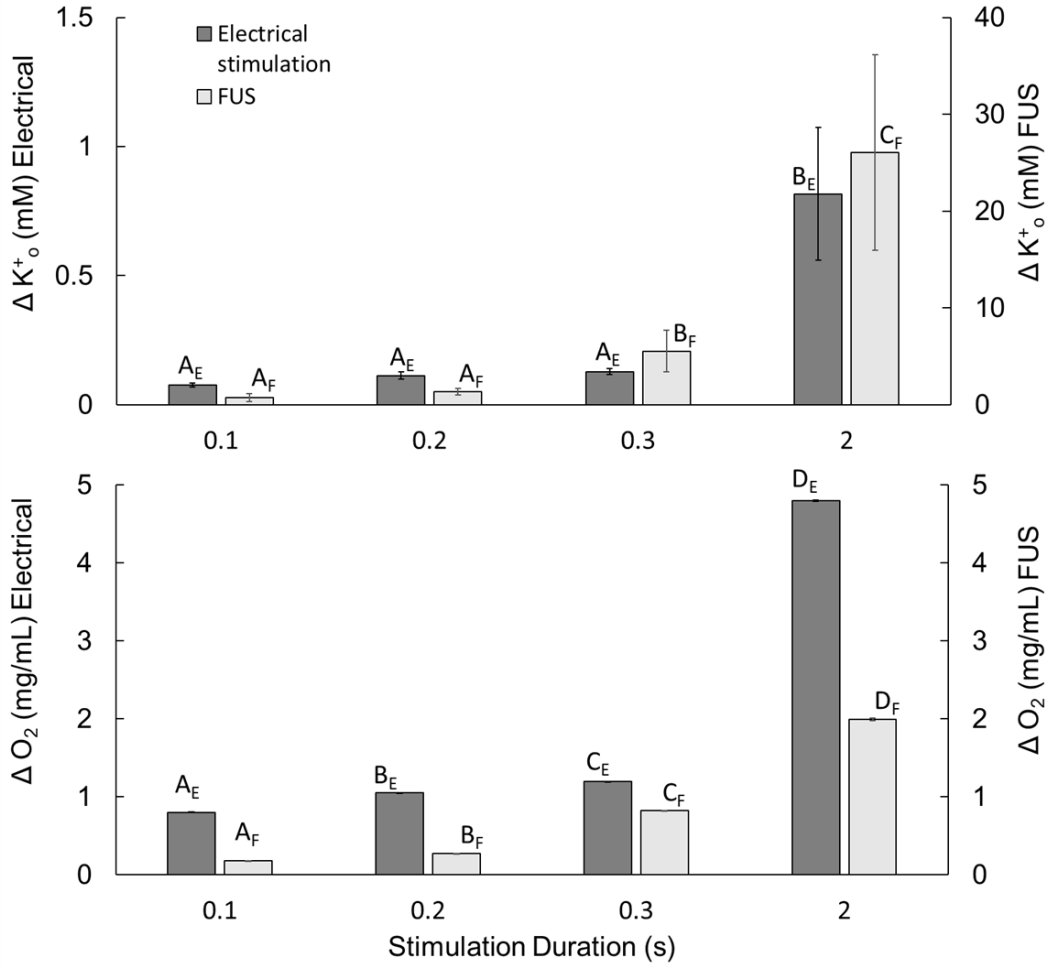

Figure 13: Comparison of the averaged peak amplitude of oxygen and potassium.
The magnitude of the evoked potassium and oxygen responses to both focused ultrasound stimulation (right y axis and light gray bars) and electrical stimulation (left y axis and dark gray bars). Subscript "E" represents electrical stimulation and subscript "F" is FUS stimulation. Bars with the same letters are not statistically different, whereas differing letters are significantly different.

Neuronal responses to FUS stimulation are dependent on oxidative metabolism

Since the mechanisms of FUS stimulation are not fully understood, it is not known if metabolism is involved in neuronal responses to FUS stimulation. To determine if the responses to FUS stimulation we were seeing were dependent on oxidative

metabolism, we reversibly quenched neuronal activity using NaCN while measuring extracellular oxygen and potassium. NaCN inhibits oxidative phosphorylation by reversibly causing cytochrome c oxidase to complex with cytochrome a3. This prevents the cytochrome oxidase from catalyzing the oxidation of cytochrome c through the reduction of oxygen. To measure dependence on oxidative metabolism, we applied modified ACSF containing 1mM NaCN for 10 min after 5 min of a baseline recording. At the end of 10 min of NaCN, we switched back to ACSF without NaCN and continued to monitor FUS responses.

Figure 14 shows that responses to FUS stimulation require oxidative metabolism. Neither oxygen nor potassium responses to FUS stimulation were significantly larger than the noise after 10 minutes of sodium cyanide application. This is not due to permanent neuronal damage because responses to FUS recovered during the wash out. Recovery was slow but nearly complete by the end of the experiment (Figure 14). Recovery of activity after 10 min chemical anoxia using NaCN in 10 mM glucose ACSF has been shown to occur after approximately 3 min after NaCN is washed out , however because our apparatus has a much larger reservoir than a standard perfusion chamber, NaCN wash-out was prolonged.

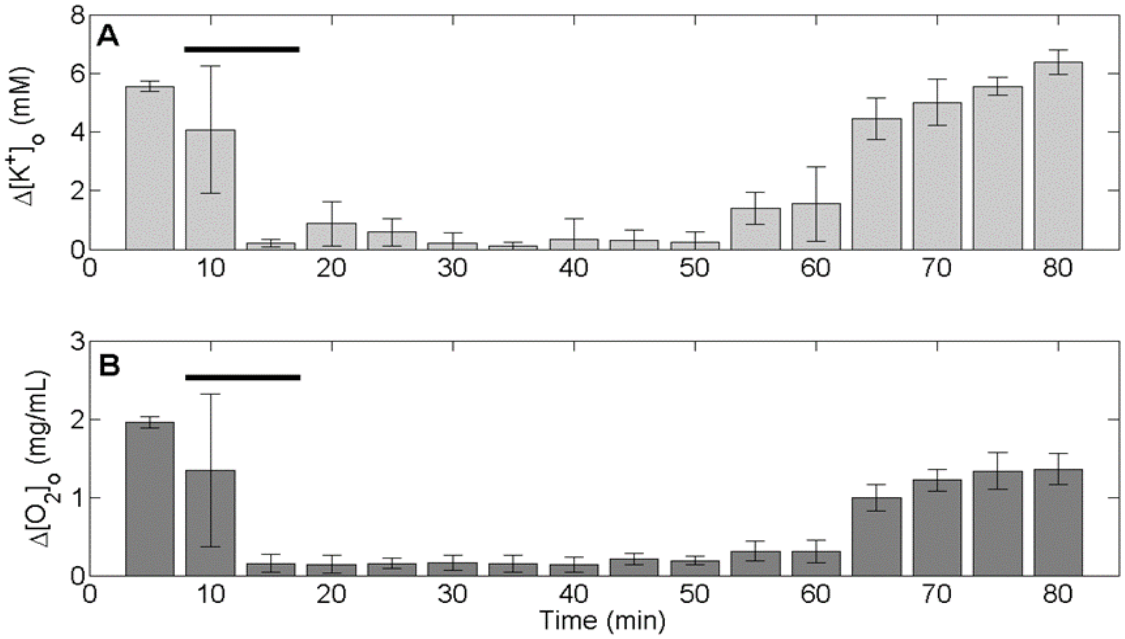

Figure 14: Quenching potassium and oxygen responses to FUS stimulation using NaCN.
Panel A and B show the average peak amplitude, in 5-minute increments, of potassium and oxygen respectively in response to the addition of NaCN at 10 minutes after the start of the recording. The black bar indicates the window of time NaCN was being added.

There are minimal thermal effects in this range of FUS stimulation

We measured the change in temperature for the same FUS protocols used in our experiments to determine if there were any substantial thermal changes that might lead to neuronal responses. We embedded a thin-wire (Omega) thermocouple in an agar phantom and recorded measurements both with and without perfusion flow. Without perfusion flow, there was a slight, but significant, duration-dependent increase in temperature. However, this increase was <1°C in a stimulation duration range between 0.1 – 2 s, which is well above the physiological norm and can be considered negligible. The addition of perfusion flow, at the same rate we used experimentally, removed the increasing trend and did not yield any temperature changes greater than 0.2°C (Figure

15). Though this does not completely rule out any thermal effects, it does imply that the dose-dependent increases in K+ and O2 are not thermally based.

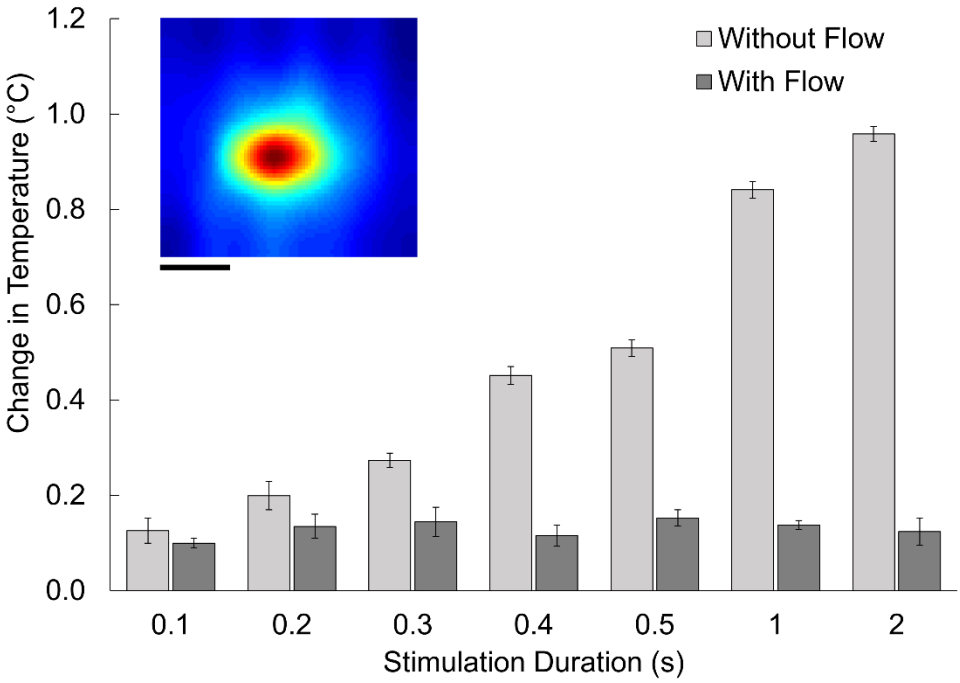

Figure 15: Thermal changes in response to FUS protocols.
Ultrasound-induced temperature changes with and without fluid flow. Temperature was measured using a thin-wire thermocouple embedded in an agar phantom and stimulated with 0.1 – 2 s durations of the same acoustic stimulation parameters used in the ex vivo experiments.

Metabolic responses differ between FUS and electrical stimulation

Because neurons and neuronal functions are highly sensitive to the disruption of oxygen and potassium levels, and even subtle changes in metabolism have profound effects on neuronal activity and health, we tested to see if there were any differences in metabolic responses between FUS and electrical stimulation. We found that FUS and

electrical stimulations produce robust and qualitatively similar oxygen and potassium responses. The two stimulus modalities however produce somewhat different physiological responses as can be seen when the interstimulus interval is reduced**.** Figure 16 shows the effects of both modalities of stimulation for 20-second interstimulus intervals. The potassium responses are qualitatively similar though not quantitatively similar. In comparison, the oxygen responses are markedly different, with FUS producing responses that fully recover between stimuli and electrical stimuli driving the tissue into an elevated level of oxygen consumption. Further differences between the two platforms can be seen in their response curves to stimulation duration as shown in Figure 13. FUS stimulation consumes less oxygen and releases more potassium, whereas electrical stimulation consumes more oxygen and releases less potassium.

Simulation of the effects of acoustic radiation force on the spatiotemporal response of brain tissue to FUS yield qualitatively similar results to experimental data

To interpret the experimental phenomenon we were observing, we modeled the oxygen and potassium responses with respect to ionic redistribution resulting from acoustic radiation force. The oxygen output in the model is represented by Na^+/K^+ pump activity. Figure 11 depicts a representative experimental time trace of potassium response to FUS stimulation as compared to a simulated result. Both the experimental and simulated time traces display distinct characteristics that are present in all the experimental responses. Here, we can see that the stimulation produces a large increase in extracellular potassium that persists after the cessation of stimulation indicating a transient physiological response. This potassium response reaches a maximum almost two seconds after stimulation termination. The model reproduces many of the key

features including the downward spikes that occur at 10 Hz intervals, which is the pulse repetition frequency of the ultrasound protocol. The model further reveals that these downward spikes are formed by the drop in local extracellular potassium concentration during tissue compression. Figure 16 further compares the model results of oxygen and potassium responses to ultrasound and electrical stimulation with the experimental time traces for the same parameters. We see that the model has been able to replicate the very large potassium responses in ultrasound as compared to electrical, whereas the oxygen is in the same general range for both modalities.

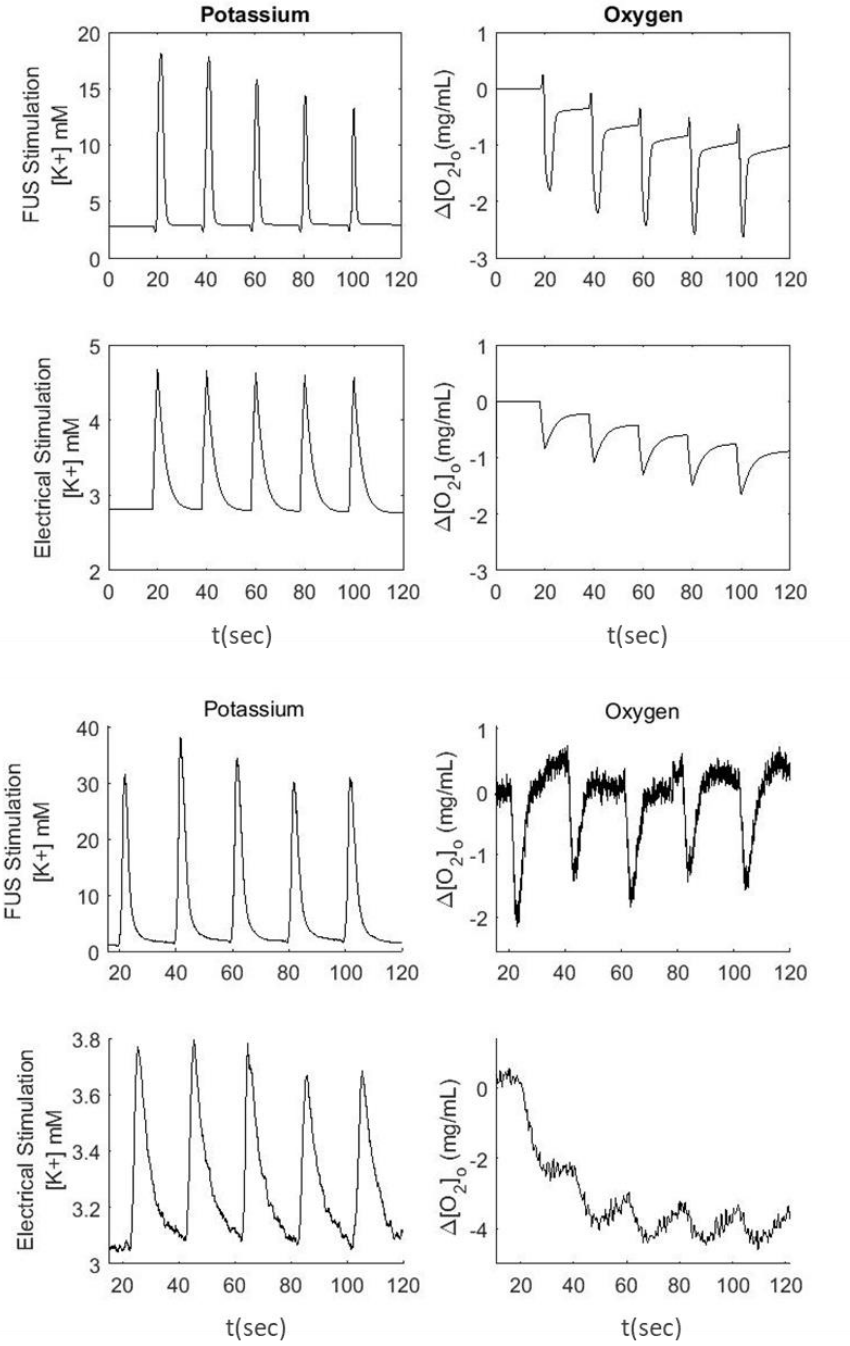

Figure 16: Comparison of model results to experimental data for FUS and electrical stimulation.
Panels A-D show the simulated results for potassium and oxygen time traces at 20 s intervals contrasting FUS and electrical stimulation. These are compared to panels E-H, which show experimental time traces of the same parameters.

The model reveals the ionic dynamics contributing to the observed experimental effects.

It seems paradoxical that the potassium extrusion during FUS should be so much greater while drawling a similar amount of oxygen. Since this result is qualitatively reproduced by the model, we can use it to investigate the cause. Figure 17 compares the ionic effects of electrical versus ultrasonic stimulation in the model. The change in sodium concentrations is far larger due to electrical stimulation in both the neurons and the glial cells. The effect is however inverted between the two cell types as the increased extracellular potassium leads to pumping of internal sodium. Neuronal cells produce the increased extracellular potassium while absorbing significant amounts of sodium to more than balance the increased pumping. However, the glial cells see a net outward flow of sodium which ultimately will limit the action of their pumps. This effect can be seen in Figure 18 as the pumping rates for the glial cells diminish towards zero during the course of the stimulation, whereas the pumps in the neuronal cells respond to their accumulation of sodium with increasing effect. The final simulation, Figure 18, shows that aggregate ATP consumption rates for the two compartments, after scaling for their relative volumes, is similar in magnitude for the two stimulation protocols. Also, in accordance with the experimental data, the recovery in response to FUS stimulation is much faster than the corresponding electrical response.

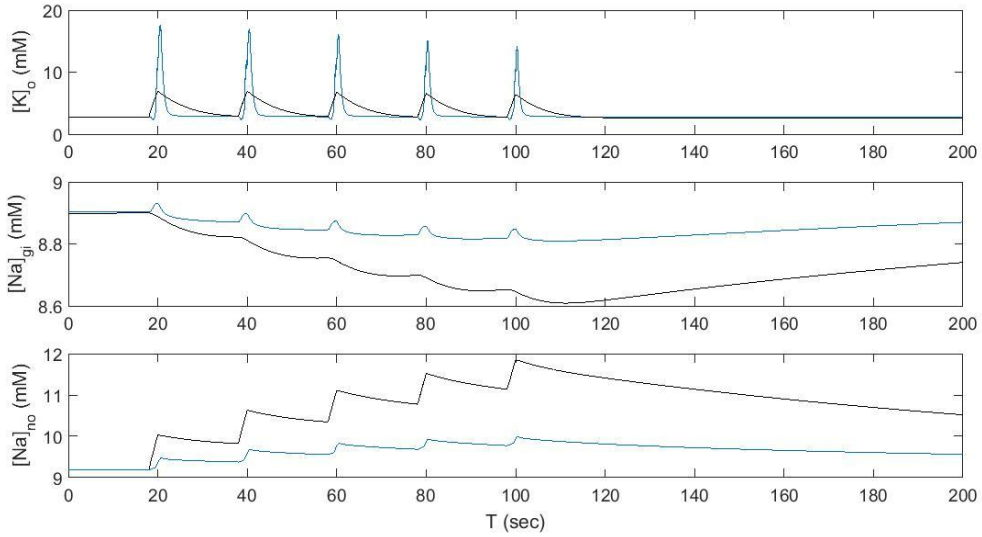

Figure 17: Ionic effects of electrical versus ultrasonic stimulation in the model.
The first panel shows the significantly larger increase in extracellular potassium due to the FUS stimulation (blue) as compared to the electrical stimulation (black). The second and third panels compare sodium changes within the glial and neuronal compartments respectively.

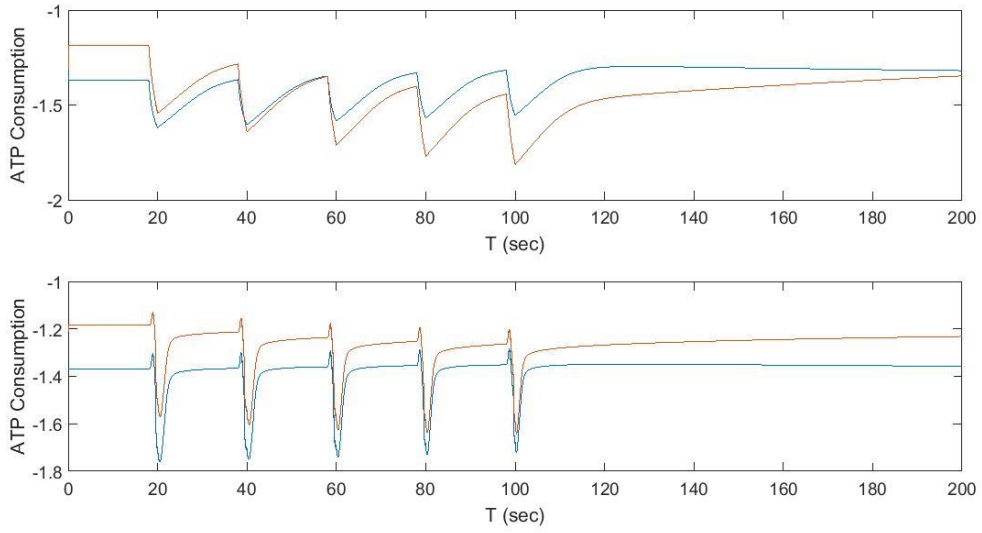

Figure 18: Sodium/Potassium ATPase activity.
the pumping rates for the glial (blue) and neuronal (orange) cells during electrical (top) and acoustic (bottom) stimulations.

FUS can modulate local field potentials in response to electrical stimulation

Our model predicts that neuronal tissue is left in an altered ionic state after FUS stimulation, which would lead to enhancement or quiescence of local field potentials and lead to translational therapies. To see if neuronal responses to electrical stimulation could be modulated using FUS, we applied regular intervals of FUS at 3 different pulse repetition frequencies (PRFs) during electrical stimulation (as described in detail in the Methods section). We observed a PRF-dependent increase in local field potentials when FUS modulation was applied during electrical stimulation. A significant increase in LFP responses is seen during modulation with FUS for all PRFs applied (p-value: 1Hz =.04, 5Hz =.004, 10Hz = .01). It was also noted that there was significant difference in LFP responses between FUS modulation and post modulation for 1 and 5 Hz but not for 10 Hz modulation. LFP responses post 10 Hz modulation did not return to pre-modulation amplitudes. A significant increase in LFP amplitude during modulation was also seen between 1Hz and 10 Hz (p-value = .01) (Figure 19).

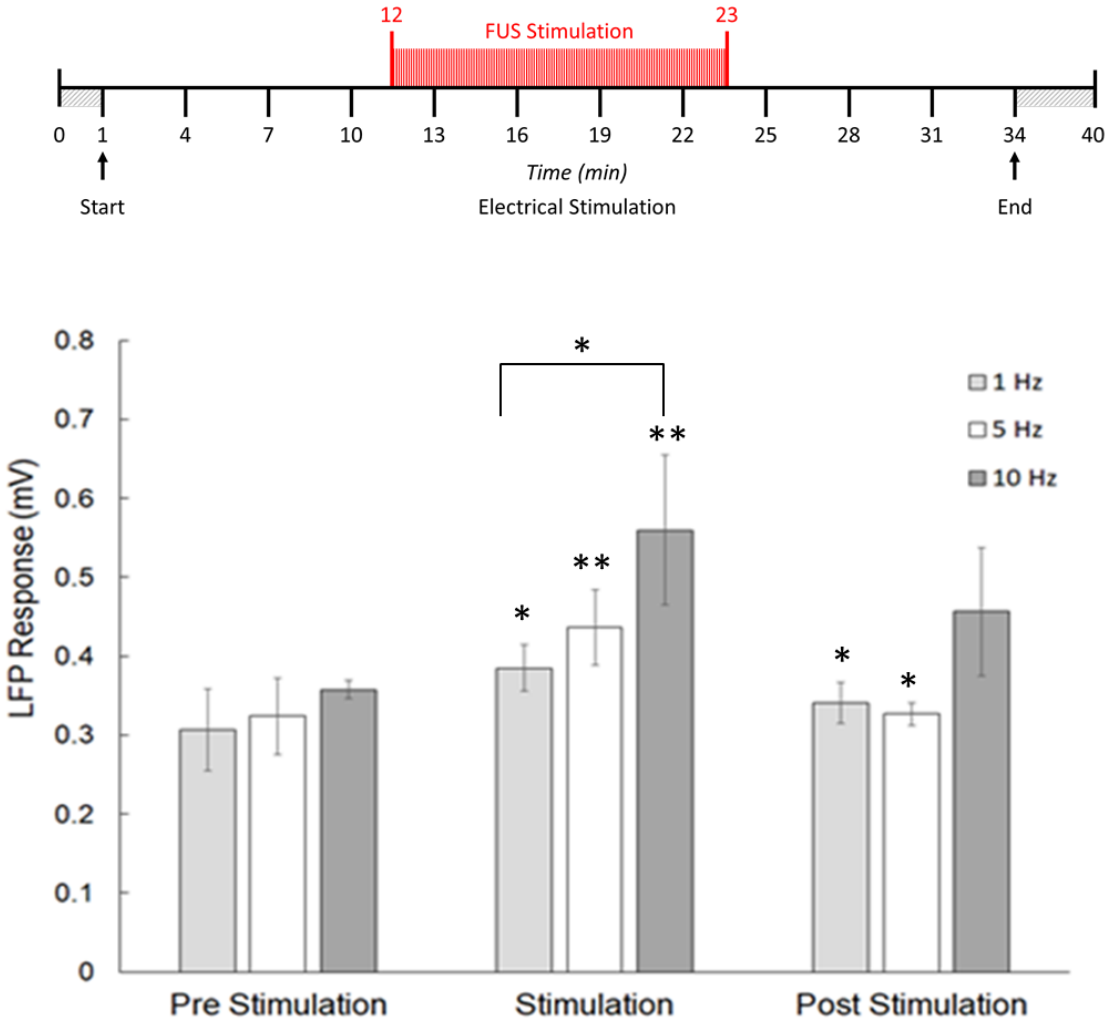

Figure 19: PRF-dependent FUS modulation of local field responses to electrical stimulation in the CA1 region at 1, 5, and 10 Hz.
During the entire run electrical stimulation was applied every 3 minutes using a train burst width of 2 s, pulse duration of 1 X 10-3 s, inter-pulse period of 2.5 X 10-2 s and an output of 150 – 200 µA to evoke local field potentials. Only electrical stimulation was applied to measure the baseline amplitude for LFP responses for the first 10 minutes. From minutes 12 to 23 the ultrasound stimulation (1, 5, 10 Hz) was also applied. Only electrical stimuli were then applied for the last 17 minutes to measure the recovery from ultrasonic modulation. (p-value: 1Hz =.04, 5Hz =.004, 10Hz = .01)

Discussion

To date no one has investigated the local metabolic demands of neuronal response to FUS. Understanding the changes in neuronal metabolism in response to FUS

stimulation can lead to enhanced methods of modulation as well as greater safety. We compared oxygen and potassium changes in response to FUS and electrical stimulation in the rat hippocampus to assess metabolic demands between both modalities. We also developed a computational model based on ionic redistribution. Our results show that FUS stimulation produces simultaneous responses to extracellular oxygen and potassium which are dependent on oxidative metabolism. We also found that metabolic responses differ between FUS and electrical stimulation in that FUS places a lower metabolic burden on the tissue. Furthermore, these changes in extracellular oxygen and potassium responses to FUS stimulation can be simulated using a model of ionic redistribution in response to acoustic radiation force in the absence of cavitation and thermal mechanisms. We also found that FUS can modulate the amplitude of local field potentials in response to electrical stimulation in ex vivo slices, which suggests a potentially new avenue of investigation.

Ionic dynamics and metabolism

We address the differences between these two stimulation modalities in the context of ionic redistribution and metabolic responses, with the understanding that FUS responses require intact metabolic activity as they are quenched by the application of sodium cyanide (NaCN) **(**Figure 14**)**. Alterations to ionic concentrations can lead to a strong metabolic drive through the action of the sodium potassium pump (Baeza-Lehnert et al., 2019). However, the metabolic demand produced by FUS stimulation is far less than that of conventional electrical techniques for the same ionic effects. The rate of recovery for oxygen is considerably slower for electrical stimulation, whereas potassium

recovers almost as quickly for electrical stimulation as it does for FUS stimulation **(**Figure 16**)** although our model shows that much of the potassium recovery in both scenarios is due to diffusion. Moreover, the ratios of these two major input (O_2) and output (K^+) factors show that though the potassium response for FUS stimulation is an order of magnitude greater than that of electrical stimulation (Figure 13), the oxygen consumption of FUS stimulation as compared to electrical stimulation is considerably lower; indicative of a significantly reduced metabolic demand. This holds true across all stimulation doses and is indicative of differing mechanisms of stimulation.

Simulated ionic results are achieved modeling acoustic radiation force in the absence of cavitation and thermal effects.

We chose to use a 35 MHz transducer not only because its narrow focal diameter provides highly localized stimulation in a small hippocampal slice, but also because cavitation is unlikely to occur at such a high frequency since the rarefaction time in this range is too short to allow bubble formation. Eliminating the possibility of cavitation would allow us to focus on the effects of ARF both experimentally and computationally with fewer confounds. Normally high frequency would not have direct clinical application since the high attenuation would prevent the beam from traversing the cranium. However, the findings in this study can be extrapolated to clinical settings based on the I_{SPTA} values. Generally, higher frequency also increases absorption in the tissue which leads to increased radiation force and thermal rise. However, the pulsed mode used in these experiments, deposits very little energy into the tissue therefore the thermal rise is negligible as was reported in the thermal data.

Based on these experimental conditions, we did not include cavitation or thermal components in our model. The simulated results are achieved solely on the volumetric changes produced by ARF compression of the tissue. This progressive compression leads to a reduction of extracellular space and an increase in tortuosity as the cell membranes are deformed **(**Figure 21**)**. This reduction in the extracellular space drives fluid out of the interstitial space. However, non-mobile osmotic agents such as hyaluronan and other proteins (Kawamata, Mori, Sato, & Katayama, 2007; Perkins, Arranz, Yamaguchi, & Hrabetova, 2017) remain in the interstitium thereby creating a change in osmolarity which leads to a re-distribution of ion concentrations. This effect is visible both experimentally and computationally in Figure 16 as each pulse incrementally reduces the volume of the tissue resulting in a similarly incremental increase of K^+ efflux. It is this change in gradients that drives the Na^+/K^+ pump activity and oxygen consumption.

Alternative biophysical mechanisms

There is significant evidence that mechanosensitive ion channels can respond to ultrasonic stimulation through changes in membrane conductance (Árnadóttir & Chalfie, 2010; Hamill & Martinac, 2001; Haswell, Phillips, & Rees, 2011; Mike D. Menz et al., 2019; Orr, Helmke, Blackman, & Schwartz, 2006; Tyler, 2012) Mechanosensitive ion channels Piezo, TRAAK, TREK-1, and TREK-2 have been investigated in several studies and found to have a significant influence on K+ currents in response to FUS (Brohawn, 2015; Martinac, 2004; Syeda et al., 2016). They were also required in responses by C. elegans to FUS stimulation in a study by (Kubanek et al., 2018). However, if we include an ultrasound-dependent conductance in our model, we cannot observe the biphasic

potassium response characteristic of our experimental observations. Therefore, although they may play a role, these channels are neither necessary nor sufficient to reproduce our findings. Exocytosis has also been found to slow down in response to high static pressure in a study by (Heinemann, Conti, Stühmer, & Neher, 1987). Although it is not clear how this would lead to neuronal responses it remains an avenue to explore.

Pressure induced phase changes in the plasma membrane would lead to changes in membrane conductance and capacitance and has been used as a model of neuronal stimulation (Mike D. Menz et al., 2019; Prieto, Oralkan, Khuri-Yakub, & Maduke, 2013). This appears in neuronal dynamics as a rapid varying membrane current which could lead to depolarization, but cannot address the observed disconnect between potassium accumulation and metabolic stress.

Extensions of the model to in vivo simulation

As already discussed, our model was designed to address the results from ex vivo experiments and not directly applicable to the in vivo condition. To extend the model to the in vivo setting we need to start by addressing the following issues: First, our model is based on the exchange of fluid and ions between an affected region of tissue and the bathing solution. When in vivo, the affected region would communicate with either surrounding, unaffected regions or perhaps, the vasculature, or primarily between affected regions of compression and expansion.

We do not expect significant qualitative differences between the dynamics for the compressed region in vivo versus in vitro for cases where the exchange is between neighboring neuronal spaces. However, the selective exchange constrained by the

vascular membranes and junctions may significantly alter the interplay with the affected neuronal tissue. Furthermore, we ran the model with only expansive stimuli and found minimal effects as the increased volume does little to change the osmotic pressure of the already dilute immobile ions.

Modulation effects

We studied the potential modulatory effects of FUS stimulation through its redistribution of ionic gradients. Ionic redistribution can produce a number of different secondary effects (excitation or inhibition), depending on the magnitude of the ionic responses and the specific ions that are affected. For instance, a rapid increase in extracellular K+ would cause its reversal potential to rise, resulting in excitation whereas a more gradual increase in extracellular K+ would lead to increased Na^+/K^+ ATPase activity that could hyperpolarize the cell resulting in quiescence (Owen, Barreto, & Cressman, 2013). Once well understood, such modulatory effects could be used in treatments of disorders such as epilepsy, depression, and anxiety among others (Bystritsky & Korb, 2015; Hakimova et al., 2015; Min et al., 2011; Monti et al., 2016). It induces a highly localized effect, penetrates deeply within the brain tissue, and is minimally to completely non-invasive.

Conclusion

In conclusion, our study differs from work done by others in two main areas: 1) We are not investigating a direct mechanism of stimulation, but rather are elucidating the metabolic implications of FUS stimulation through the effects of ionic redistribution. Though we used acoustic radiation force in our model, metabolic demands and ionic

redistribution can be investigated using any other mechanism. 2) We are not attempting to produce electrical responses directly from FUS stimulation, but rather modulate the ability of the tissue to respond to information-rich stimuli found in native neuronal networks by making the tissue either more excitable or quiescent through changes in ionic redistribution. The specific conditions used for this protocol resulted in increased excitability. However, the same protocol might have different effects in vivo since the diffusion properties of the tissue surrounding the target area would be different than that of a perfusion bath. The key is to gain an understanding of the ionic redistributions created by each different protocol to determine if the tissue will become more excitable or quiescent in the appropriate setting. This may help to explain the confounding results seen across the field of FUS stimulation and open new avenues of investigation.

Methods

Animals

Male Long Evans rats, age 42 days or greater.

Slice Preparation

Each rat was anaesthetized with isoflurane and decapitated. The extracted brain was placed in an oxygenated, low Ca_2^+ ACSF semi-frozen slushy for approximately one minute prior to dissection of the hippocampus The low Ca_2^+ ACSF contained (in mM): KCl, 2.8; D-glucose, 10; NaHCO3, 26.2; NaH2PO4, 1.25; CaCl2x2H2O, 0.5; MgSO4, 7; Sucrose, 210. The isolated hippocampi were cut into 400-μm transverse slices using a tissue chopper. The slices were temporarily placed in a chilled, oxygenated solution of the same low Ca_2^+ ACSF until all the slices had been made. The slices were then

transferred using a sable paint brush to a pump-circulated incubator containing oxygenated ACSF at room temperature which was then slowly brought up to 35°C. The ACSF in the incubator contained (in mM): NaCl, 126; KCl, 2.8; NaH2PO4, 1.25; CaCl2x2H2O, 2; MgSO4, 1; NaHCO3, 26.2; D-glucose, 11. The slices were incubated for approximately 1.5 h before the recordings started. An incubated slice was transferred to a submersion-type recording chamber that had been temperature-acclimated with oxygenated ACSF of the same concentration as the incubating ACSF using gravity flow to pass the solution through an in-line heater, into the recording chamber.

Apparatus

The apparatus was composed of a perfusion recording chamber, with an in-line heater (Warner Instruments, model TC-324B), mounted to an Olympus BX51 epifluorescent microscope equipped with a Retiga EXi CCD camera model Fast 1394, a Lumen 200 Fluorescence system, a Photometrics Dual View splitter, and a Ludl shutter and filter wheel (570 nm). Optical measurements of the oxygen dye required filters in the ranges of 620 and 760 nm. The microscope was combined with a custom-built 35MHz Olympus NDT focused ultrasound (FUS) transducer model PI-35, Olympus 5073PR pulser/receiver, an E&I power amplifier (20 Watts Linear, 45dB 150kHz - 300MHz, model 420 LA RF), 2 function generators, one of which was an Agilent 33600A (capable of running the 35MHz transducer), and a Tektronix TDS 1001B two-channel oscilloscope. Potassium was measured using a Warner Instruments HiZ-223 high-impedance amplifier. Tissue was electrically stimulated using an A-M system isolated

pulse stimulator (model 2100). The apparatus was housed in a fully-enclosable, light-proof Faraday cage on top of a TMC air table.

Focused ultrasound and microscope integration. The 35MHz FUS transducer was integrated into the microscope by replacing the microscope condenser with a custom-machined adapter to hold the transducer in place which allowed vertical and horizontal manipulation. A custom cuff was 3D-printed and combined with a latex balloon to create a movable fluid reservoir that enabled the transducer to interface with the tissue Figure 20 (see supplemental material for details). The transducer was co-aligned with the objective using a metal washer with nylon crosshairs approximately 30 μm thick. The transducer was connected to the pulser/receiver and the signal output was viewed on the oscilloscope. The crosshairs were centered on the screen and the transducer was first vertically aligned to find the largest signal indicating that it was within the focal range. The transducer was then aligned horizontally by adjusting the knobs normally used to move the condenser in the X,Y direction until the maximum peak created by the intersection of the crosshairs was located and coincided with the image on the screen. Once the the transducer was coaligned with the objective it was disconnected from the pulser/receiver and connected to the E&I amplifier.

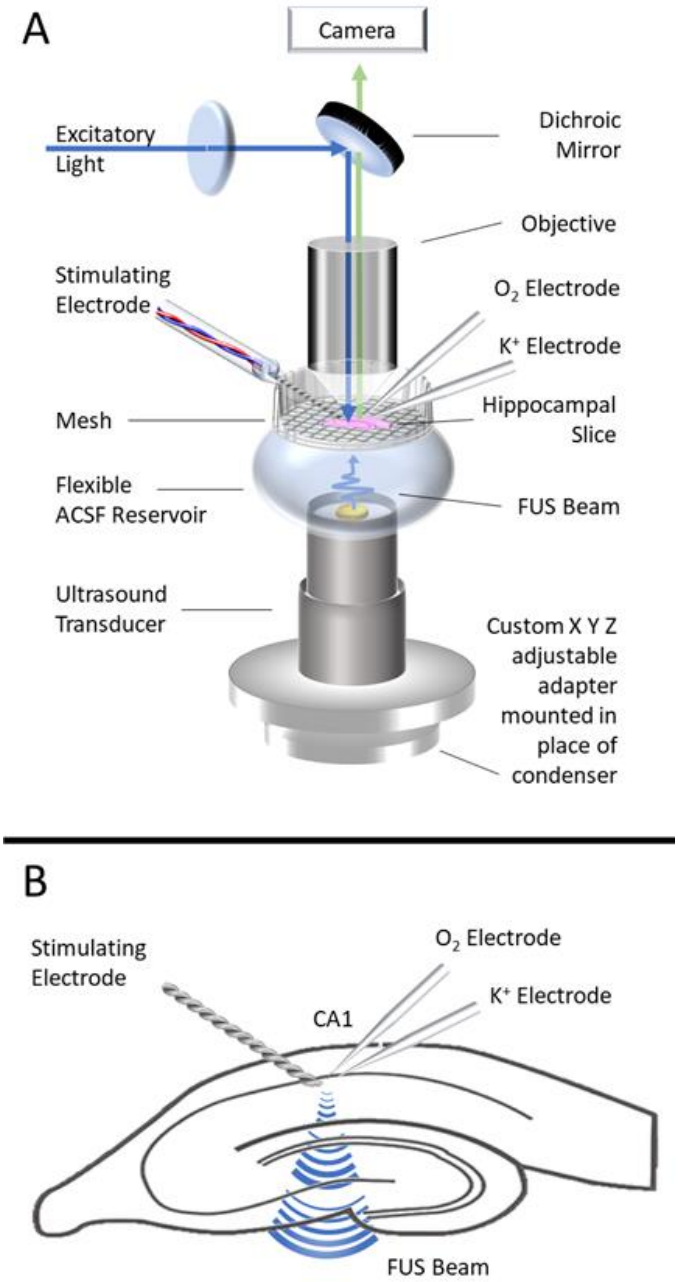

Figure 20: Apparatus and experimental schematic.
Panel A shows a schematic of the apparatus. The hippocampal slice is placed on a mesh in a custom perfusion well over a flexible ACSF reservoir. The transducer is joined to the reservoir with a custom water-tight cuff and mounted to a custom XYZ adapter that replaces the microscope condenser. The transducer is co-aligned to the objective to be able to visualize the XY placement of the focal point on the slice. The Z component is calibrated by placing a metal washer in the well and moving the condenser holder along the Z plane to find the maximum wave form on an oscilloscope. Panel B shows a close-up of the electrode positioning in the slice. The O_2 and K^+ electrodes are placed in close proximity to each other in the cell body layer of the CA1 region whereas the stimulating electrode is placed in the stratum radiatum. The FUS beam is focused on the stratum radiatum as well.

Electrode preparation.

Stimulating electrodes. Twisted pair bipolar stimulation electrodes were fabricated from 75/~m platinum wire insulated with Teflon (Medwire, Mt. Vernon, NY).

Oxygen/Reference electrodes. Oxygen-sensitive electrodes (optodes), capable of simultaneously collecting optical oxygen readings as well as electrical data were fabricated in-house, as described in Ingram et al., 2013. The optodes were constructed of pulled borosilicate glass micropipettes which were dipped in an oxygen-sensitive polymer matrix. The matrix was prepared by dissolving 22mg of polyvinyl chloride (PVC) and 44mg bis(2-ethylhexyl) ester (DOS) in 0.5 mL of tetrahydrofuran (THF) and sonicating until emulsified. Stock solutions of THF containing 0.98 mg of Pt(II) Octaethyl Porphine Ketone (PtOEPK) (Frontier Scientific) and 0.05 mg BODIPY 577/618 maleimide (Invitrogen) were added to the plasticized PVC and evaporated to 1mL (Hartmann & Trettnak, 1996). The pulled micropipettes were attached to an adapted syringe and pressurized with air to prevent the tip from being clogged with dye. Air pressure was maintained while the tip of the micropipette was dipped 10x into the dye matrix. The coated micropipettes were allowed to dry, and the tips were rinsed with deionized (DI) water to remove any excess THF. The dried micropipettes were filled with ACSF of the same composition as was present in the recording chamber and tested at the time of use to ensure a resistance of 2-8 MΩ.

Potassium-sensitive electrodes. Potassium-sensitive electrodes were also made in-house as described in (Ammann et al., 1987). The electrodes were constructed of pulled borosilicate glass micropipettes *without filament*. The glass pipettes were filled with 9 μL

of Sigmacote and suspended over low heat for approximately an hour. The remaining Sigmacote was blown out of the pipette tip using tubing connected to an air supply. The pipettes were suspended over low heat for another hour and then left to dry overnight. The next day, the pipettes were inspected under a microscope to ensure that they were completely clear indicating that they were dry. Once dry, the pipettes were filled with 6 μL of Sigma-Aldrich Potassium ionophore I- cocktail B and gently back-filled with 100 mM KCl solution.

Stimulation parameters

Electrical stimulation. The stimulating electrode was placed in the region of the stratum radiatum near CA1. Stimuli were applied under computer control, in randomized sets of intervals consisting of: one stimulus per 1 min., 30 s, 20 s and 10 s, using a train burst width of 2 s, pulse duration of 1×10^{-3} s, inter-pulse period of 2.5×10^{-2} s and an output of 150 – 200 μA.

FUS stimulation. The focal point (140 μm diameter) of the transducer was placed in the stratum radiatum near CA1. Stimuli were applied under computer control, in randomized sets of intervals consisting of one stimulus per 1 min, 30 s, 20 s and 10 s, using a train burst of 700 kcycles at pulse repetition frequency of (PRF) 10 Hz and an output of 150 mVpp with stimulation durations ranging between 0.1 – 2 s. Alternate protocols may have used 350 or 175 kcycles as indicated in the results section Figure 12.

Electrical stimulation modulated by FUS. The stimulating electrode was placed in the region of the stratum radiatum near CA1 and the FUS focal point was aligned to the same spot on the tissue (Figure 20). Baseline was recorded for 1 minute before

electrical stimulation was applied every 3 minutes using a train burst width of 2 s, pulse duration of 1 X 10^{-3} s, inter-pulse period of 2.5 X 10^{-2} s and an output of 150 – 200 µA. FUS stimulation was initiated at 12 minutes after the start of the recording between the 4^{th} and 5^{th} electrical stimulus and stopped after 11 minutes between the 22^{nd} and 25^{th} electrical stimuli. Electrical stimulation continued for an additional 9 minutes after cessation of FUS modulation and the tissue was allowed to return to baseline for 6 minutes after electrical stimulation stopped. Electrical responses were recorded.

Inhibition of physiological responses by NaCN

Modified ACSF containing 1mM NaCN and 10 mM D-Glucose, which is closer to physiological levels of glucose, was introduced into the perfusion chamber at a designated time using a separate shunt added to the main gravity-flow line of ACSF. It is important to note that higher levels of glucose will prevent NaCN from having a notable effect on cell response (Tian & Baker, 2000). The modified ACSF contained in mM: 126 NaCl, 3.0 KCl, 1.4 KH2PO4, 2.4 CaCl2, 1.3 MgSO4, 26 NaCO3, and 10 glucose. The slice was perfused with modified ACSF without NaCN for 5 min to collect baseline measurements. The modified ACSF containing NaCN was added to the perfusion for 10 min to induce anoxia. At the end of 10 min, the perfusion was switched back to modified ACSF without NaCN for the remaining 65 min.

Thermal Measurements

A thin-wire (Omega) thermocouple was inserted horizontally into an agar phantom submerged in an ACSF bath at room temperature. The transducer was mounted on a computer-controlled motorized-stage assembly and raster-scanned in steps of 0.5

mm using a train burst of 700 kcycles at pulse repetition frequency of (PRF) 10 Hz and an output of 150 mVpp. Stimulation duration was matched to experimental protocols in a range of 0.1 – 2 s. Three randomized temperature measurements of each stimulation duration were obtained with and without perfusion flow. The data were collected using an in-house Labview program.

Recordings

Extracellular recordings were made by placing the optode and potassium-sensitive electrode in very close proximity to each other in the cell body layer of the CA1. Optical data were recorded using IP Lab software. Potassium and electrical data were recorded using an in-house Labview program.

Data processing and analysis

All data and statistical analysis were processed in Matlab. All statistical analyses were performed using a one-way ANOVA.

Computational Model

See Chapter 4 of this dissertation for full details.

Contributions

Performed Experiments: Monica La Russa Gertz

Developed model: John Robert Cressman and Monica La Russa Gertz

Literature search: Monica La Russa Gertz

Wrote chapter: Monica La Russa Gertz and John Robert Cressman

Edited chapter: Monica La Russa Gertz, John Robert Cressman

CHAPTER FOUR: MODELS OF IONIC PERTURBATION AND METABOLISM

In the previous two chapters we compared the experimental and computational results after the addition of a metabolic module in Chapter Two, followed by the addition of the volumetric module in Chapter Three and saw that they correlated well. In addition to elucidating the effects of ARF in ultrasound stimulation, the model helped to reveal an interesting metabolic response to stimulation, namely an ionically mediated suppression of astrocytic energy consumption that resembles the Crabtree effect. In this chapter we describe the development of this computation model and the mechanisms behind it in greater detail than in the previous chapters.

Introduction

A computational model is an essential tool to guide experiments through predictions as well as to interpret experimental findings; especially when investigating novel techniques, and unexplained phenomena. A computational approach has the advantage that it can explore myriad scenarios of a particular hypothesis in less time, and with less effort and cost than experiments. Moreover, simulations can test the limits of a system that may not be possible experimentally.

Our model explores the known phenomenon of acoustic radiation force (ARF) as it relates to the spatiotemporal response of brain tissue to FUS stimulation (Nightingale, Soo, Nightingale, & Trahey, 2002). In brief, the model represents a cylindrical area of tissue within the focal region of the transducer, containing astrocytes, neurons, and interstitial space, which is compressed during FUS stimulation. The simulation also

accounts for ionic solution in the interstitial space and surrounding bath, as well as non-mobile osmotic agents in the interstitium. The neuronal and glial compartments are modified conductance-based Hodgin-Huxley-type models described previously in Cressman *et al.*, 2009 (which will also be discussed in greater detail in the Membrane Dynamics section).

The model describes ionic and electrical responses to ultrasonically induced volumetric changes that lead to osmotic changes in tissue due primarily to immobile but osmotically active agents in the extracellular space. This draws water into the interstitial space lowering the local ionic concentrations. It can be shown that a simple reduction of extracellular concentrations will lead to a conductance dependent shift in the membrane potential. For typical leak conductances, this leads to depolarization of the compressed tissue. To encode these interactions, we include four modules for Ionic Molar Dynamics, Membrane Potential Dynamics, Metabolic Dynamics and Volumetric Dynamics.

Volumetric Dynamics

This section describes tissue compression as it relates to the mechanisms of ARF during FUS stimulation. The physical effect of ARF is to produce a localized body force within the tissue at the focus of the ultrasonic radiation. This body force produces a well described deformation of the neuronal tissue (Nightingale et al., 2002) that we model here as a simple rate of change in the volume of the extracellular space. To visualize this effect, imagine packing a room with bubbles. Then very carefully add some water to a bubble deep in the middle of the space. The added weight will require more force from below to hold it up and therefore the bubbles below would become compressed and the

ones above expanded. For FUS the region of focus selects the region of the 'heavy bubble' and this segment of tissue experiences the added body force which is akin to the added weight in our analogy. For our ex vivo experiments the tissue slices are of comparable thickness to the size of the region affected by the radiation force. Therefore, we do not have the spatial localization needed to see the expansion effect. The changes in extracellular volume do not directly affect the extracellular ion concentrations as similar ionic solution is shifted from one interstitial space to another, or in the case of ex vivo experiments, the local bath. However, non-mobile, osmotic agents, such as hyaluronan and other large molecules, remain in place. Even in small concentration these agents can have profound effects on the local osmotic pressure if the extracellular volume becomes greatly reduced.

Differences in osmotic pressure between the local extracellular spaces as well as with their intracellular compartments induces osmotically based volume fluxes as water flows from the lower solute concentration to the higher solute concentration in the compressed interstitial space. An osmotic change is established in regions where the volume was increased as well and, although we do not believe our tissue preparations are thick enough to observe expansion, the model has been designed to address the results of ex vivo experiments where such effects should be present.

FUS stimulation in the model initiates a compressive force for 20 ms that decreases the tissue volume in the focal region as a function of time. We used data from previous studies to guide our simulation of volume flux in brain tissue as described in this section. We begin by modeling the effect of a single tone burst comprised of 700 kcycles

with a 50% duty cycle at 150 mV p-p and a 35 MHz central. The linear compression of tissue under the action of ARF has been measured in response to localized radiation force (I_{SPTA} ≈0.1 W/cm2) (Nightingale et al., 2002; Palmeri & Nightingale, 2011). From these measurements, and our ultrasound parameters we were able to approximate the compression for a slice with thickness of L =500 μm to be ΔL (-1 μm). From this value of linear compression, we can estimate the volume contraction using the following first-order approximation:

Equation 1

$$\frac{\Delta V}{V} = (1 - 2\nu)\frac{\Delta L}{L}$$

Where V is the volume of the focal region of the transducer, defined by $\pi r^2 l$, r (70 μm) is the radius of the focal area of the transducer and l (500 μm) is the depth of the focal region Figure 24. Lippert et al., 2004 gives an approximate value of 0.4 for the Poisson Ratio (ν) in brain tissue. Using these parameters the relative volume change (ΔV) over the course of a single tone burst is approximately -3,080 μm3 for a 500 μm-thick slice of brain tissue (Figure 21, Figure 22 and Figure 23). Since the extracellular volume cannot become negative, a phenomenological term is included to suppress the volume current as the volume approaches zero. This term can be understood as both a necessary cut off due to our assumption that cellular membranes maintain their integrity as well as significant constrictions in the extracellular paths communicating between neighboring spaces. This latter term is known as the tortuosity and can be modeled as the length of the path an ion follows in the extracellular space (Simonova et al., 1996).

The transmembrane osmolar volume flux of water is modeled on diffusion, and based on volume current density as: $J=LpRT*[H_2O]$, where J is the flux in volume current density, and is the product of the filtration coefficient (Lp), the gas constant (R), temperature (T), and the change in osmolarity $[H_2O]$ (Fettiplace & Haydon, 1980).The osmolar volume flux between the bath and extracellular space is based on Fick's first law of diffusion, where the flux between bath and extracellular space is based on the difference of the total number of ions and non-mobile osmotic agents between the extracellular space and bath over the distance between the extracellular space and the bath, with respect to the rate of diffusion of water.

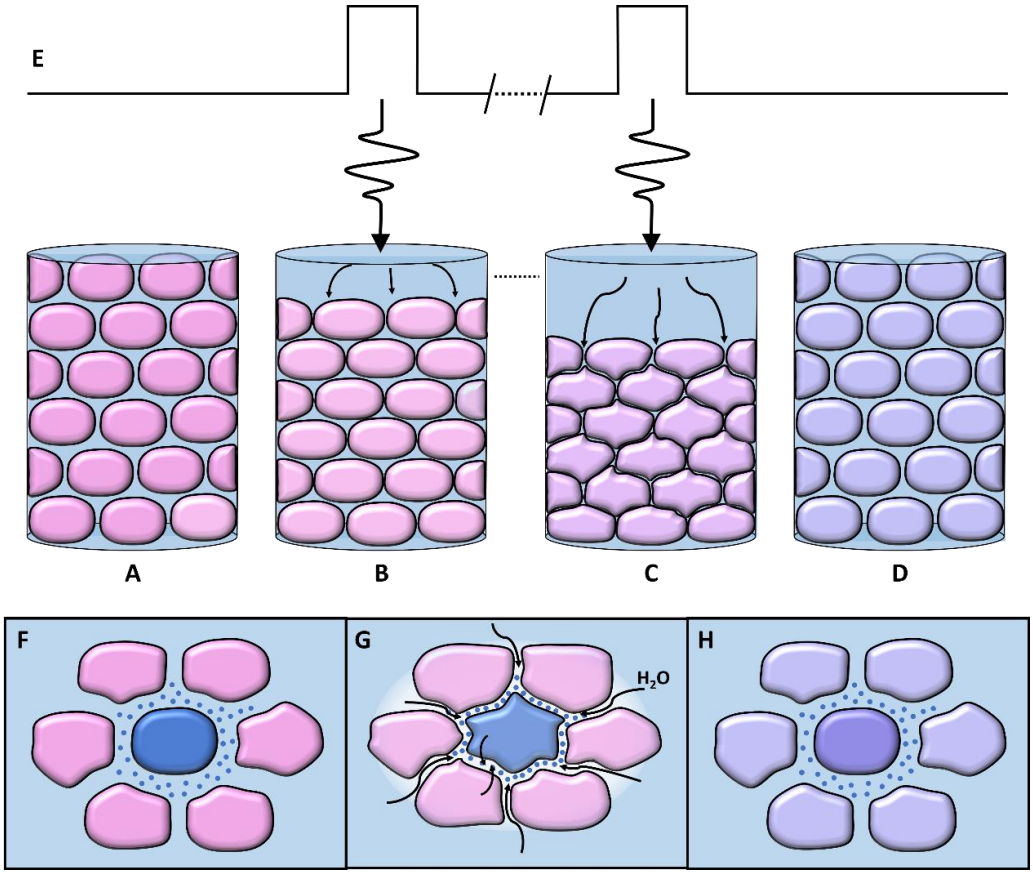

Figure 21: Model scheme of compression.
A - D represent the same section of tissue inside the focal area of the acoustic beam. E is time trace of the acoustic pulse. The blue background is the ionic bath solution containing K^+, Na^+, Ca^{2+} and Cl^-.

A is the tissue before stimulation. B and C show the progressive compression of the tissue during stimulation, and D shows the tissue re-expanding after stimulation stops. B also shows increased tortuosity in the extracellular space as compared to C. In B, C, and G black arrows show H_2O flowing from the ionic bath solution into the extracellular space due to osmotic gradients created by non-mobile osmotic agents.

Panel F shows a neuron surrounded by glia in uncompressed tissue before stimulation. Panel G illustrates the decrease in extracellular space due to compression. Panel H shows the cells re-expanding after stimulation. The resulting changes in ion gradients leave the tissue altered after stimulation, which leads to changes in excitability.

To understand this depolarizing effect, we simply need to understand the effect of a volume increase on the resting membrane potential. To derive the resting membrane potential, we start with the following equations that govern the voltage and ionic concentrations inside the cell.

Equation 2

$$\boldsymbol{\frac{dV}{dt}} = (1.0/\text{Cm}) * (\text{-Ina-Ik-Icl-}\boldsymbol{I_{Pump}})$$

Equation 3

$$\frac{dNa}{dt} = (ccon) * \left((-Ina - 3.0 * I_{Pump})\right)$$

Equation 4

$$\boldsymbol{\frac{dK}{dt} = ccon * \left((-Ik - Icc + 2.0 * I_{Pump})\right)}$$

$$\boldsymbol{\frac{dCl}{dt} = ccon * \left((Icl - Icc)\right)}$$

After setting these equations to zero and eliminating the pump current we arrive at an equilibrium condition only dependent on the conductances and reversal potentials of the ions.

Equation 5

$$-Ina/3.0 = (Ik + Icl)/2.0 = I_{Pump}$$

$$\text{-Ina-Ik-Icl}+Ina/3.0$$

$$\text{Ik+Icl}+2Ina/3.0 = 0$$

The resting membrane potential can now be isolated and expressed in terms of the conductances and reversal potentials:

Equation 6

$$V = \frac{2g_{Na}V_{Na}/3 + g_kV_k + g_{cl}V_{Cl}}{g_{cl} + 2g_{Na}/3 + g_k}$$

By expressing the reversal potentials in terms of concentrations, we can obtain the resting potentials dependence on the change in extracellular volume alone. This dependence models the effect of the osmolar flow that changes extracellular volume, but not ion number, the main result of the FUS stimulation.

Equation 7

$$V_N = 26.64 \ln((\mathrm{NNo}/\nu)/\mathrm{Ni})$$

Equation 8

$$\frac{\boldsymbol{dV}}{\boldsymbol{dv}} = \frac{\boldsymbol{26.64mV(-2g_{Na}/3 - g_k + g_{cl})/\nu}}{\boldsymbol{g_{cl} + 2g_{Na}/3 + g_k}}$$

Equation 9

$$\boldsymbol{\gamma = -2g_{Na}/3 - g_k + g_{cl}}$$

Finally, the parameter determines whether the effect of the FUS stimulation will be excitatory, $\gamma > 0$ or inhibitory, $\gamma < 0$.

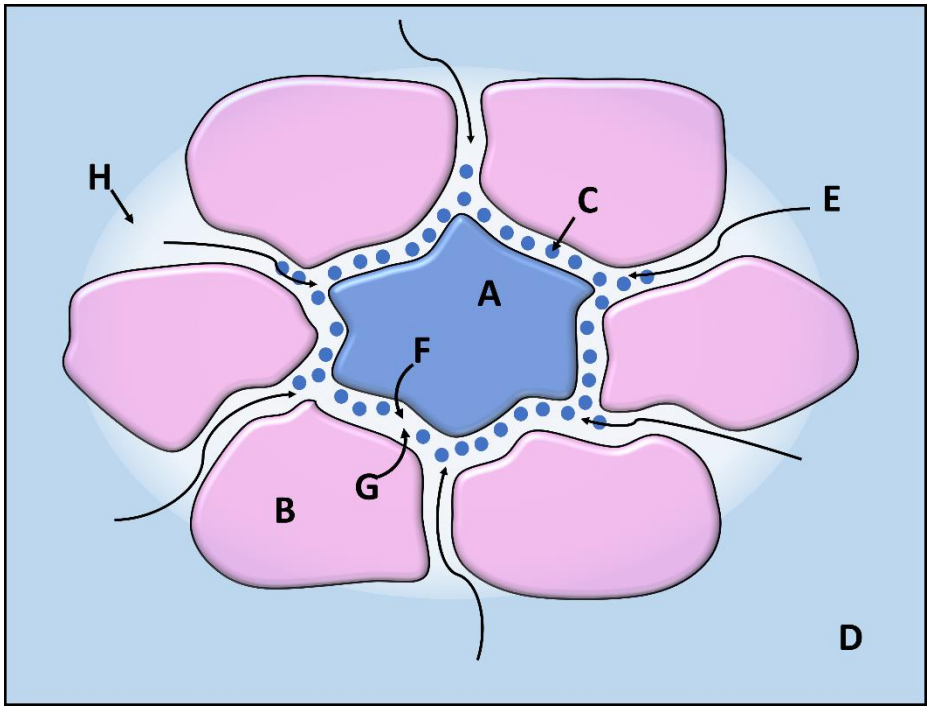

Figure 22: Close-up of modeled mechanisms during FUS compression.
A represents a neuron surrounded by astrocytes (B). C is one of many immobile osmotic agents (such as proteins, or other large molecules like hyaluronan, for example) that are not flushed out of the interstitial space with the other ions in the bath during compression. D is the ionic bath solution. E is the flow of H_2O down the osmotic gradient created by C. F and G are osmotically induced transmembrane fluxes as H_2O moves from the intracellular space of neurons and astrocytes to the extracellular space. H is the transient area of lower ion concentration created by the osmotic flow of H_2O created by E, F, and G.

During compression, the ionic solution is pushed out of the interstitium into the bath as the extracellular space decreases, and the tortuosity increases. The reduced extracellular space combined with the immobile molecules that remain, create an osmotic gradient that draws H_2O back in to the same space creating a dilute local environment that contains a far lower concentration of K^+, Na^+, Ca^{2+} and Cl^-.

The tissue also possesses elastic properties (Franceschini, Bigoni, Regitnig, & Holzapfel, 2006; Fung, 1993; Galford & McElhaney, 1970). This effect is modeled as a simple bulk modulus that acts to draw of extracellular fluid into the extracellular space making it both a volume and ion exchange with the neighboring bath compartment. These osmolar volume fluxes combine to create a volume current, where the glial and neuronal transmembrane aqueous volume fluxes, along with the extracellular and bath aqueous

volume flux, and the total change in tissue volume, are affected by the FUS stimulation and the intracellular volume change.

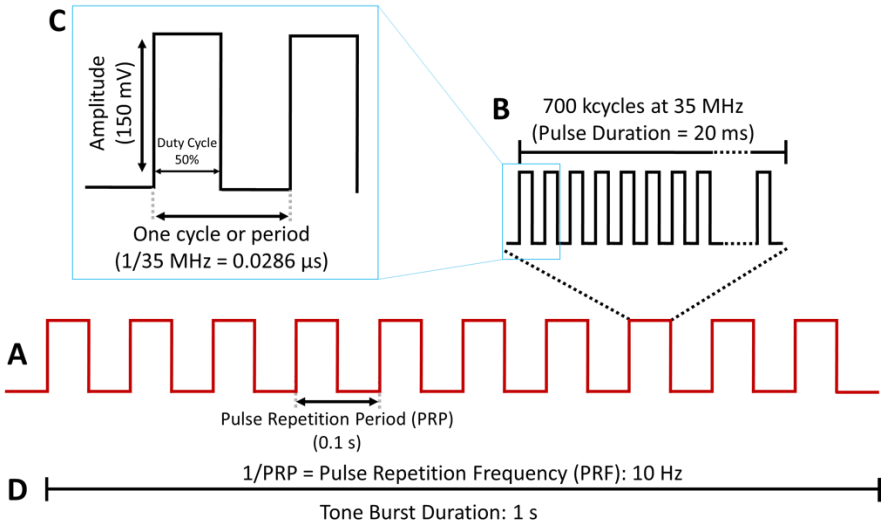

Figure 23: Stimulation protocol.
The model simulates the compressive effects of a series of pulses at a PRF of 10 Hz (A). Each pulse is comprised of 700 kcycles at 50% duty cycle, and measures 20 ms in duration (B). Each cycle oscillates a central frequency of 35 MHz, with a period length of 0.0286 µs and an amplitude of 150 mV (C). However, the tone burst duration can vary depending on how many pulses are applied in a single burst (D).

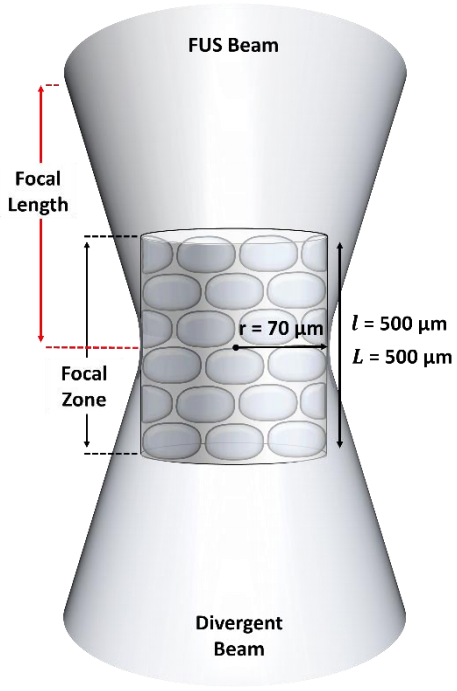

Figure 24: Model of focal region.
The bioeffects of FUS occur in the focal region of the beam. The center of the focal region is also the narrowest point of the beam where the sound waves from the transducer converge. The distance from the transducer and this point is the focal length, which varies which each transducer type. Once the acoustic waves pass the center of the focal region, they begin to diverge. No bioeffects can occur in the fully divergent area as the pressure is too diffuse. The area of the focal region calculated in the model does not replicate the hourglass shape of the beam. Instead it approximates the focal region using the equation of a cylinder, where r is the radius of the beam at the focal length and *l* is the length of the focal region. The length of the focal region also coincides with the thickness of the tissue slice (L).

Ionic Molar Dynamics

The changes in osmolarity due to volume compression described in the previous section leads to a re-distribution of ion concentrations. The ionic molar dynamics section describes the flow of ions between intra- and extracellular spaces in the affected tissue, and adjacent extracellular spaces during FUS stimulation. Ion fluxes are current flows measured in moles based on *diffusion* (due to concentration gradients) and *drift* (due to electrical gradients) of ions between different extracellular regions. This treatment is

equivalent to the Goldman, Hodgkin, and Katz formalism however, we analyze each flow separately so as to more clearly observe their dynamical roles. To match our experiments the adjacent space is assumed to be the bath and it is treated like an infinite reservoir for ions and oxygen.

The diffusive current is determined from the concentration gradients of ions between the extracellular space and the bath, over the distance to the bath, and multiplied by the rate of ion diffusion across the area between the extracellular space and the bath. Ion drift currents are modeled as Ohm's law, where the potential between the bath and the extracellular space is determined by the flow of ions between these spaces. The conductance and capacitance for the tissue is modeled after Butson and McIntyre, 2005.

Finally, the bulk volume flow due to the FUS body force moves ions equal to the concentration times the volume of the moving fluid. Although the concentration of the fluid may not change as it moves from space to space it is necessary to keep account of the total number of ions in each space as the volume is changing as well.

To translate the model to the in vivo condition we would need to explore the most relevant adjacent spaces for each of these flows. These could include the unaffected surrounding tissue, the vasculature, or between affected regions of compression and expansion. Although it is outside the scope of this work to explore these avenues, we will speculate on their relevance and potential impacts in the discussion.

Membrane Potential Dynamics

Both volumetric dynamics and ionic molar dynamics contribute to the membrane potential dynamics in this model. Membrane potential dynamics describe the electrical

changes in response to ionic redistribution as a result of compression. The equations are based on dynamic reversal potential (Nernst) equations for potassium, sodium, and chloride, along with full charge currents, ion pumps tuned to resting membrane potential for both neuron and glia, and voltage gated conductances for the neuron. The general equation is:

Equation 10

$$V=1/C\ (\sum I)$$

Where V is the transmembrane voltage, C is the membrane capacitance and ($\sum I$) is the sum of all the currents. Voltages are modeled to account for the transmembrane potential in the presence of an external bath potential. The transmembrane currents include leak and voltage-gated channels, cotransporters, and sodium/potassium pumps. Conductances for cotransporters, potassium leak channels, and basal pump strength were fitted from the model to established resting conditions.

Metabolic Dynamics

This compartment of the model describes the differing roles and interactions of glia and neurons with respect to energy production and consumption. The production of ATP used to maintain neuronal gradients is a downstream result of metabolism, which has two main components: glycolysis and oxidative phosphorylation. Experimental results demonstrate that the change in ATP/ADP ratios in neuronal cells does not change substantially during physiological stimulation (Baeza-Lehnert et al., 2019), therefore the metabolic dynamics included here have no feedback to the other cellular dynamics at physiological stimulation ranges. However, this strict control will not be possible for supraphysiological stimuli, so we investigated ATP dynamics for both canonical and non-

canonical stimulations. The model was used to employ both canonical and non-canonical mechanisms of ATP production. In this context canonical and non-canonical refer to whether ATP production is driven by the cytosolic ATP/ADP ratio, or by the direct utilization of ATP by the Na^+/K^+ ATPase respectively. The non-canonical model also incorporates an activity dependent interaction between the neuronal and glial metabolic dynamics.

It has been found that active brain tissue does not fully oxidize glucose but instead generates a local surplus of lactate. This phenomenon is termed "aerobic glycolysis" because excess glycolysis is occurring in the presence of oxygen. However, there are two known forms of aerobic glycolysis: the Warburg Effect and the Crabtree Effect (Figure 25). Though both involve augmented lactate production in response to higher glucose/oxygen consumption ratio, they are mechanistically different (Barros et al., 2020). The Warburg Effect can be interpreted as a deficit in the capacity of mitochondrial activity to inhibit glycolysis. Whereas the Crabtree Effect is the suppression of mitochondrial oxidative metabolism by glycolysis. A major site of such acute aerobic glycolysis is the astrocyte. It has been proposed that fast aerobic glycolysis observed in the brain may be part of a complex relationship between neurons and astrocytes whereby neurons induce surrounding astrocytes to produce and supply lactate as a substrate, thereby not only increasing local oxygen availability for the neuron, but also shuttling lactate to the neuron for additional oxidative fuel, thus maximizing information processing.

We modeled canonical metabolic activity by first modeling the ATP levels in the cells based on a basal consumption rate, the pump rates and an ATP/ADP dependent production rate. The final term was also used to determine oxygen consumption as it is related to the rate of ATP production, which is a combination of glycolysis and oxidative phosphorylation. The non-canonical mechanism has been proposed to include the inhibition of oxidative phosphorylation in glial cells, and glycolysis proceeds anaerobically to produce lactate, which is shuttled to the neuron making them no longer limited by glycolysis since they are receiving additional substrate from those astrocytes, therefore the maximal neuronal ATP production rate increases. The net effect of the metabolic model is a shift of oxidative phosphorylation from glia to neuron.

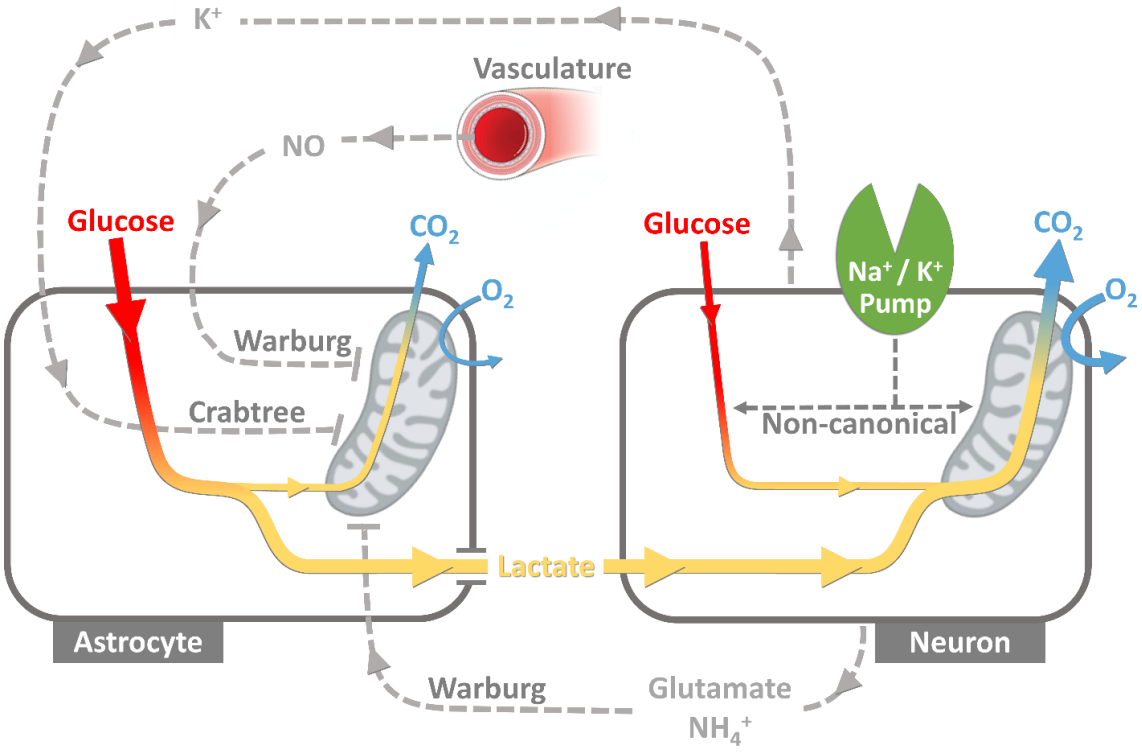

Figure 25: Acute activity-dependent aerobic glycolysis in brain tissue.
(adapted from Barros et al., 2019) Excitatory neuronal activity triggers the release of multiple small molecules, which act as intercellular metabolic signals. K+ stimulates astrocytic glycolysis leading to inhibition of respiration, a Crabtree effect. Neuronal glutamate and NH4 +, and endothelial NO, also inhibit astrocytic respiration, a Warburg effect. As a result, neurons are supplied with lactate and oxygen. Glycolysis and mitochondrial respiration in neurons are controlled by the Na+ pump, not by canonical mechanisms involving adenine nucleotides

Results

Simulated results reflect the same behaviors observed experimentally for both electrical and FUS stimulation.

The model was able to replicate the extracellular potassium response seen in the stimulation experiments. The model results were first compared to electrical stimulation, which is a well-known stimulation modality. The simulated results were able to replicate many of the prominent features of the oxygen and potassium responses to electrical stimulation and provide a mechanistic insight to the source of the observed behaviors.

The top right panel in Figure 27 shows the increasing potassium signal that reaches a maximum before decreasing the amplitude of the responses. This behavior may be understood in terms of the progressive change in the electrical response to stimulation. In the early stages of the stimulation train each stimulation pulse produces two spikes whereas towards the end it has been reduced to a single spike per stimuli. This is the most important effect in sculpting the response. However, the overall shape is also controlled by the shifting reversal potentials as will be explained further in the next section. The model was then able to simulate oxygen and potassium responses to FUS stimulation as well. Figure 26 presents the simulated results of FUS responses for potassium and oxygen. Here we see large potassium responses that compare well to experimental results in relation to the oxygen responses.

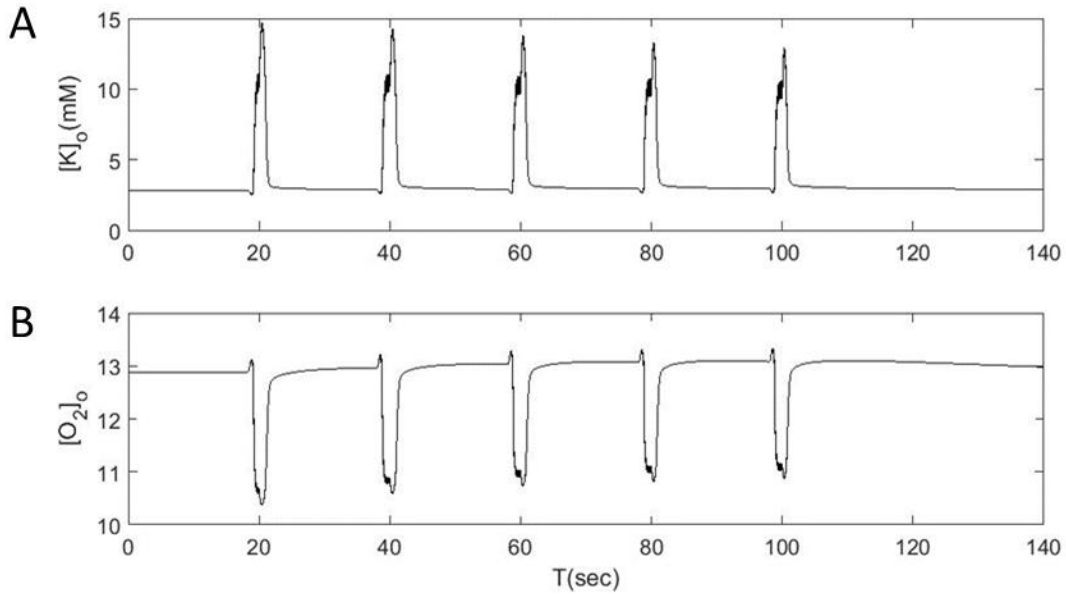

Figure 26: Simulated simultaneous oxygen and potassium responses to FUS.
Panel A is a simulated potassium response to FUS stimulation every 20 s with a 2 s stimulation. Panel B is the corresponding simulated oxygen response. Both the potassium and oxygen simulations compare well with the experimental results.

The next set of results deal with an investigation into neuronal metabolic dynamics in responses to electrical stimulation so that we can employ them in our model for FUS stimulation to assess its metabolic stress. At present these metabolic dynamics do not feedback into the previously discussed dynamics. Though it would be natural to makes the Na^+/K^+ ATPase dependent on metabolic output that is beyond the scope of this work.

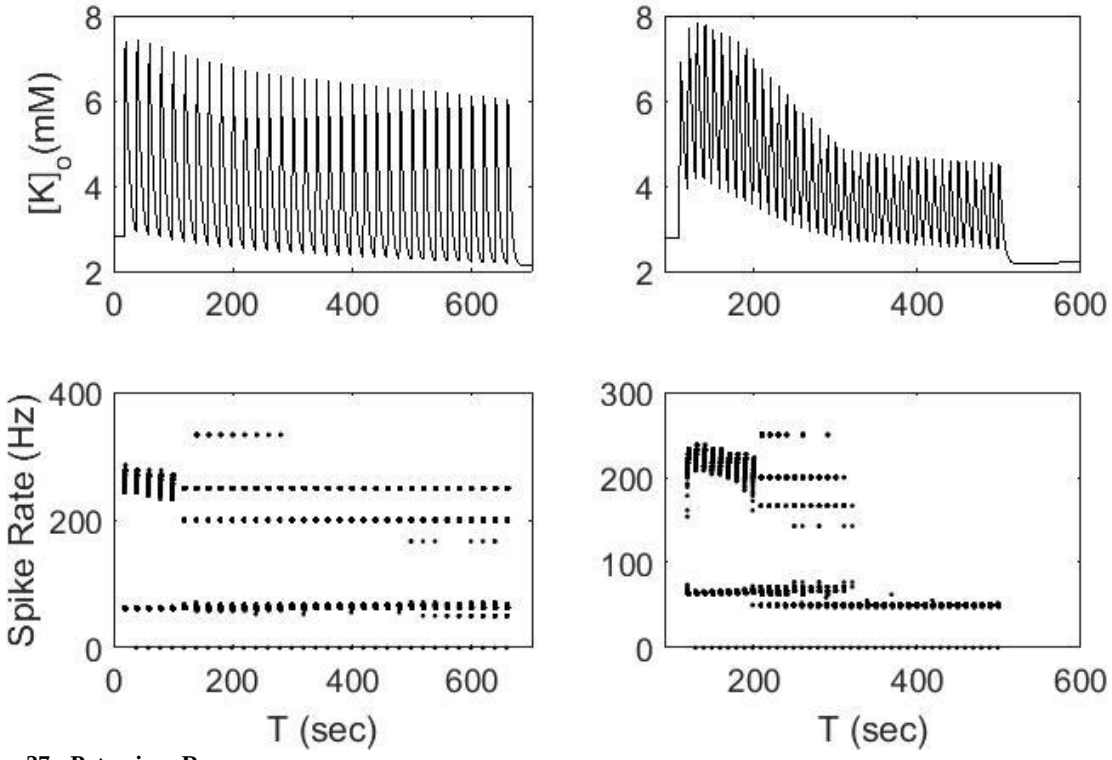

Figure 27: Potassium Recovery.
The top panles display the extracellular potassium concentration for potassium for interstimulus intervals of 20 seconds (left) and 10 seconds (right). The bottom panels show the instaneous spike rates for the stimulated neurons.

Simulated oxygen responses are independent of canonical and non-canonical roles of Na^+/K^+ ATPase.

We utilized the assumption that the Na^+/K^+ ATPase was the driver for metabolic production of ATP. Therefore, we investigated the pumping rates for the neuronal (orange) and glial (blue) cells as shown in the second row of Figure 28. For both stimulation intervals the glial cells show marked decrease in pumping activity as the stimulation progressed owing to the pumps depleting the internal sodium as seen by the yellow traces in the first row of Figure 28. The internal sodium levels for neurons

(orange) on the other hand display a more steadily increasing pumping rate as their internal sodium rises due to action potential generation.

The last row in Figure 28 shows the sum of the glial and neuronal pumping rates after weighting for their volumes, nearly two to one for the glia to the neurons. The qualitative features from the oxygen consumption from the data are captured by the model. Where for the 20 s stimulation intervals the ATP consumption reaches a steady state whereas the ten second intervals produce a maximum consumption rate that peaks shortly after the potassium as was found in the experimental results.

Model reveals an ionically mediated suppression of astrocytic energy consumption that resembles the Crabtree effect

Next, we incorporated dynamics to emulate the well-known Crabtree effect. To summarize, the effect entails an activity, perhaps extracellular potassium mediated, switch that limits aerobic metabolism in the glia to glycolytic producing lactate that can be utilized by the neuron. We therefore used a phenomenological switching function based on the extracellular potassium concentration that simultaneously reduced the glial oxygen utilization and increased the rate maximal rate of oxygen utilization in the neuron. The results of these added mechanisms can be seen as the brown trace in Figure 29. The blue trace is the result of the model before the addition of the switch. The result without this mechanism produced a response that was in better agreement with the data.

.

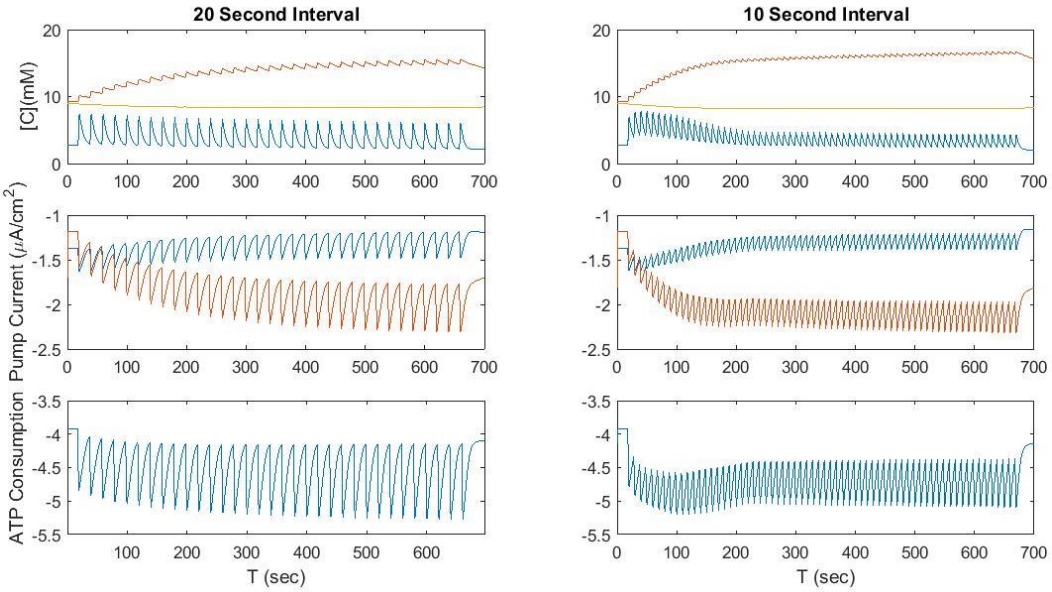

Figure 28: ATPase activty.
The top panels display the extracellular potssium concentration (blue) and the intracellular sodium concentrations for the neuron (orange) and glia (yellow) for 20 seconds (left) and 10 second (right) inter stimulus instervals. Second row of panels shows the rate of pump activty for the glial cells (blue) and neurons (orange), and the last row shows the sum of the individual currents after weighting by their relative volumes.

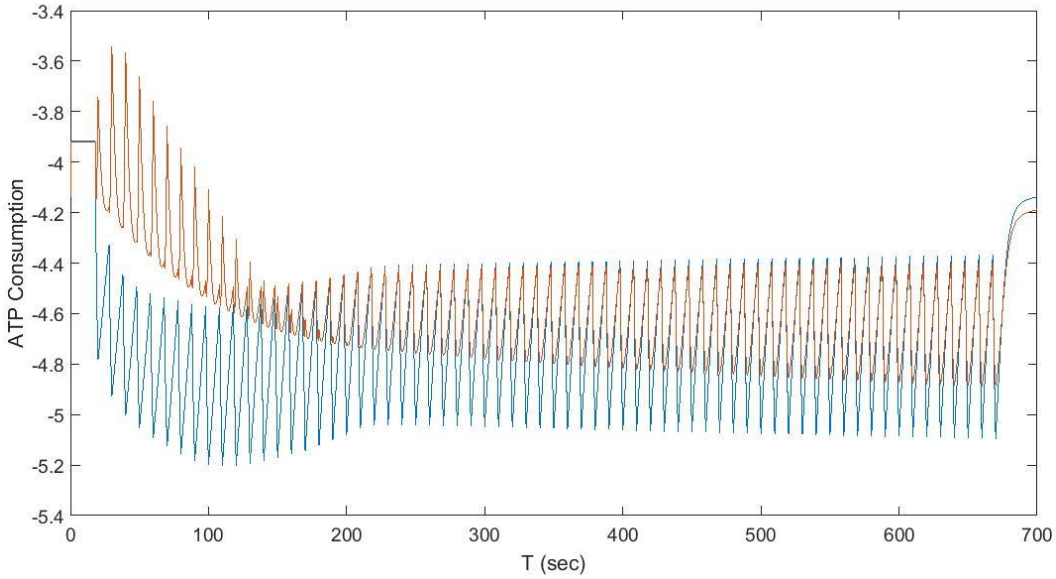

Figure 29: Canonical versus Non-canonical.
Blue curve depicts the ATP production for the canonical metaboic response, whereas the brown curve show the response when the activity-dependent metabolic swtich is imposed on the model.

Finally, we describe the effects of the canonical, non-canonical and activity switch on the available ATP levels in the cell. All three cases show nearly identical responses for the glial cells (light green) in Figure 30. Whereas the canonical and non-canonical responses are similar in shape, the canonical exerts a tighter control over the ATP concentrations. The switch on the other hand shows a much slower decrease in ATP concentration then the other two cases. This discrepancy may play a more important role when we include the ATP dependence in the pumping equations.

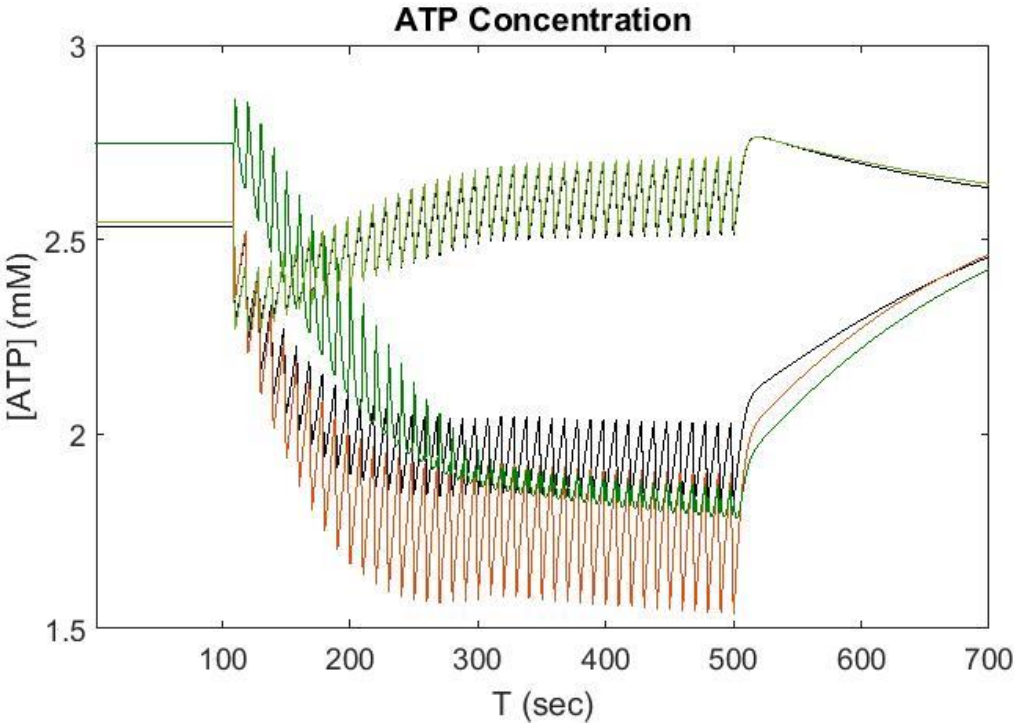

Figure 30: Cytosolic ATP Concentrations.
Here we display the intracellular ATP concentratoin for neuronal cells and glial cells for canonical, non-canonical pump drive, and non-canoncial pump drive and activity switch. All three glial currents are nearly identical and follow the light green trace.

Simulation describes the underlying ionic mechanisms leading to potassium and oxygen responses in response to ARF.

The main effect is due to spike generation as shown in Figure 31 below. The stimulation begins at 58 seconds and persists until 60 seconds. The early phase is characterized by a moderate drop in extracellular potassium accompanied by a gradual depolarization of the cell. Once threshold is reached, action potential generation is responsible for the bulk of the ionic fluxes. The reduced extracellular space enhances the effects of these flows on the extracellular concentrations, that in turn have a dramatic effect on the reversal potentials as shown in brown, blue and green for sodium, potassium, and chloride respectively.

As these three potentials along with their relative permeabilities, and to a lesser extent the pump current, determine the resting potential of the cell, their modulation affects the cell's excitability. In the initial phase the only reversal potential moving towards the depolarized state is that of chloride implicating this ion in the excitatory action of the stimulation. The action of the FUS stimulation is to reduce the extracellular concentrations of the ionic constituents by drawing water into the extracellular fluid. This has the effect of decreasing the chloride and sodium gradients, while temporarily increasing the potassium gradient. To further analyze the ionic effects on the membrane potential in the early phase we plot the change in the transmembrane currents in Figure 32. Here the brown, blue, green, and red traces are for the sodium, potassium, chloride, and pump currents across the membrane. The sum of these currents, plotted in black, is responsible for changes to the transmembrane potential. The summed currents are multiplied by a factor of five for effect and displayed as a black dashed line. The rapid increase in the sodium current at approximately 19 seconds is due to the initiation of spike generation.

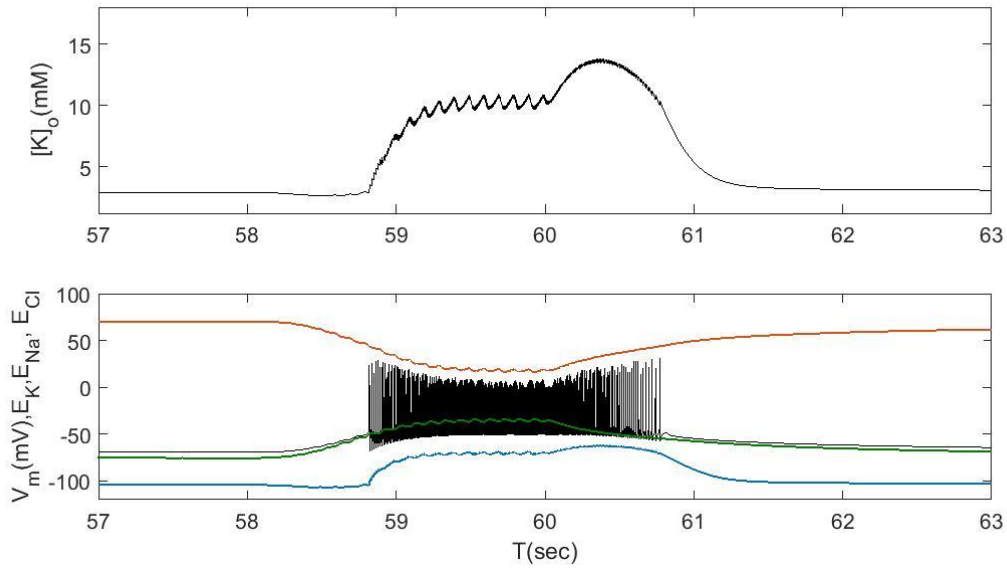

Figure 31: Model reveals that spike generations causes the main effects observed in FUS stimulation.
Panel A shows a single response to a 2 s tone burst. Panel B shows the reversal potentials for sodium (brown), chloride (green) and potassium (blue). The black trace is transmembrane potential. The stimulation begins at 58 seconds and persists until 60 seconds.

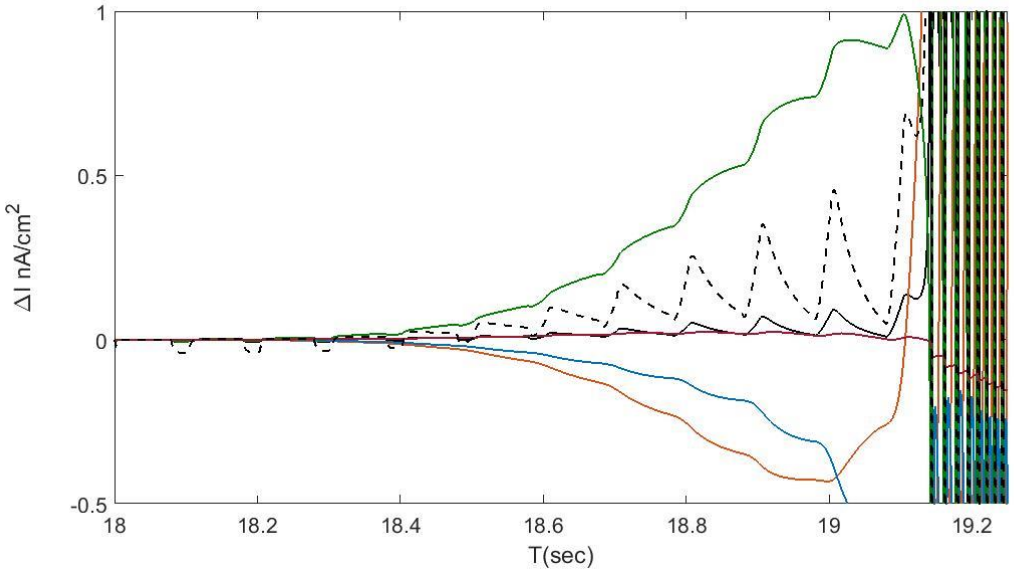

Figure 32: Change in Transmembrane Currents.
Transmembrane currents, with steady state subtracted off, during ultrasonic stimulous burst. The black curve represents the sum of the currents and the black dashed line is the same current multiplied by 5 for effect. The green, blue, brown, and purple curves are for the chloride, potassium, sodium and pump currents.

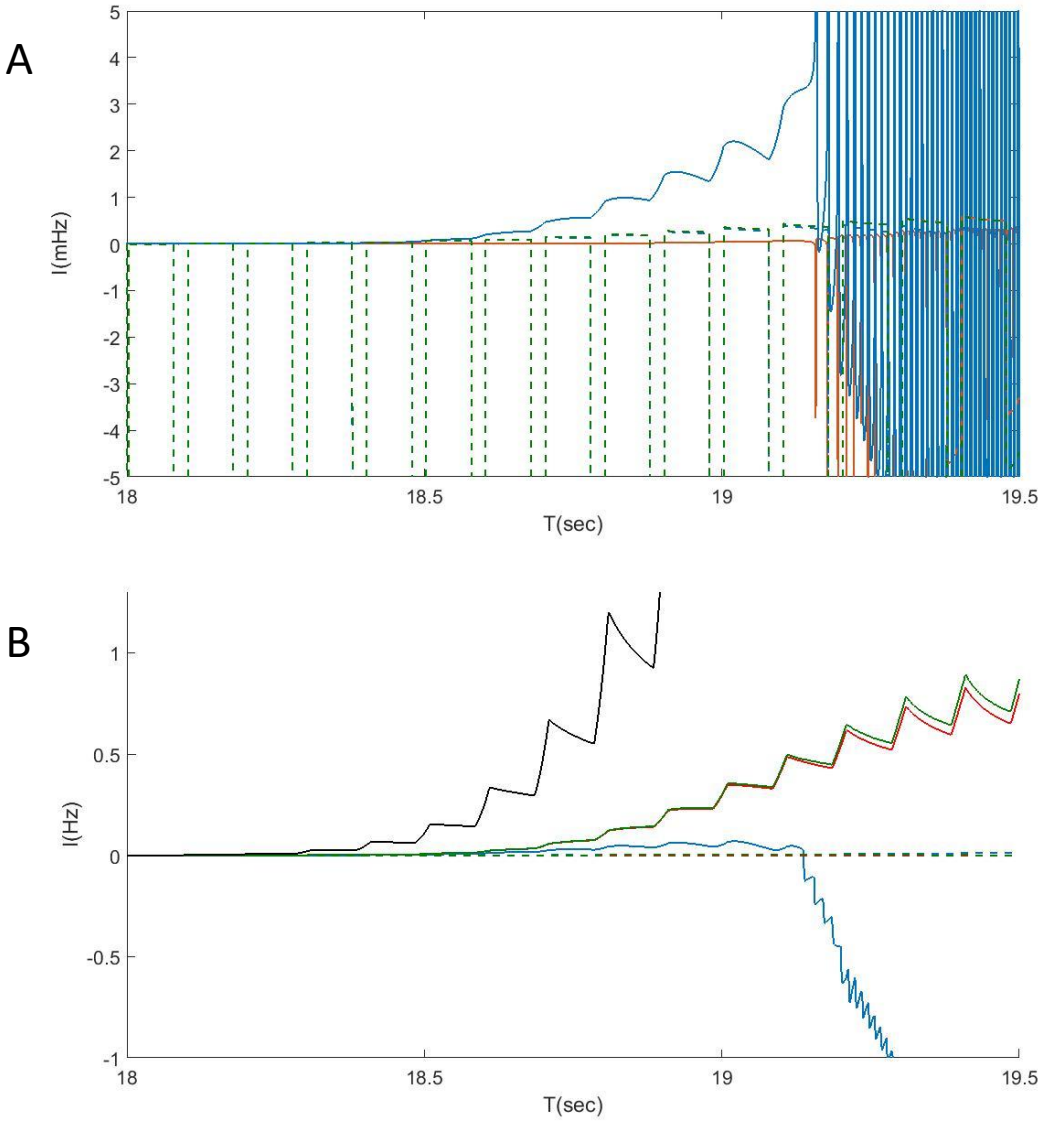

Figure 33: Extracellular Molar Currents.
Panel A. The composite concentration currents entering the extracellular space normalized by their steady state concentrations in the extracellular space. The three ions concentration currents with the bath are shown by dashed lines and are nearly on top of each other. The transmembrane components for potassium (blue) and sodium and chloride (brown). Panel B. The ionic exchanges with the bath. The black curve is due to the elastic expansion pulling bath fluid into the tissue. The red and green curves are for sodium and chloride respectively. The blue is for potassium and the dashed line are movement of ions due to the drift current.

Figure 33 shows the normalized molar currents exchanged with the extracellular space. Figure 33A shows the composite currents across the neuronal membrane, solid curves, as well as those exchanged with the bath, dashed curves. The currents have been normalized by their steady state concentrations in order to display their relative effects. The bath currents are dominated by the large negative currents produced by the FUS stimulation, but the positive osmotic flow is seen between stimulation events. The transmembrane currents are relatively small for the sodium and chloride currents, whereas the potassium flux across the membrane dominates the contribution to that ionic component. This large current is also responsible for shunting the depletion of potassium from the extracellular space.

Figure 33B shows the normalized ionic currents exchanged with the bath. Only the FUS depletion current is left out for clarity. The black curves show the effect of the fluid drawn into the extracellular space by the elastic expansion of the tissue. Once normalized by the steady state concentrations, all three of these currents lie on top of each other. The red, green, and blue curves show the diffusive currents entering the extracellular space from the bath. The sodium and chloride currents, red and green respectively, show increasing flow of ions into the space as the action of the FUS leaves their extracellular concentrations below that of the bath. The potassium current, in blue, on the other hand shows limited diffusion as the transmembrane current discussed in Figure 33A counteracts the FUS induced depletion of extracellular potassium. This limited diffusion leads to an imbalance between the ionic constituents and progressive depolarization of the membrane. The progressive depolarization occurs while the volume

increases due to the influx of water under the osmotic action of the high concentration of immobile agents. To understand the depolarization observed here, we simply need to understand the effect of a volume increase on the resting membrane potential. The reduction of concentrations for sodium and potassium cause their reversal potential to become more negative, but chloride rises towards zero and the net result depends on the relative conductances of the three ions. For the conductances used in this model, the net result is a depolarization of the membrane potential.

Model fails to simulate experimental results using other mechanisms.

The first panel of Figure 34 shows a number of results from our model implementing different stimulation strategies. The first panel shows the already described effect of volume contraction due to ARF. The accompanying red curve shows the response to an ARF-induced volume expansion. As with the contraction the expansion produces an increase in extracellular potassium. However, unlike the contracting condition, this effect does not produce an initial decrease in concentration. Furthermore, the expansion produces a potassium response that recovers towards baseline immediately after the cessation of stimulation. These key features of the experimental results, namely a non-monotonic response to stimulation and prolonged tissue response are not seen in any of the alternative methods of stimulation.

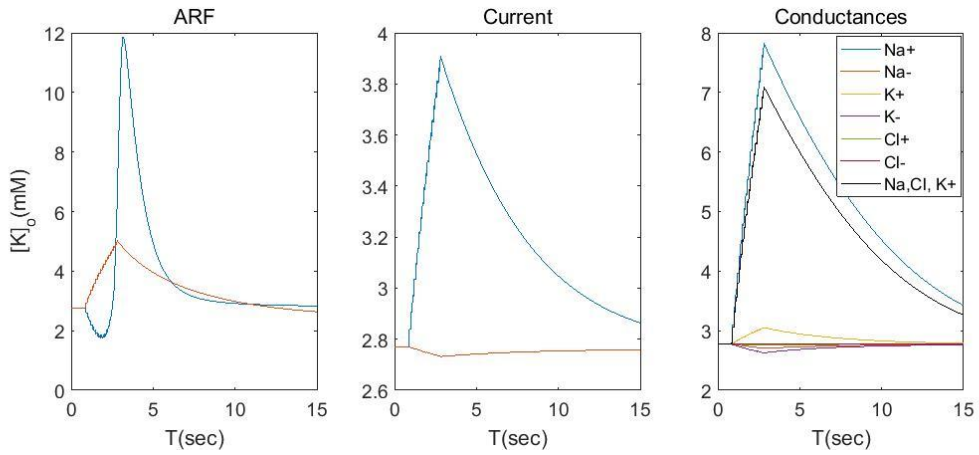

Figure 34: Extracellular potassium responses to ARF vs current and conductance as a mechanism. The "Y" axis is the extracellular potassium response to different potential mechanisms including ARF, current and conductance changes. Only ARF simulations can produce the non-monotonic responses seen in experimental data.

The middle panel shows the effect of a direct electrical current applied to the neuronal cells. The current is simply added to the transmembrane currents of the neuron and are activated during the span of the train burst to simulate a nondescript positive or negative current entering the cell due to the FUS. The blue curve is for a depolarizing current and the red curve a hyperpolarizing current. The depolarizing current shows the characteristic monotonic and unsustained responses seen in the expansive ARF stimuli, whereas the hyperpolarizing stimulus produces are relatively small decrease in the potassium concentrations.

We then modeled whether FUS interacts directly with ion channels in the membranes by making the sodium, potassium and chloride conductances dependent on the FUS activity. We modeled both FUS induced increases or decreases to these conductances first independently. The conductances for these ions were either increased

(indicated by a '+' in the legend) or decreased (-), during the application of the train burst. For all cases the responses were monatonic and unsustained. Furthermore, all of the responses are concomitant and therefore the sum of their effects will still not produce the stereotypical responses seen in experiments. The black curve demonstrates the effect of increasing all conductances during the FUS train burst. This protocol could either simulate direct protein interactions, or a general increase in conductance due to changes in the membrane due to either heating, cavitation or other fluid interactions. Either way, we have not been able to reproduce the characteristic potassium responses seen in experiments with any means other than ARF-induced tissue compression.

Discussion

We developed a model to address a set of empirical results from a study investigating the metabolic demands of ultrasound mediated neuronal stimulation. This is a promising new form of neuronal modulation. However, the lack of understanding of its mechanism of action undercuts the ability to rationally design safe and effective treatments. Our experimental results revealed that ultrasound stimulation can produce large extracellular ionic redistribution while imposing a relatively small metabolic response as compared with electrical stimulation. In order to understand this apparent contradiction, we developed a computational model endowed with mechanisms for volumetric, ionic, electrical, and metabolic dynamics.

The model was developed along with electrical, potassium, and oxygen measurements taken during electrical and acoustic stimulations in ex vivo slice preparations of rat hippocampus. Although our goal was to explain the discrepancy

between electrical and acoustic stimulation in terms of metabolic demand, our main result is the revelation of an osmotic mechanism underlying the depolarization of neuronal tissue through the compressive effects of acoustic radiation force. In addition, we were able to explain the large potassium responses as a result from the effects of spike-mediated transmembrane currents entering a reduced extracellular space due to ARF compression. Moreover, simulations failed to approximate experimental results when modeling other mechanisms such as current and conductances in the absence of ARF-induced volume changes. Finally, our development of the metabolic module led to the discovery of an ion-mediated metabolic switch that could explain the previously reported Crabtree effect (Barros et al., 2020; Fernández-Moncada et al., 2018).

The simulated results are achieved solely on the volumetric changes produced by ARF compression of the tissue.

We present a model that relies on a new mechanism for stimulation through the volumetric, ionic and electrical effects of acoustic radiation force. This is a very different mechanisms than those normally associated with ultrasonic stimulation, namely mechanically induced channel, membrane (Árnadóttir & Chalfie, 2010; Hamill & Martinac, 2001; Haswell et al., 2011; Orr et al., 2006; Syeda et al., 2016; Tyler, 2012), or thermal effects (Chapman, 1967; Guttman, 1966; J. C. F. Lee et al., 2005; Thompson et al., 1985). Our model reproduces the biphasic potassium response seen in our experiments, whereas these other mechanisms, such as currents or conductances do not produce this response as they produce responses more akin to our electrical model based on inducing conductance changes (Figure 34). There, we see neither the biphasic relationship, nor do we see the large ionic responses observed in experiments.

Simulated oxygen responses are independent of canonical and non-canonical roles of Na^+/K^+ ATPase.

We find that experimental oxygen measurements are consistent with our computational results regardless of whether we calculate the metabolic response based on pumping rates or the ATP/ADP ratio in the cytosol. These two metabolic drivers produce qualitatively similar responses with only a slightly lower level of ATP/ADP for the non-canonical case. The time course for the pumping rates initially follows the extracellular potassium concentration, however it is the intracellular sodium which sets the long time limit. It is the accumulation and depletion in the intracellular sodium concentrations for the neurons and glial respectively that drives their opposing metabolic trends reflective of the Crabtree hypothesis. And it is the sum of these two opposing metabolic trends that gives rise to the overall responses like those seen in the experimental results without the need of further sensing or control. However, this relationship may change if lactate is included in the model

The Crabtree effect appears to be an intrinsic ion-mediated metabolic phenomenon.

In addition to elucidating the effects of ARF in ultrasound stimulation, the model helped to reveal an interesting metabolic response to stimulation, namely an ionically mediated suppression of astrocytic energy consumption that resembles the Crabtree effect. The model implies that the mechanism for this Crabtree effect is based on the initial buildup of extracellular potassium which drives an increase in the pumping rate of the Na+/K+ ATPase in the astrocytes as well as the neurons. This, in turn, reduces the intracellular sodium in the astrocytes to the point that their pumping slows down and suppresses their ATP usage. This effect is based entirely on ionic dynamic and does not

require any other metabolic component involved in aerobic glycolysis, such as lactate, which is not modeled in this simulation.

Limitations of the model and future work.

The major limitation of this model is that it does not include lactate which would presumably increase oxygen consumption in the neuron by providing large amounts of additional substrate for oxidative phosphorylation as a result of oxidative phosphorylation from the ionically induced Crabtree effect we have presented here. This might improve the oxygen approximations in future simulations.

In conclusion, we find that the model approximates the large potassium extrusions in response to ARF as opposed to electrical mechanisms as is seen in our experimental results, while maintaining oxygen consumption in the scale of magnitude for both modalities. We further conclude that this model can be used to elucidate the constraints on neuronal activity in other stimulation modalities.

Contributions

Developed model: John Robert Cressman and Monica La Russa Gertz

Literature search: Monica La Russa Gertz

Wrote chapter: Monica La Russa Gertz and John Robert Cressman

Edited chapter: Monica La Russa Gertz, John Robert Cressman

CHAPTER FIVE: SUMMARY AND EXTENDED APPLICATIONS

Introduction

This dissertation presents an experimental and computational investigation into the metabolic demands on neuronal responses to focused ultrasound stimulation. It is presented in three parts: background and context, experimental approaches, and computational approaches.

Background and Context

The first chapter reviews the emerging role of FUS as a non-invasive brain stimulation tool for both basic research, and clinical application. The gaps in knowledge in this field are numerous. Not only are the mechanisms of FUS stimulation poorly understood, but there may be different mechanisms involved depending on the protocol and tissue type. Though most basic studies are focused on elucidating the mechanisms of acoustic stimulation, the need also exists to understand the concomitant effects of this platform. Since the field of acoustic neuromodulation is evolving from an ablative role in the clinical setting, and is now being tested on humans, the question of safety is paramount. Of all the research reviewed in this chapter, none have explored the metabolic demands of FUS stimulation on neuronal tissue, which can have profound effects on neuronal activity. Moreover, Chapter One also shows that there are very few computational models in this field, and the great majority are focused on the issues of localization and attenuation, with only three studies investigating the mechanisms of neuromodulation, and of those three, only one is accompanied by experiments to

corroborate the model. Like the experimental studies reviewed, none of the computational studies investigate the metabolic dynamics involved in acoustic neuromodulation either.

Experimental Approaches

Experiments inherently contain more variables, both known and unknown, as compared to a computational model. Experimental data can reveal unanticipated phenomena while also providing validation to computational hypotheses and speculation. In Chapter Two, I uncovered several unexpected behaviors during simultaneous measurements of oxygen and potassium. The data showed that oxygen recovery began to fail much earlier than potassium, and that the tissue developed a second steady state of oxygen consumption. The potassium recovery on the other hand, did not fail until the system was being driven the hardest at the shortest stimulation interval. At that point, both potassium and oxygen displayed another unanticipated behavior. Both averaged time traces reached a peak response at approximately 70 s after the start of stimulation, with potassium leading oxygen, after which the response levels declined, and remained at a lower steady state of response until the end of each experiment. This had no obvious explanation, except for perhaps changes in metabolic requirements or energy availability, which led to literature searches for mechanisms to model that would explain this phenomenon. This experimental finding eventually led to the addition of a metabolic component in the model, which corroborated the results by incorporating a non-canonical role for the sodium/potassium pump.

In Chapter Three, we delved into the unknown again. No one has ever investigated oxygen and potassium responses to FUS stimulation. There was no prior knowledge to guide this investigation. We had no idea what to expect or how to model it for predictions. The first poorly understood feature in the experimental data was the downward peaks present in the potassium responses, but not in the oxygen responses, that coincided with the acoustic pulses of the stimulation. Initially, we thought these were artifacts, but subsequent modeling showed that they were not, as will be explained in the next section. The other prominent feature in the experimental data to raise questions was the disparity in responses between electrical and FUS stimulation, as well as between oxygen and potassium within the FUS experiments. Again, because there was no prior information on this subject, we could not be sure if the stimulation range for FUS was simply not equitable to the electrical stimulation protocols, or if there was some other factor at play. These questions also provided fodder for tuning the model.

The last set of experiments in Chapter Four was used to validate a prediction from the tuned model indicating that the tissue remained in a transiently altered state of increased excitability after a stimulation burst. This suggested that electrically induced LFPs should be larger after the tissue had been primed with FUS stimulation. The experiments confirmed this.

Future experimental approaches can look into testing these protocols on microelectrode arrays in conjunction with electrical stimulation to see if cell cultures primed with FUS will show altered responses. Or perhaps testing modified protocols on

striatal slices instead of hippocampal slices to test the effects on dopamine release and long-term potentiation (LTP).

Computational Approaches

A computational model is an essential tool to guide experiments through predictions as well as to interpret experimental findings; especially when investigating novel techniques, and unexplained phenomena. A computational approach has the advantage that it can explore myriad scenarios of a particular hypothesis in less time, and with less effort and cost than experiments. Moreover, simulations can test the limits of a system that may not be possible experimentally.

In Chapters Two and Three we employ the same HH conductance-based model to elucidate and predict different elements of the experimental data. The main difference between the two applications is the contribution of the volumetric component of the model. In Chapter Two, we find that the addition of the metabolic component of the model is imperative to reproduce the same characteristic responses to electrical stimulation. Moreover, the metabolic component employs a non-canonical mechanism in which the Na+/K+ pump serves as the sensor that drives oxidative phosphorylation as opposed to the canonical mechanism which is regulated by the ATP/ADP ratio. Though the volumetric component is present in the model at this point, since there is no change in volume for the simulation of electrical stimulation, the component is nullified. In Chapter Four however, we have already validated three out of the four components against electrical stimulation data. We use the full model to reproduce the experimental phenomena observed during FUS stimulation. The model allowed us to decipher the

meaning behind the prominent features of the experimental data. Particularly, the downward spikes produced during the acoustic bursts. As mentioned previously, we thought these were artifacts, but the model revealed that these were transient episodes of reduced extracellular ionic concentration due to ionic redistribution resulting from volumetric changes in response to acoustic radiation force. The model also verified that the disparity in experimental responses between FUS and electrical stimulation was physiological. FUS stimulation is a more energetically economical mechanism, therefore extrudes more potassium for less oxygen consumption as compared to electrical stimulation.

The limitations of the model are mainly due to the fact that it is a simplified model for all components. It does not account for countless other factors that would increase the quantitative accuracy of the simulations such as a model of lactate production by astrocytes and lactate consumption by neurons. Nonetheless, it produces excellent qualitative simulations as compared to experimental data, and reasonably comparable quantitative results as well.

The model can be used in future applications to predict protocol ranges that will lead to varying levels of tissue excitability or perhaps even quiescence. Another possibility is to run the electrical experiments discussed in Chapter Two for a longer period of time to see if the second steady state of response persists indefinitely or if the system changes again or breaks down. The model can also be used to determine stimulation parameters that will result in physiologically relevant levels of potassium extrusion, which can then be applied to other experimental platforms.

Conclusion

This dissertation is a cohesive investigation into the metabolic demands on neuronal responses to focused ultrasound stimulation. It presents novel electrophysiological experiments of metabolic activity, which is supported by a computational model. The experimental results and corresponding simulations reveal different metabolic demands in neuronal tissue between FUS and conventional electrical stimulation. They also suggest that acoustic radiation force is a predominant mechanism in FUS stimulation. Finally, experiments show that neuronal tissue is transiently altered to a more excitable state by FUS modulation, as is predicted by the model.

APPENDIX

This section contains a protocol paper I published as a first author during a collaboration in the laboratory of Dr. Nathalia Peixoto. It uses representative data from a paper by Hamilton *et al.*, 2015 to visually demonstrate protocols and techniques used to prepare primary neuronal cultures on microelectrode arrays which are subsequently trained through electrical stimulation and processed as described below. Because the topic is not part of my thesis study, it has been included in the appendix.

TIME-DEPENDENT INCREASE IN THE NETWORK RESPONSE TO THE STIMULATION OF NEURONAL CELL CULTURES ON MICRO-ELECTRODE ARRAYS

Abstract

Micro-electrode arrays (MEAs) can be used to investigate drug toxicity, design paradigms for next-generation personalized medicine, and study network dynamics in neuronal cultures. In contrast with more traditional methods, such as patch-clamping, which can only record activity from a single cell, MEAs can record simultaneously from multiple sites in a network, without requiring the arduous task of placing each electrode individually. Moreover, numerous control and stimulation configurations can be easily applied within the same experimental setup, allowing for a broad range of dynamics to be explored. One of the key dynamics of interest in these in vitro studies has been the extent to which cultured networks display properties indicative of learning. Mouse neuronal cells cultured on MEAs display an increase in response following training induced by electrical stimulation. This protocol demonstrates how to culture neuronal cells on MEAs; successfully record from over 95% of the plated dishes; establish a protocol to train the networks to respond to patterns of stimulation; and sort, plot, and interpret the results from such experiments. The use of a proprietary system for stimulating and recording neuronal cultures is demonstrated. Software packages are also used to sort neuronal units. A custom-designed graphical user interface is used to visualize post-stimulus time histograms, inter-burst intervals, and burst duration, as well as to compare

the cellular response to stimulation before and after a training protocol. Finally, representative results and future directions of this research effort are discussed.

Introduction

Micro-electrode arrays (MEAs) can be used to investigate drug toxicity, design paradigms for next-generation personalized medicine, and study network dynamics in neuronal cultures. In contrast to more traditional methods-such as patch-clamping, which can only record activity from a single cell, or field recording with a glass pipette, which can record extracellular responses from the neurons surrounding the electrode at a single site-MEAs can simultaneously record from multiple sites in a cell culture without requiring the arduous task of placing each electrode individually. This allows for the study of the dynamic interactions between groups of cells that form a network within that culture. Moreover, the effects of electrical stimulation on network firing patterns and network control in neuronal cultures have been well documented, and numerous configurations of electrical stimulation and controls can be easily applied within the same experimental setup, allowing for a broad range of spatio-temporal dynamics to be explored.

One of the key dynamics of interest in these in vitro studies has been the extent to which cultured networks display properties indicative of learning. The Peixoto Lab previously examined the effects of high-frequency training signals, as described in (Ruaro, Bonifazi, & Torre, 2005), on networks of mouse neurons plated on microelectrode arrays. In these experiments, networks displayed an increase in response following training induced by electrical stimulation. The increased response was

considered a form of learning via stimulus recognition, whereby the networks responded in a consistent manner to a change in stimulus after the application of a specific stimulation (i.e., training) protocol.

This protocol demonstrates how to culture neuronal cells on MEAs, successfully record from over 95% of the plated dishes, establish a protocol to train the networks to respond to patterns of stimulation, sort single-unit activity, plot histograms, and interpret the results from such experiments. The use of a proprietary system for the stimulation and recording of neuronal cultures is demonstrated, as well as the application of software packages to sort neuronal units. A custom-designed graphical user interface is used to visualize post-stimulus time histograms, inter-burst intervals, and burst duration, as well as to compare the cellular response to stimulation before and after a training protocol.

Protocol

All animal procedures follow the National Institutes of Health (NIH) guidelines and/or the Public Health Services Policy on the Humane Care and Use of Laboratory Animals and are under an institutionally approved animal care and use (IACUC) protocol at George Mason University.

Material Preparation

1. Autoclave the following materials: 5.75 inch long glass pipettes arranged vertically in (2) 500 mL beakers, approximately 24 pieces of filter paper (150 mm diameter, each one cut into 8 wedges; the pore size does not matter), 1,000 µL filtered pipette tips, 200 µL filtered pipette tips, 10 µL filtered pipette tips, and de-ionized (DI) water for the washes (at least 200 mL).

2. **Prepare the reagents and media.**
    1. Prepare all reagents and media in the biohood using aseptic techniques.
    2. Prepare Poly-D-lysine (PDL) as per Table 3.
        1. Mix the PDL with sterile DI water to a final concentration of 50 µg/mL, as follows. Use a sterile serological pipette to transfer 96 mL of sterile DI water to an autoclaved glass reagent bottle.
        2. Use a sterile serological pipette to add 4 mL of sterile DI water to the manufacturer vial containing PDL. Dissolve the PDL by pipetting. Use the same pipette to transfer the PDL solution to the glass reagent bottle containing the 96 mL of sterile DI water.
        3. Cap the bottle tightly before removing it from the biohood and vortex the solution. In the biohood, divide the solution into 5-mL aliquots; freeze any unused solution at -20 °C. Thawed PDL can be re-frozen once. Discard thawed solution if re-frozen before.
    3. Prepare laminin solution as per Table 4.
        1. Mix the laminin with phosphate buffer saline (PBS) to a final concentration of 20 µg/mL, as follows. Use a sterile serological pipette to transfer 49 mL of PBS to a 50 mL centrifuge tube.
        2. Use a sterile serological pipette to add 1 mL of PBS to the manufacturer vial containing the appropriate weight of laminin. Dissolve the laminin by pipetting. Use the same pipette to transfer the

laminin solution to the 50 mL centrifuge tube containing the 49 mL of PBS.

3. Cap the tube tightly before removing it from the biohood and vortex the solution. In the biohood, divide the solution into 5 mL aliquots; freeze any unused solution at -20 °C. Thawed laminin cannot be re-frozen; discard any unused thawed solution.

4. Prepare storage medium, as per Table 5.

   NOTE: Storage medium is used to store tissue for up to a month at ambient CO_2 levels. It can be purchased (see the table of materials), or it can be prepared using the general recipe of: ambient CO_2 cell storage medium + 2% serum-free supplement for neural cell culture + 0.5 mM cell culture medium that contains a stabilized form of L-glutamine (see the table of materials).

   1. To make 10 mL of storage medium, transfer 10 mL of storage medium for embryonic tissue without $CaCl_2$ to a 15-mL centrifuge tube. Add 210 µL of serum-free supplement for neural cell culture and 55 µL of a stabilized form of L-glutamine. Mix gently by inversion.
   2. As the storage medium is light-sensitive, protect it by covering the 15-mL centrifuge tubes with aluminum foil. Aliquot 2 mL of storage medium per tube for a total of 5 aliquots. Store in a refrigerator for up to 2 weeks or until ready for use, but do not freeze.

5. Prepare DMEM 5/5 medium, as per Table 6.

1. Thaw aliquots of serum-free supplement for neural cell culture, horse serum (HS), fetal bovine serum (FBS), and ascorbic acid. Thaw an aliquot of pen-strep, if necessary, to control bacterial contamination. Pipette each ingredient into a 50 mL centrifuge tube. Make sure that the pipette tips do not touch any surfaces or objects.
2. Inside the biohood, connect the filter to the vacuum tube with the vacuum still off. Pour the mixture into the filter top and close it. Turn on the vacuum in the biohood and let the medium filter to the bottom of the container. Unplug the filter from the vacuum before turning off the vacuum.
3. Tighten the lid on the sterile medium container, label it, and store any unused medium at 4 °C for up to one month. Open the container inside the biohood to keep the medium sterile.

6. Prepare DMEM+ medium, as per Table 7.
    1. Thaw aliquots of serum-free supplement for neural cell culture and ascorbic acid (and pen-strep, if needed). Pipette each ingredient into a 50 mL centrifuge tube. Repeat steps 1.2.5.2-1.2.5.3 for the remaining process.

Array/Dish Preparation

NOTE: The MEAs used in the procedure are 60-channel arrays organized in an 8 x 8 square. The interelectrode distance is 200 µm, and each electrode is 10 µm in diameter. The conducting material for the tracks is titanium, and the electrodes

themselves are made of TiN. The glass ring around the electrodes is 6 mm high, with a 24 mm outer diameter. A cap made from polyoxymethylene (POM) is used to cover the MEA, and a gas-permeable/liquid-impermeable fluorinated ethylene propylene (FEP) film is used to prevent contamination during recording and stimulation sessions.

1. The day before plating.
    1. Make unused MEAs hydrophilic by exposing them to plasma; this is usually not necessary after the first use. Ensure that glass coverslips used for control cultures also receive a plasma treatment. NOTE: Plastic Petri dishes (35 mm) may also be used as control dishes and do not need any pre-treatment.
        1. Administer the plasma treatment using a plasma etcher for 40-60 s at half power (50 W), with the chamber pressure set to 100-150 mT.
    2. Immediately fill the MEAs with DI water. Submerge the coverslips in a Petri dish filled with DI water. Leave the DI water in contact with treated surfaces for approximately 15 min.
    3. Inside the biohood, suction out the DI water. Fill the MEAs to the rim with 70% ethanol. Remove the DI water from the Petri dish containing the coverslips and fill the Petri dish with ethanol until the coverslips are fully submerged. Allow this to sit for 10-15 min.
    4. Label all Petri dishes and control dishes with the MEA ID#, date of surgery, cell type, and initials. Then, place each MEA in its labeled Petri dish.
    5. Place the MEAs into individual Petri dishes and remove the ethanol using vacuum suction. Fill the MEAs with sterile DI water to remove any residual

ethanol. Use vacuum suction to remove the DI water. Let the MEAs air-dry inside the biohood.

6. Add 40-70 µL of 50 µg/mL poly-D-lysine (PDL; high molecular weight, at least 50 kDa) to the center of each MEA and 0.2 mL to controls using sterile pipette tips.
7. NOTE: Be sure not to touch the center of the MEA with the pipette, tip as this may damage the electrodes. The exact amount of PDL dispensed depends on the hydrophilicity of the surface.
8. Place a small piece of lab tissue paper into each dish and wet it with sterile water to avoid PDL evaporation overnight. Cover all dishes before removing them from the biohood. Place the dishes in an incubator at 37 °C overnight.

2. Plating day.
    1. On the plating day, thaw 1 aliquot of laminin (20 µg/mL); each MEA requires 40-50 µL of laminin, and each control dish requires 0.2 mL of laminin. Calculate the volume of laminin needed based on the number of MEAs and controls to be used.
    2. Transfer all dishes from the incubator to the biohood.
    3. Fill all MEAs with sterile DI water using a sterile serological pipette and allow them to sit for 10 - 15 min. Aspirate the DI water using sterile Pasteur pipettes and repeat the process twice.
    4. Add 40 - 50 µL of thawed laminin to the center of each MEA and 0.2 mL of laminin to the control plates using sterile pipette tips. Cover all the MEAs and

the control dishes in the biohood and transfer them to an incubator at 37 °C for 1 h.

    1. Carefully remove the excess laminin from the center of the MEAs using suction with sterile Pasteur pipettes and let the surface air-dry before plating.

5. Leave the dishes in the biohood or place them in an incubator until ready to plate the cells. NOTE: The dishes can stay in the incubator until the following day. However, if more time is needed, it is advisable to clean the dishes and start over from the poly-D-lysine (PDL) step (step 2.1.6).

Embryo Removal and Brain Extraction

1. Pour L-15 (Leibovitz) medium into 4 of the 100 mm Petri dishes. Cover them and place them in a -20 °C freezer until the medium has a slushy consistency but is not frozen solid (~40-60 min).
2. Do this approximately 40 min to 1 h before dissection. NOTE: This will cool the embryos and the brains quickly, so that they have a firm consistency and do not disintegrate upon extraction.
3. Prepare the dissection area for embryo removal.
    1. Place a tray with ice near a sink and lay out the surgical instruments and materials for embryo removal. These include 4 Petri dishes with cold L-15 "slush," paper towels, a spray bottle with 70% ethanol, blunt-nose thumb forceps, fine forceps, small surgical scissors, and large scissors (Figure 35).
4. Prepare the dissection area for brain extraction.

1. Place a glass Petri dish face down in a tray full of ice.
2. Lay out the surgical instruments and materials for brain extraction, including paper towels, small surgical scissors, a thin double-ended spatula, a spray bottle filled with 70% ethanol, and a plastic bag for the disposal of the carcass (Figure 36).

5. Put on a lab coat, a facemask, and gloves. Spray all working surfaces, including the gloves, with 70% ethanol. NOTE: Though this is not a sterile procedure, it is best to reduce the chances of contamination as much as possible.
6. Euthanize an E17 timed-pregnant mouse following the NIH guidelines16 and/or Public Health Services Policy on the Humane Care and Use of Laboratory Animals and under an institutionally approved animal care and use protocol (IACUC) for CO_2 asphyxiation. Be sure to release the CO_2 gas slowly into the chamber over a 3 to 5 min period to avoid inducing panic or discomfort in the mouse.
7. Decapitate the mouse and place it on a paper towel, ventral side up. Spray its lower abdomen with 70% ethanol. Using the small surgical scissors, make a V-shaped cut through the skin and subcutaneous fat of the lower abdomen, extending the cut to the distal ends of the thoracic cavity and exposing the uterus.
8. Using forceps, carefully lift the uterus between the embryos. Cut away the connective tissue with dissection scissors until the entire uterus is free. Briefly rinse the uterus with 70% ethanol to remove any blood and place it in one of the 4 Petri dishes filled with cold L-15.

9. Release each embryo from the uterus and interior embryonic sac using a pair of fine-tipped forceps. Ensure that the umbilical cord has been severed and the placental sac removed. Place the freed embryos in the second dish full of cold L-15. Decapitate the embryos with forceps and scissors. Using forceps, transfer the heads to a third Petri dish and the bodies to a fourth, both full of cold L-15.

Frontal Cortex Removal

1. In a biohood, place a wedge of autoclaved filter paper on the chilled glass Petri dish stage. Place a single embryo head on the filter paper. Grip the skull by placing a pair of forceps through the ocular cavities with the non-dominant hand. Remove the skin and underlying muscle tissue with a pair of iris scissors.
2. Place the cutting edge of the lower sheer of the iris scissors into the base of the skull. Keeping the lower sheer against the inner surface of the skull, away from the brain, cut through the occipital plate and then along the midline between the parietal plates. Continue cutting rostrally, between the cartilaginous frontal skull plates.
3. Starting at the center of the occipital plate, make a perpendicular cut to the left and to the right of the center cut.
4. Remove the brain by carefully sliding a small spatula between the ventral surface of the brain and the bottom skull plates until it is completely under the brain. Lift the spatula up; the whole brain will come out intact.
5. Place a few drops of L-15 medium on the filter paper so that the brain does not stick to the paper and gently slide the brain from the spatula onto the filter paper,

ventral side down. Carefully cut away the olfactory bulb with the tip of the spatula.

6. Using a clean spatula, dissect the frontal lobe in a trapezoidal pattern. Transfer the tissue to a 15 mL centrifuge tube containing storage medium. Repeat the above with the remaining embryos. Be sure to use a fresh wedge of filter paper each time (*i.e.*, one wedge of filter paper per head).

Cell Dissociation

1. In the biohood, assemble the items listed in Table 8.
2. Use a sterile serological pipette to add 5 mL of DMEM+ to a vial of papain; warmed DMEM+ can be used to better dissolve the papain. Gently pipette to mix the solution.
3. Use a sterile micropipette to add 0.5 mL of DMEM+ to a vial of DNase. Avoid forceful pipetting while making the DNase solution, because DNase is sensitive to shear denaturation.
4. Transfer 2.5 mL of papain solution to a sterile centrifuge tube and add 125 µL of the DNase to the same tube. Mix the solution by gently inverting the capped centrifuge tube about 8 times.
5. Using a sterile, wide-bore pipette, remove the tissue from the tube containing storage medium and place it into a sterile, 35-mm Petri dish. Collect as little medium as possible. Use a sterile pipette to remove as much excess storage medium as possible without removing the tissue. The tissue should not be floating in medium, but it should be moist.

6. Use two sterile scalpel blades to mince the tissue. Use a sterile serological pipette to add 2.5 mL of the DNase/papain mixture to the minced tissue in the Petri dish. Gently swirl the Petri dish to ensure that all tissue is free in the solution and not adhered to the bottom of the dish. Place the dish in an incubator 37 °C for 15 min.
7. In the biohood, use a sterile, wide-bore transfer pipette to transfer all media and tissue to a sterile, 5 mL cryogenic tube. Place the tip of the same wide-bore transfer pipette close to the bottom of the tube. Gently triturate by slowly pipetting up and down 10-15 times.
8. Avoid forming bubbles while pipetting. Repeat the process using a small-bore transfer pipette until a homogenous mixture is achieved. If the tissue is not dissociated, triturate using a 1,000 µL pipette.
9. Add 2 mL of warmed DMEM 5/5 to the dissociated cell mixture. Cap the centrifuge tube while it is still in the biohood. Gently mix by inversion. Centrifuge at approximately 573 x g for 5 min at room temperature (20-25 °C).
10. In the biohood, use a sterile serological pipette to remove and discard all the supernatant, without breaking the pellet. Use a sterile pipette to add 1 mL of warmed DMEM 5/5 to the pellet in the tube to re-suspend the cells. Use a sterile, small-bore transfer pipette to break up the pellet by gently pipetting up and down until the mixture is homogenous.

    NOTE: Avoid forming bubbles while pipetting. If very little tissue was collected, add only 0.5 mL of DMEM 5/5.

11. Inside the biohood, use a sterile pipette to transfer 10 µL of the cell suspension to a microcentrifuge tube. Outside of the biohood, add 10 µL of Trypan blue to the 10 µL of cell suspension in the microcentrifuge tube.

    NOTE: This step does not require sterility.

12. Load 10 µL of the Trypan blue cell suspension into a disposable hemocytometer chip in order to count the cells.

Plating Cells

1. In the biohood, use a sterile micropipette to transfer 50 µL of cell suspension to the center of each array and each control Petri dish. Use one pipette tip per dish. Make sure to put the cells exactly at the center of the array. Re-wet the lab tissue paper that was in the dish with sterile water, or place new tissue paper into each dish. Cover the dishes.
2. Place the covered Petri dishes in an incubator set to 37 °C and 10% CO_2 for 3-4 h.
3. In the biohood, gently add 1 mL of warmed DMEM 5/5 to each MEA.

    NOTE: Avoid washing the cells away from the center array when adding the medium (important!). Very carefully, use a sterile micropipette to add one drop at a time around the inside edges.

4. Place a cap containing a gas-permeable FEP membrane on each MEA. Return them to the incubator for two days.

    NOTE: The cap prevents contamination and evaporation. Follow aseptic technique, drying the caps in the biohood with 100% ethanol before putting them

on the MEA. The cultures must be capped within the biohood and must remain capped at all times.

Maintaining the Cultures

1. **After two days, perform a complete medium replacement with warmed DMEM+.**
    1. Transfer only a few dishes from the incubator to the biohood at a time to avoid stressing the cultures for too long.
    2. Use a sterile 1-mL micropipette to draw out all the medium from the dish by carefully placing the tip of the pipette on the inside wall of the dish, avoiding touching the cells in the center. Use only one pipette tip per dish to avoid spreading contamination.
    3. Use a sterile micropipette to dispense 1 mL of warm DMEM+, carefully placing the tip of the pipette on the inside wall of the dish.
2. **Perform 50% medium changes with warmed DMEM+, as described above, 2-3 times per week and with no more than 4 days between feedings.**
    1. Use a sterile 1 mL micropipette to draw out 500 µL of medium from the dish. Use a sterile micropipette to dispense 500 µL of warm DMEM+.

Visual Inspections and Recording

1. Inspect the dish samples every other day under a microscope to look for cell coverage over the array (using 4X and 10X magnification) and contamination (using 20X magnification), either bacterial or fungal.

NOTE: Figure 37a shows an example of optimal cell coverage, whereas Figure 37b shows a culture with poor cell density.

2. **Two weeks after plating, test a sample of the MEA dishes for spontaneous activity. Record from MEAs, as described below, for 3-5 min. Spikes will be detected if activity is present (Figure 38).**

   NOTE: It is up to the experimenter to determine when to begin testing based on the type of experiment and hypothesis being investigated.

   1. To record activity in an MEA, use the following equipment: power supply, amplifier, headstage/preamplifier, temperature controller, and stimulation generator (see the table of materials and Figure 39).
   2. Before taking the cultures out of the incubator, plug in the temperature controller and turn on the system by switching on the power supply (according to the manufacturer's instructions), allowing the heated base plate of the preamplifier to reach 35 °C.
   3. Place the capped culture in the preamplifier so that the black line in the MEA well aligns with the reference ground. Ensure that the preamplifier pins line up, that the top of the preamplifier is secured, and that the culture cap is still on.
   4. Once the culture is placed in the plate, uncheck the "Change MEA" option on the data acquisition software (see the table of materials for software names and user guides). Additionally, uncheck the box labelled "Blanking" before doing any recordings.

5. Select "Download" in "MEA_Select" after the culture is placed in the system. Check that the program shows "Download OK" before continuing.
6. Press "Start" in the software environment to start visualizing the signals. In the main window, select: "Spikes" → "Detection" → "Automatic," change the "Std Dev" value to "5," and click "refresh" to reset the threshold.

   NOTE: The "Spikes" window shows spikes that passed threshold.
7. In the main window, select "Recorder" → "Recorder" → "Browse." Change the path and file name to identify the date, time, dish, and experiment. Set the time limit (*e.g.,* to 5 min). Click "Stop," "Record," and "Play." Note that the recording stops automatically.
8. Open the stimulation software. Select "Recorder" → "Recorder" → "Browse" to create a file and to set the time limit. Click "Stop," "Record," and "Play" to record again. Click "Download and Start" (on the stimulation software) for the stimulation to be delivered to the dish.
9. Select the "Change MEA" button in the software control in order to change dishes.

   NOTE: Do not keep the culture out of the incubator for more than 30 min at a time without a system to maintain a CO_2 atmosphere around the culture. If longer recording sessions are required, use a commercially available adapter to supply CO_2.

Training Networks

NOTE: Figure 40 shows an overview of steps 9.1-9.3, described below.

1. Record a 5-min baseline of spontaneous activity from the cell culture (as described in step 8). Once the baseline has been established, administer a 5-min pre-training probing stimulation consisting of a 0.5 Hz biphasic pulse with a 200 µs pulse duration and a 900-mV pulse amplitude (Figure 41a) through the selected stimulation electrodes, as shown in Figure 42 (see the software manual in the table of materials for details on how to select the stimulation electrodes).
2. Upon completing the pre-training stimulation, administer a "training" protocol to the networks using the same electrodes as in the probing stimulation. Deliver the high-frequency trains once every 2 s, as described in (Hamilton et al., 2015). (Figure 41b and Figure 41c).

   NOTE: The training signal consists of 40 pulse trains. Each pulse train is comprised of 100 biphasic pulses, with 4 ms between pulses, a 200 µs pulse duration, and a 900 mV pulse amplitude.
3. After concluding the training period, administer a 5 min post-training stimulation to the cells, identical to the pre-training stimulation. Once the post-training stimulation ends, record 5 min of post-stimulation spontaneous activity from the network (as described in step 8).
4. Use a separate control group of MEAs to account for possible changes in network response due to natural fluctuations or system non-stationarity. Administer the same experimental protocol described above to those control groups, with the

exception that the control groups receive a sham training period in which no actual training signal is administered.

Data Analysis

Note: The data files are saved and later sorted into neuronal units using a proprietary sorting software (see the table of materials). A customized graphical user interface (GUI) is used to load the units and analyze patterns of activity in the cultures, inter-burst intervals, burst duration, and post-stimulus time histogram (PSTH) (see the table of materials). The PSTH is the most important graph to be analyzed, as it displays the activity of the network in bin sizes (of variable length), thus providing a visual representation of the response of the network to the stimulation presented.

1. Convert the .mcd data files to .plx format using a proprietary sorting software. Export the .plx file to a new .plx file within the same program. Sort the channels into neuronal units (Figure 43). Once the sorting is completed, export the data as a .nex file.
2. Open the .nex file in the appropriate software and save it as a .mat file to be analyzed with the custom-made GUI, which is freely available.

   NOTE: The graphical user interface (see the table of materials) plots PSTHs according to user input (*i.e.*, population PSTH, biased-average PSTH, or individual channel PSTH), allowing for an overview of the stimulation experiment and immediate comparison between the post- and pre-stimulus files. It also plots the initial versus final PSTHs, which compares the network response to

the first 6 and the last 6 stimuli. The GUI performs several other functions, such as spike rate, inter-spike interval, spikes per burst, inter-burst interval, and burst duration, for both stimulation files and files with spontaneous activity.

3. **First, select a .mat file with variables containing spike trains and one variable containing the stimulation artifact; the script will analyze the data, and the main GUI will pop up with a PSTH average graph on the right (Figure 44).**
    1. Click on the active electrode buttons to see the individual PSTH (in blue) in comparison to the average PSTH (in red).

       NOTE: The active electrodes will be colored to show a heat map, where higher values (more red) represent greater peak PSTH values, indicating a stronger response to stimulation.
    2. Select an analysis option using the pop-up menu. Select the "Biased Average" button to select a subset of electrodes and plot the average of that subset; this is useful for comparing sub-network behavior within a culture.

       NOTE: There are multiple different analysis options selected through the pop-up menu, and they are all explained in the "help" button in the software.
    3. Select the "Save Graph" button to save the currently displayed graph as a jpeg file with high resolution. Select the "Data Table" button to export the data into a spreadsheet.

Representative Results

Using the procedure presented here **(**Figure 45**)**, 60-channel MEAs plated with E17 mouse neuronal cells were incubated until the cultures covered the arrays in a healthy carpet of cells (Figure 46 and Figure 37a). After 3 weeks of incubation at 10% CO_2 and 37 °C, the cultures were checked for spontaneous activity using a commercial recording system. The temperature was maintained at 37 °C during the recording procedure using a temperature controller, since temperature affects neuronal activity and firing rates.

Testing for activity

Spontaneously active networks normally exhibit varying signal patterns. An average active culture can register activity in approximately 40% of the electrodes. Of these active electrode sites, nearly half register spontaneous signals, with firing rates ranging from 5 - 10 Hz. A representative raster plot of spontaneous activity is shown in Figure 4a. The tick marks indicate the timestamps of action potentials recorded from 9 active electrodes during a 20 s window, at an acquisition rate of 25 kHz and a bandpass filter range between 300 Hz and 3 kHz. Figure 4b shows the baseline noise and the filtered raw extracellular signal during 8 bursts of activity before the sorting procedure. To separate the action potentials from the noise, thresholds for each channel are set to 5 times the standard deviation of the baseline noise and are calculated over a 500 ms window.

Prior to analysis, recorded spikes for each electrode were sorted offline to distinguish between physiological activity and stimulation artifacts using a k-means

algorithm and principle component analysis. Signals that had been identified as physiological responses were grouped together to create a population response at each electrode (Figure 47 and Figure 43).

Training neural networks with electrical stimulation

Networks were trained using electrical stimulation applied to the culture directly through the MEA electrodes using a stimulus generator (see the table of materials). In this set of representative results, an "L"-shaped configuration consisting of 13 electrodes was used (Figure 8), although many other configurations can be applied. The probing and training stimulation were based on parameters defined in (Ruaro et al., 2005).

A baseline was initially set by recording 5 min of spontaneous activity prior to stimulation. Once the baseline was established, a 5 min pre-training probing stimulation consisting of a 0.5 Hz biphasic pulse with a 200 µs pulse duration and a 900 mV pulse amplitude (Figure 37a) was administered through the selected stimulation sites (*i.e.*, "L"-shaped). A training protocol was then administered to the networks every 2 s using the same set of electrodes. The training signal was comprised of 40 pulse trains, each containing 100 biphasic pulses, with a 4 ms inter-pulse period, a 200 µs pulse duration, and a 900 mV pulse amplitude (Figure 37b and Figure 37c). This training period was then followed by a 5-min post-training phase, similar to the pre-training stimulation. The protocol was then concluded with a 5-min recording of post-stimulation spontaneous activity.

The same experimental protocol was applied to a control group of cultures to account for natural fluctuations in network response. The only difference in the control

protocol, however, was the application of a sham training period, during which no actual training signal was administered.

Statistical analyses of the datasets (*i.e.*, training versus control) were carried out with a one-way ANOVA, with the variable "training" as a between-subject factor. The latency was used as a within-subject factor. If significant interaction was found, Tukey's post-hoc procedure was performed. The results showed a pre-training response within 20 ms post-stimulus, though the range of activity was inconsistent after the first response. However, post-training activity exhibited not only a response within the first 20 ms post-stimulus, as seen during pre-training, but it also exhibited significant activity 30-50 ms post-stimulus (Figure 48 and Figure 49) . There was also a statistically significant correlation of "spike frequency" versus "time after stimulus" and of "spike reliability" versus "time after stimulus." "Spike reliability" can be defined as the probability of seeing a network response to a stimulation, where a response to each stimulus is assigned a maximum value of 1. Figure 50 shows nearly a 50% increase in spike frequency, as well as a 30-50% increase in spike reliability for trained networks versus control in the range of 20-50 ms post-stimulus. These results suggest that the training fundamentally changed the network dynamics.

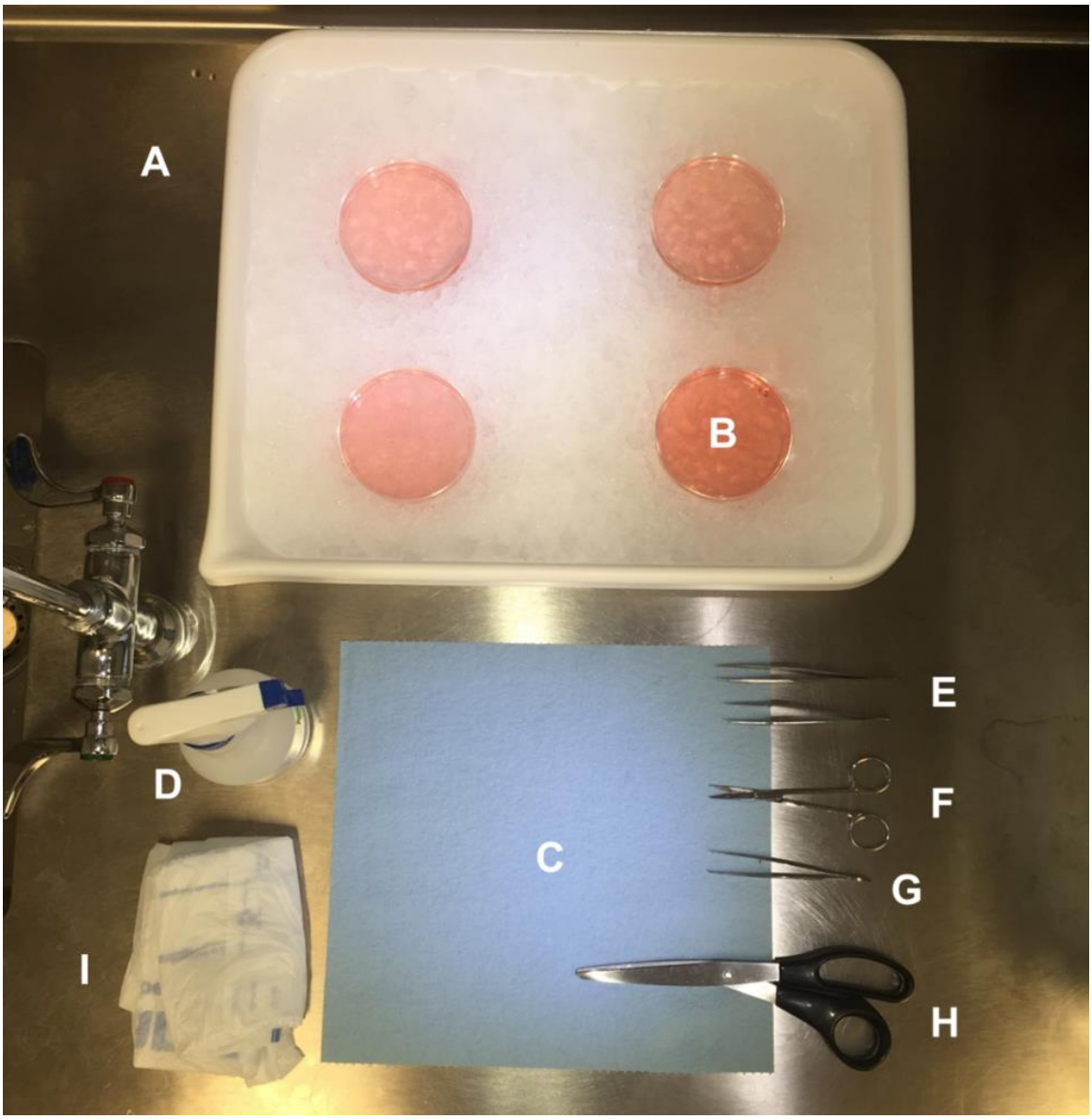

Figure 35: Tools and Materials used for Embryo Removal.
(A) Ice-filled tray. (B) Petri dishes filled with cold L-15 "slush." (C) Paper towel. (D) Spray bottle with 70% ethanol. (E) Fine forceps (x2). (F) Small surgical scissors. (G) Blunt-nose thumb forceps. (H) Large scissors. (I) Body bag.

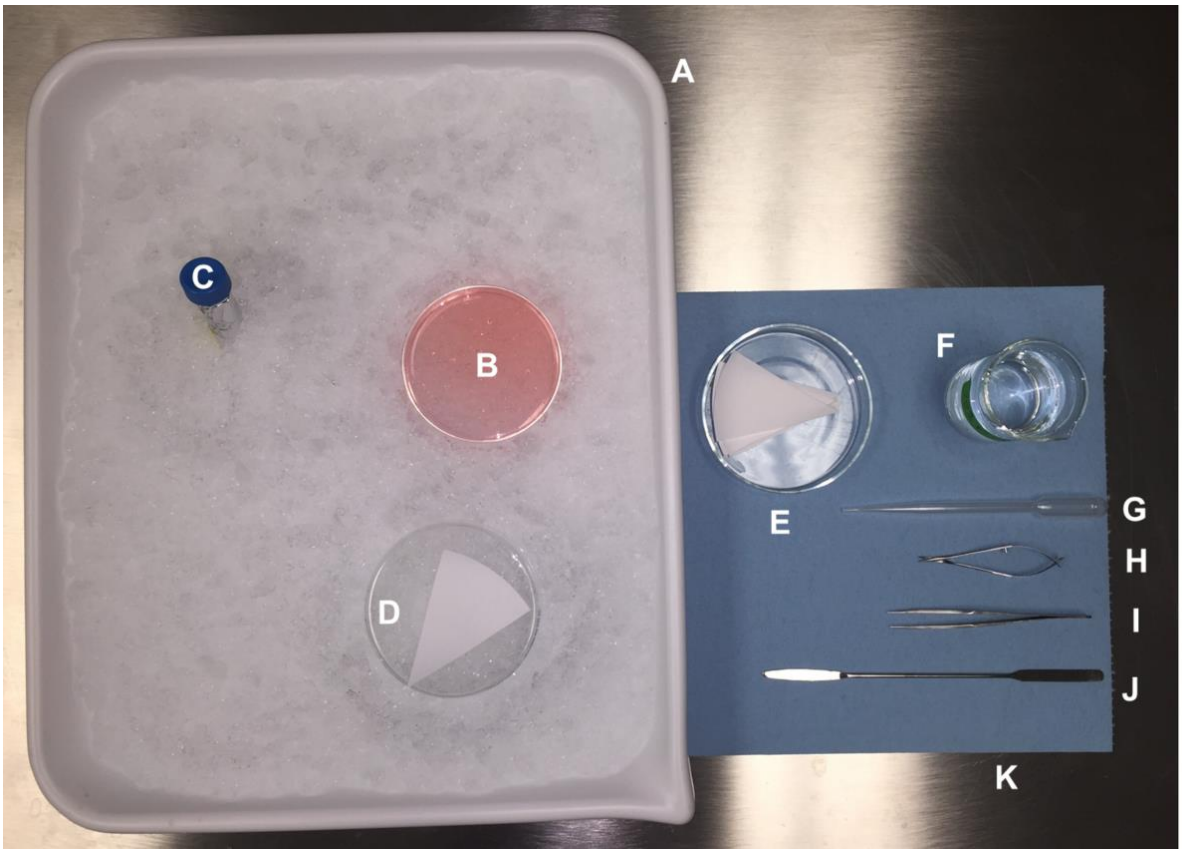

Figure 36: Tools and Materials used for Brain Extraction.
(A) Ice-filled tray. (B) Petri dish containing embryo heads. (C) Foil-covered centrifuge tube with storage medium. (D) Inverted glass Petri dish. (E) Autoclaved filter paper. (F) Beaker with 70% ethanol. (G) Plastic pipette. (H) Iris scissors. (I) Fine forceps. (J) Thin double-ended spatula. (K) Paper towel.

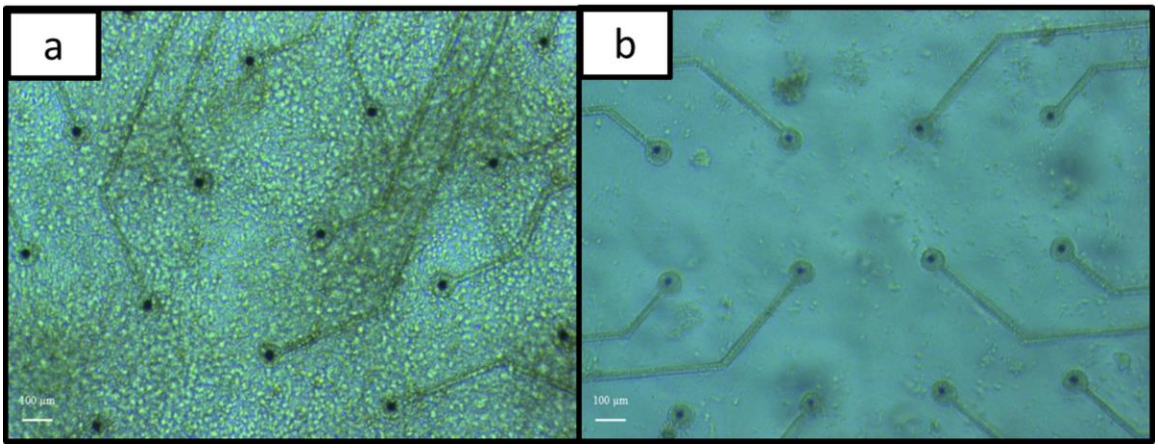

Figure 37: Optimal versus Non-Optimal Cultures.
(A) shows a healthy carpet of cells covering the arrays, in contrast to (B), in which there is poor cell proliferation.

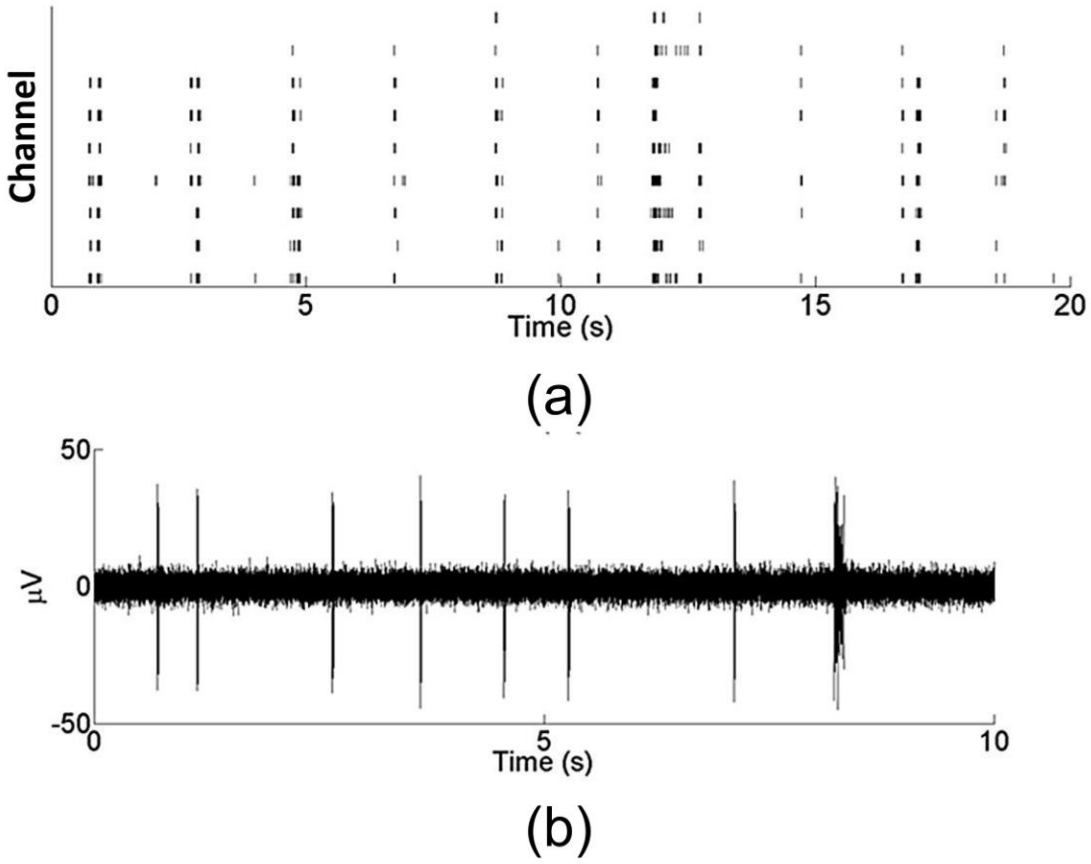

Figure 38: Representative Results of Spontaneous Activity.
(A) Representative raster plot of spontaneous activity. The tick marks indicate action potentials recorded from 9 active electrodes during a 20 s window at an acquisition rate of 25 kHz and a bandpass filter range between 3 kHz and 300 Hz. (B) Representative filtered extracellular action potential from an active site. Figure modified from (Hamilton et al., 2015).

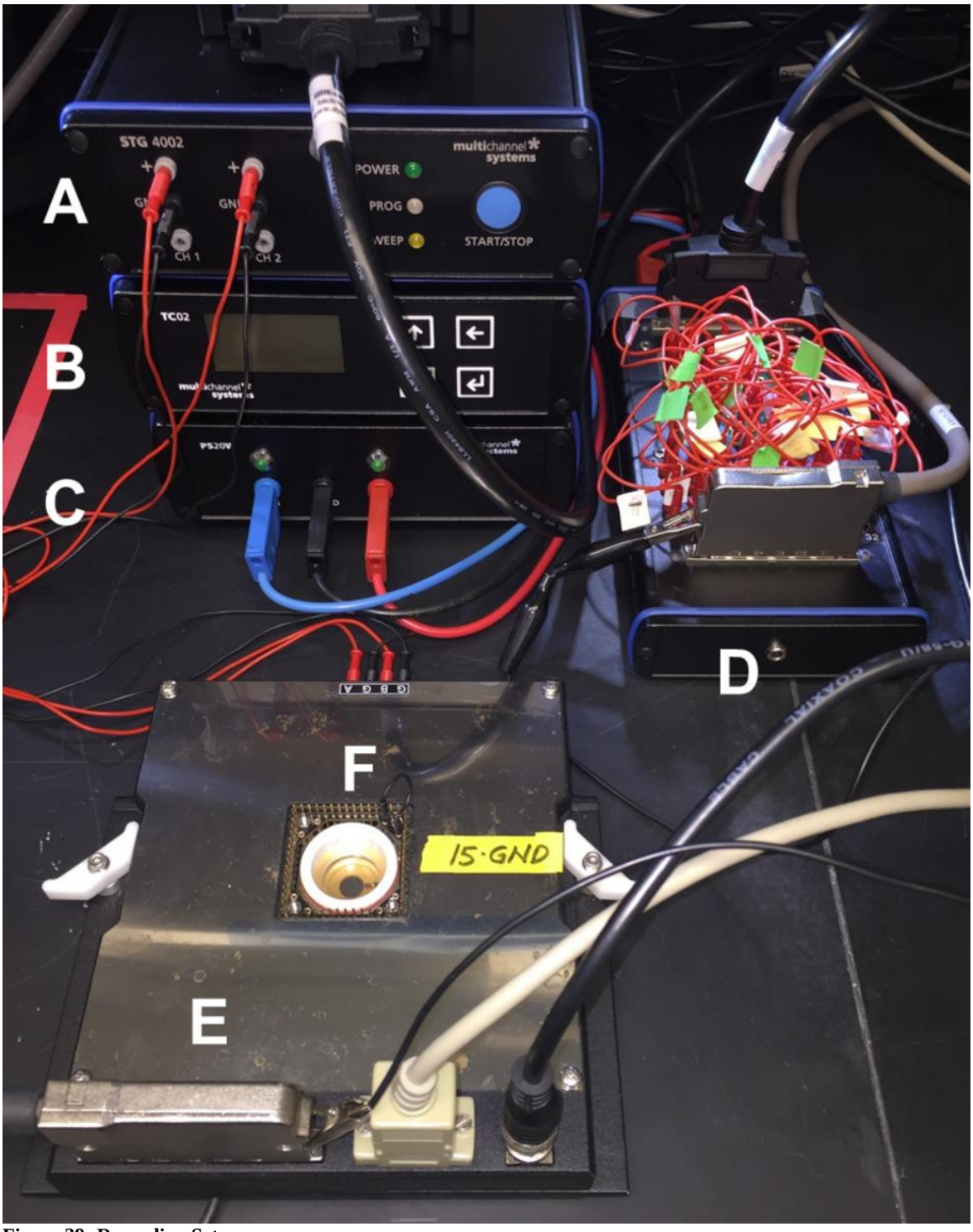

Figure 39: Recording Setup.
(A) Stimulation generator. (B) Temperature controller. (C) Power supply. (D) Amplifier. (E) Headstage/preamplifier. (F) Capped MEA.

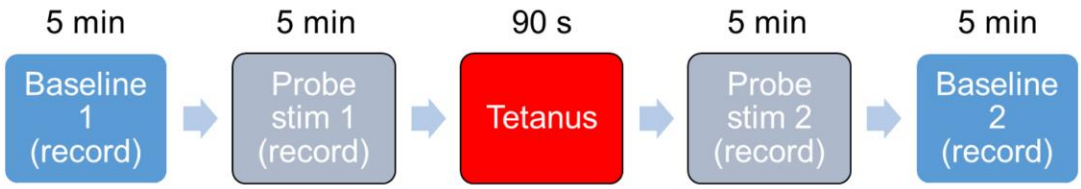

Figure 40: Schematic Representation of the Electrical Training Protocol.
Record an initial baseline for 5 min and a probe stimulation for 3 min. Apply tetanic stimulation for 90 s, which is not recorded. Apply and record a second probe stimulation for 3 min and a final baseline for 5 min.

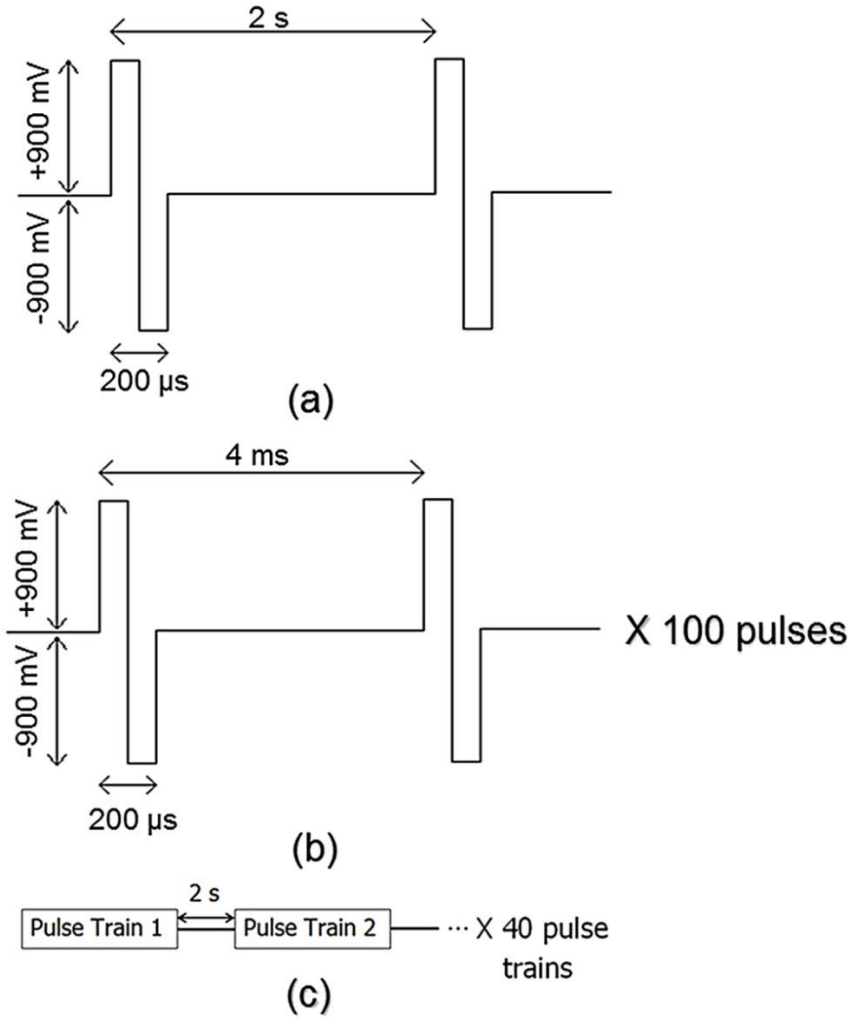

Figure 41: Probing Stimulation and Training Signal Parameters.
(A) Probing stimulation consists of ±900 mV bi-phasic pulses administered at a frequency of 0.5 Hz. (B) Pulse trains consist of 100, ±900 mV bi-phasic pulses at a frequency of 250 Hz. (C) The training signal consists of 40 pulse trains administered every 2 s. Figure modified from (Hamilton et al., 2015).

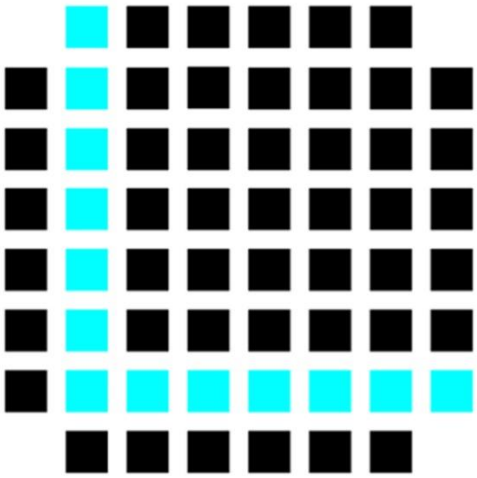

Figure 42: Representation of the "L"-shape Configuration.
Squares represent individual electrodes from an MEA. Blue squares indicate electrodes used for stimulation, whereas all others are used for recording. Figure modified from (Hamilton et al., 2015).

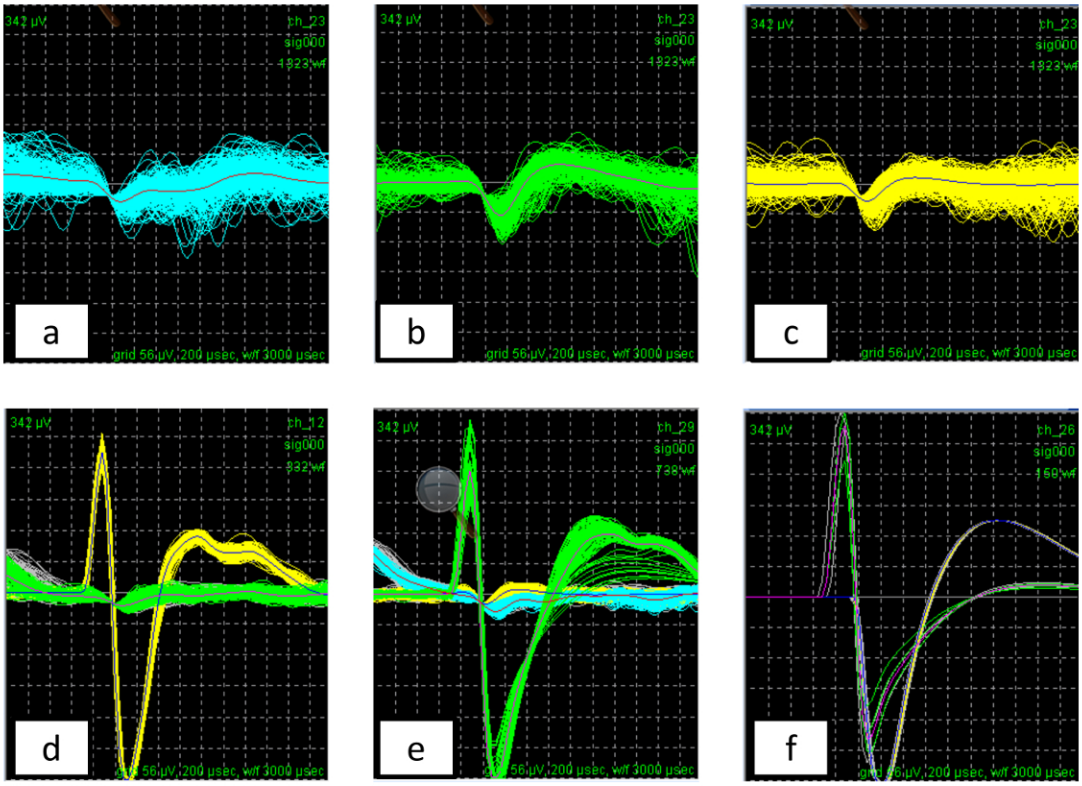

Figure 43: Distinguishing Units from Noise and Stimulation Artifacts.
The several upper panels (A-C) in this figure show examples of noise in order to clarify what a "unit" should be. (D) The yellow waveform is the only unit detected here. (E) The green waveform is the only unit. (F) Example of a channel that was recorded from an electrode that was also used for stimulation, where no units can be reasonably detected due to amplifier saturation.

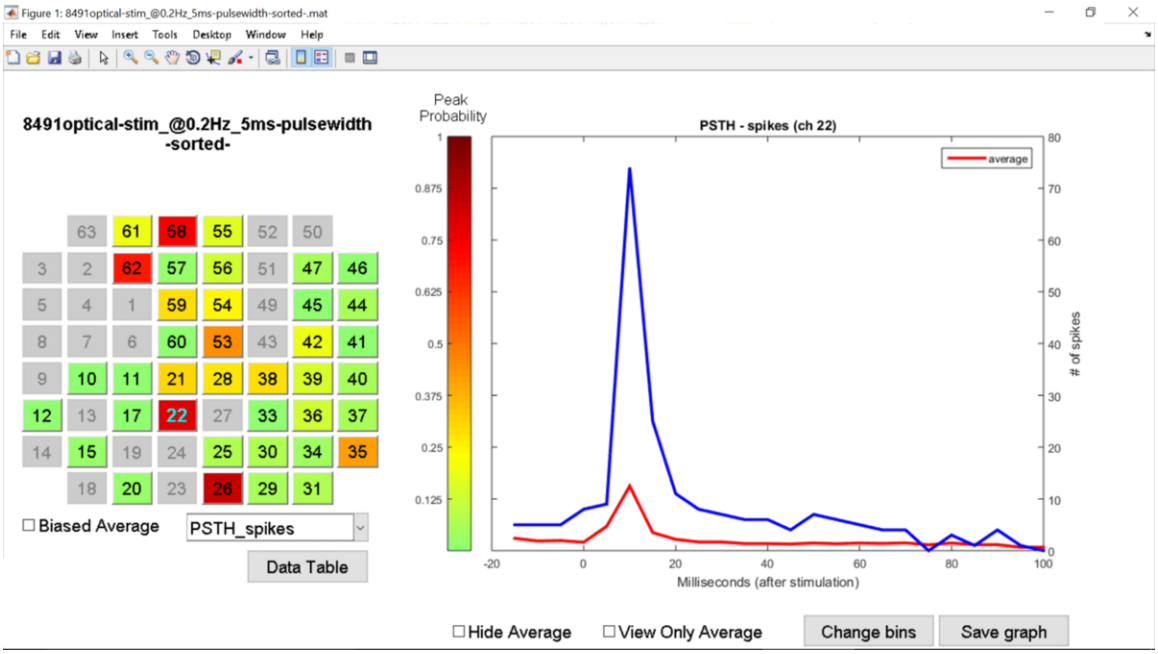

Figure 44: Post-stimulus Time Histogram (PSTH).
A graphical user interface (see Materials Table) plots the PSTHs according to user input (i.e., population PSTH, biased-average PSTH, or individual channel PSTH), allowing for an overview of the stimulation experiment and for immediate comparison between the post- and pre-stimulus files. It also plots the initial versus final PSTHs; this compares the network response to the first 6 and the last 6 stimuli. The GUI performs several other functions, such as spike rate, inter-spike interval, spikes per burst, inter-burst interval, and burst duration, for both stimulation files and files with spontaneous activity.

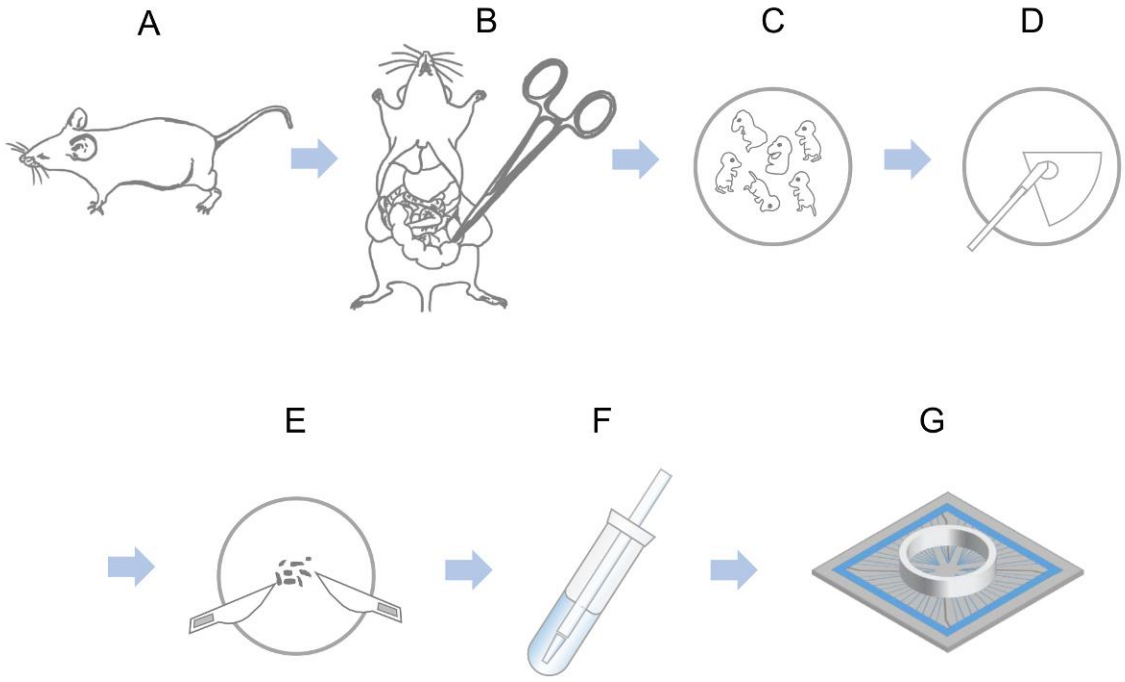

Figure 45: Overview of Cell Preparation and Plating.
(A) An E17 pregnant mouse is euthanized with CO2. (B) The mouse is decapitated and the uterus is removed. (C) The embryos are released and decapitated. (D) The brain is extracted from each embryo and the frontal lobes are removed. (E) The cells are dissociated. (F) The dissociated cells are suspended in medium. (G) The suspended cells are plated on 60-channel multi-electrode arrays (MEAs).

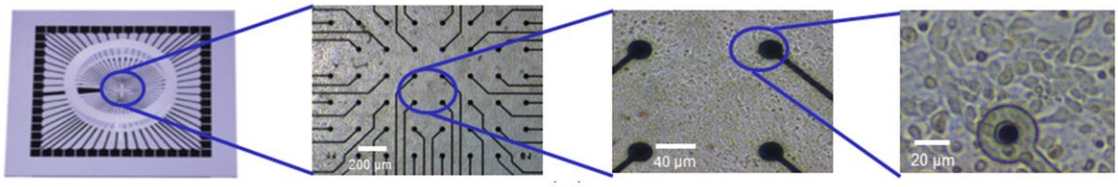

Figure 46: Neuronal Cultures Plated on Microelectrode Arrays.
Embryonic mouse neurons are plated on 60-channel MEAs, which allow for the simultaneous recording of the neuronal activity across the network from each electrode. (Figure modified from (Hamilton et al., 2015)).

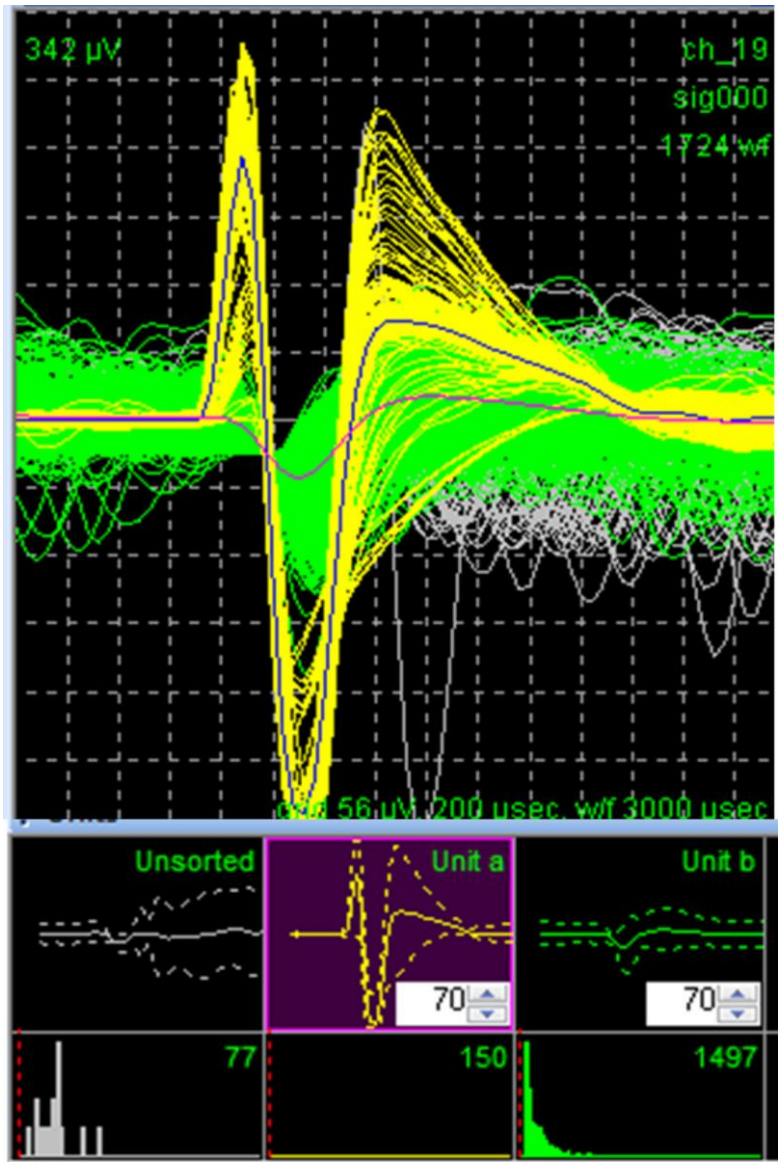

Figure 47: Sorting Program used to Sort the Waveforms from Each Channel.
The sorting program loads a data file and displays all the units initially acquired for each channel. One of several methods is selected to assign signals to specific units. In this example, the k-means clustering algorithm was selected, and the yellow unit (labeled "unit a" on the bottom window) was identified. Another program is then used to export the .nex file into a .mat file, which is the input file for the custom-made GUI (see Figure 44).

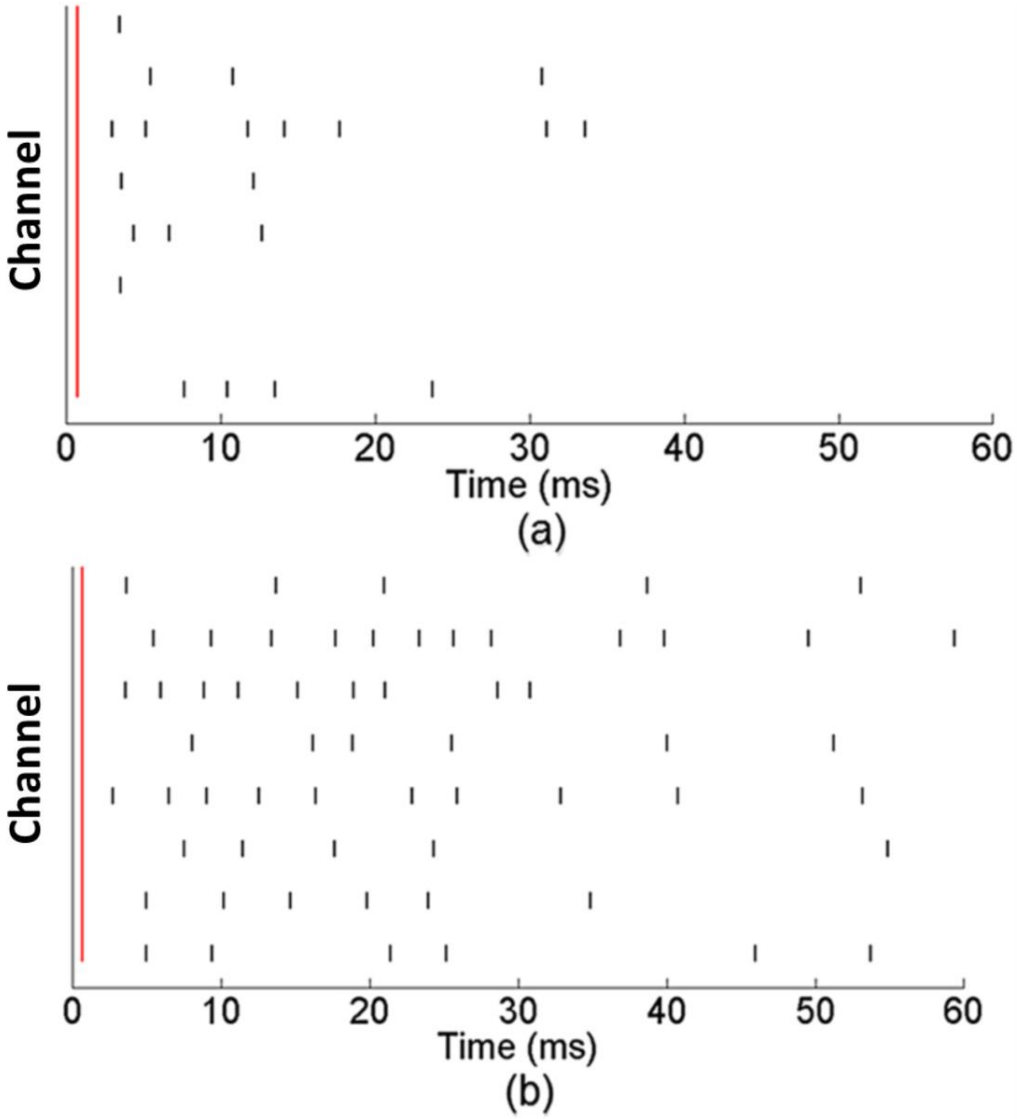

Figure 48: Altered Network Activity in Response to Stimulation after a Training Period.
Representative raster plot of activity from eight electrodes. The vertical red line indicates the time of the stimulus, and the black tick marks indicate action potentials. In pre-training (A), there is an immediate response to the stimulus pulse across channels. In post-training (B), the network exhibits a more prolonged activity response, as well as the immediate response to the (Hamilton et al., 2015).

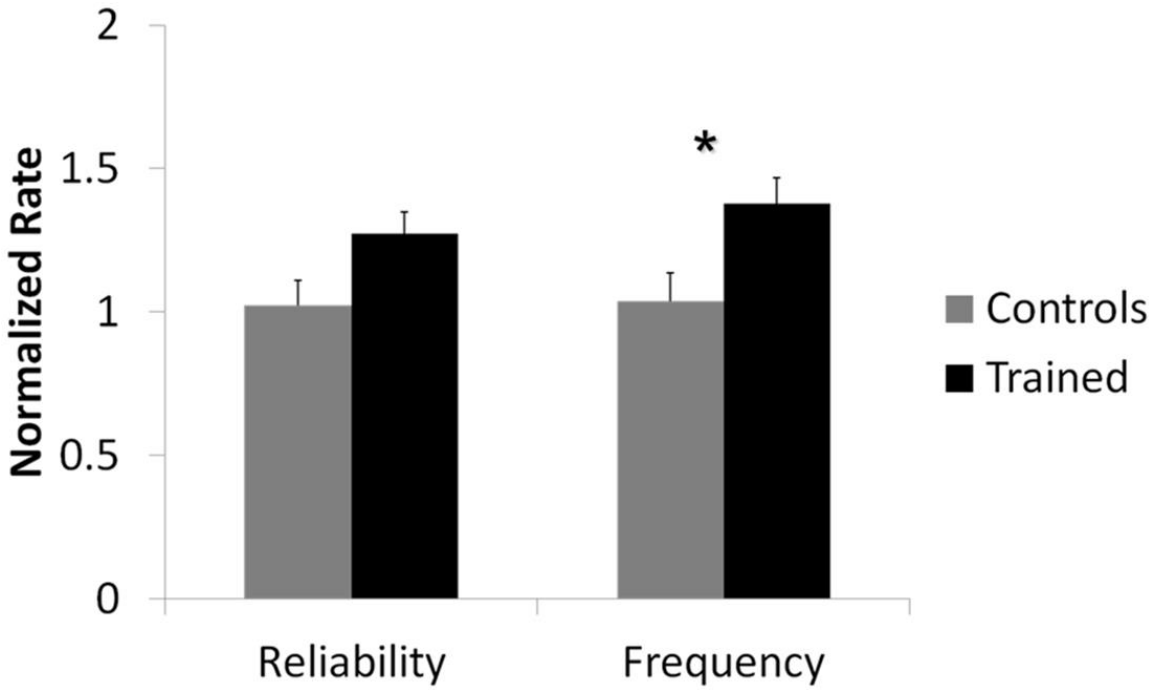

Figure 49: Trained Networks have Significantly Altered Spike Frequencies.
The frequency of the network spiking for the control networks is calculated by integrating the number of spikes over 50 ms immediately after each stimulation and dividing by that period. Shown is the average of 12 trained and 10 control networks (the error bars indicate the standard error of the mean). The asterisk (*) indicates a statistical difference (p-value <0.05) between the two datasets. Figure modified from (Hamilton et al., 2015).

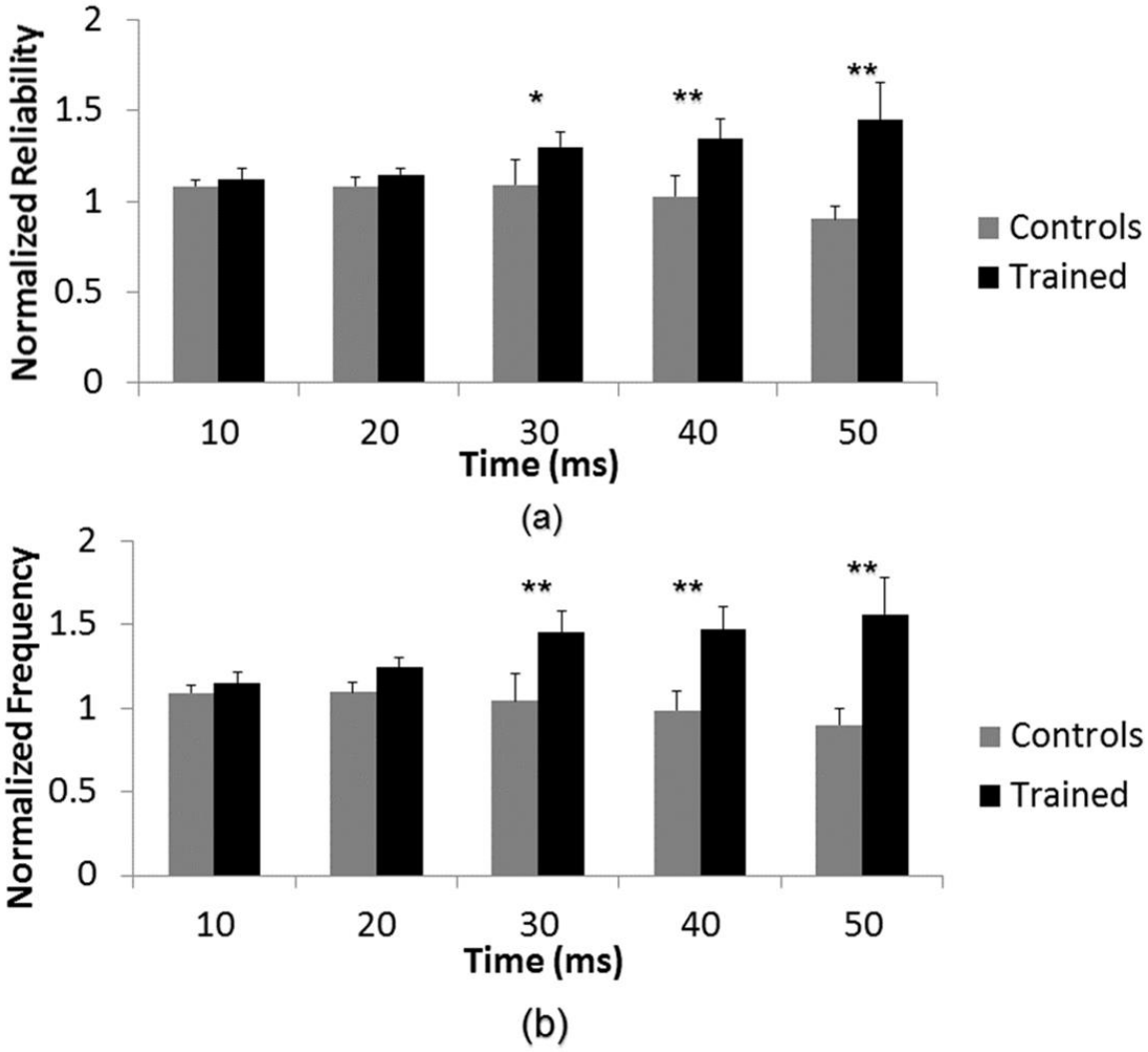

Figure 50: Synaptically-mediated Responses are Significantly Modified in Trained Networks.
(A) The spike reliability, measured in 10 ms bins and normalized to the control networks, shows no change for the direct activation of neurons near electrodes (0-20 ms). There is therefore no statistical difference between controls and trained networks for those bins. On the other hand, the longer-latency responses (30-50 ms), are synaptically mediated, indicating that this method provides a more detailed investigation of reliability than in Figure 15, above. (B) The population spike frequency repeats the behavior of the reliability and shows no modification for the direct activation (0-20 ms), while a statistically significant difference is found for the longer-term responses (30-50 ms). This behavior is consistent with the averaged results in the previous figure15. The error bars are the standard error of the mean, calculated for 10 control networks and 12 trained networks. (*) p-value <0.05; (**) p-value <0.001. Figure modified from (Hamilton et al., 2015).

Discussion

The steps outlined in this protocol provide sufficient detail for the beginner to plate his/her own neuronal cultures on MEAs and to record network activity. This

protocol will help to ensure that the cultures adhere properly, forming a carpet layer of cells over the electrode arrays, and remain healthy and contaminant-free for months.

Although it is best to adhere to all parts of the protocol, there are steps throughout the process that are critical to the successful outcome. The use of aseptic technique throughout the entire process is imperative to prevent the cultures from becoming contaminated. New MEAs must be made hydrophilic, as described in the protocol, or else poor cell adhesion will result. Avoiding harsh pipetting and the formation of air bubbles during dissociation will reduce the number of damaged cells plated and will lead to a higher and healthier yield. Switching from DMEM 5/5 to DMEM+ after the first feeding is also important. DMEM 5/5 contains horse serum, which will cause glial cells to dominate the culture if used continuously and will result in poor neuronal activity, although the cultures will appear healthy. Feeding the cultures as scheduled and keeping them in proper incubating conditions is also crucial.

Plating cell cultures on MEAs involves many variables that can lead to less-than-optimal results. Although the goal is a perfect "carpet" of cells, failure to address the critical steps mentioned above will result in poor cell maturation or in contamination. Poor cell adhesion, which is different from poor cell maturation, is also a concern. This can be caused by several factors, including poor MEA preparation prior to plating or the use of old medium. If old medium containing a stabilized form of L-glutamine and serum-free supplement for neural cell culture is used, the cells initially adhere but then float away after about two weeks. If bacterial contamination is a persistent problem, an antibiotic, such as ampicillin or pen-strep, can be added to the medium. There are also

fungicides available to treat fungal contamination. These are some of the more common variables that can affect the outcome of the cultures. There are many others that will only be encountered after time and experience.

In comparison to the use of glass microelectrodes, this technique is excellent for studying network dynamics and pharmacological responses. It enables the use of many different spatio-temporal stimulation patterns and allows for the recording of neuronal responses from multiple areas at once. Previous groups have demonstrated interesting results using protocols similar to the ones described here. Since the cultures last for weeks or months and the same cultures can be reused, this technique also allows for multiple experiments over time on the same network.

However, there are limitations to this technique. MEAs are non-invasive. Therefore, they can only record extracellular activity, as opposed to patch-clamping or intracellular recording with pipettes. Moreover, since each electrode in an array is covered by several cells, it is not possible to resolve the activity of a single neuron. Conversely, because these are in vitro cultures, they cannot fully reproduce the structural properties of networks in the brain. Also, activity can only be recorded for less than 30 min at a time without some mechanism providing a CO_2 atmosphere for the cells to maintain their pH balance.

Once this technique is mastered, pharmacological manipulations with or without electrical stimulation can be explored. New protocols to probe learning and memory formation in neuronal networks can also be designed and tested, along with protocols for hippocampal or spinal cord networks. Protocols for the stimulation and training of

networks have been previously published, and some of these were further developed into in vivo protocols, such as the "selective adaptation" proposed by (Eytan, Brenner, & Marom, 2003). Several protocols were tested. However, only results from a modification to the tetanus procedure proposed by (Ruaro et al., 2005) are presented here.

Table 3: PDL Preparation - List of Materials and Reagents.

Qty	Item
1	Autoclaved glass reagent bottle (at least 100 mL size)
20	15 mL sterile centrifuge tubes
1	10 mL sterile serological pipette
4	25 mL sterile serological pipette
2	50 mL sterile serological pipette
1	Centrifuge tube rack
150 mL	Sterile DI water
5 mg	Poly-D-lysine vial

Table 4: Laminin Preparation - List of Materials and Reagents.

Qty	Item
1	50 mL sterile centrifuge tubes
10	15 mL sterile centrifuge tubes
2	1 mL sterile serological pipette
2	50 mL sterile serological pipette
1	Centrifuge tube rack
1 mL	Phosphate buffer saline (PBS)
1 mg	Laminin

Table 5: Storage Medium Preparation - List of Materials and Reagents.

Qty	Item
1	Autoclaved glass reagent bottle (at least 100 mL size)
20	15 mL sterile centrifuge tubes
1	10 mL sterile serological pipette
4	25 mL sterile serological pipette

2	50 mL sterile serological pipette
1	Centrifuge tube rack
150 mL	Sterile DI water
5 mg	Poly-D-lysine vial

Table 6: DMEM 5/5 Medium Preparation - List of Materials and Reagents.

Qty	**Item**
44 mL	DMEM with a stablilzed form of L-glutamine (see table of materials)
1 mL	Serum-free supplement for neural cell culture (see table of materials)
2.5 mL	Horse serum
100 µL	Ascorbic acid [4 mg/mL]
2.5 mL	Fetal bovine serum (FBS)
0.5 mL	Pen strep (optional)
1	50 mL sterile centrifuge tubes
2	25 mL sterile serological pipette

2	10 mL sterile serological pipette
2	1 mL sterile serological pipette
1	250 mL filter

Table 7: DMEM+ Medium Preparation - List of Materials and Reagents.

Qty	**Item**
49 mL	DMEM with a stablilzed form of L-glutamine (see table of materials)
1 mL	Serum-free supplement for neural cell culture (see table of materials)
100 µL	Ascorbic acid [4 mg/mL]
0.5 mL	Pen strep (optional)
1	50 mL sterile centrifuge tubes
2	25 mL sterile serological pipette
2	1 mL sterile serological pipette
1	250 mL filter

Table 8: Cell Dissociation - List of Materials and Reagents.

Qty	Item
1	Papain 140 U/vial
1	Dnase 1,260 U/vial
7 mL	DMEM+ (chilled)
5 mL	DMEM 5/5 (warmed)
10 µL	Trypan blue
2	Scalpel blades
1	35 mm sterile Petri dish
4	15 mL sterile centrifuge tubes
2	5 mL sterile cryogenic tubes
2	2 mL sterile cryogenic tubes
1	50 mL sterile centrifuge tubes
1	microcentrifuge tube
2	Large bore transfer pipette
3	Small bore transfer pipette

5	2 mL sterile serological pipette
5	1 mL sterile serological pipette
2	10 μL sterile micropipette tips
1	1000 μL sterile micropipette tips
1	Hemocytometer chip

Disclosures

The authors have nothing to disclose.

Acknowledgments

This work was funded by the National Science Foundation grant CMMI-1300007. We would like to acknowledge previous lab members, who have helped with the design of these protocols and with the maintenance of the cultures for over five years at George Mason University: Dr. Joseph J. Pancrazio, Dr. Hamid Charkhkar, Dr. Gretchen Knaack, Dr. Franz Hamilton, Michael Maquera, and Robert Graham.

Contributions

Wrote Manuscript: Monica La Russa Gertz

Edited Manuscript: Nathalia Peixoto

Performed Dissection Protocols: Monica La Russa Gertz

Performed Stimulation Protocols: Zachary Baker

Performed Data Analysis: Sharon Jose

Citation: Gertz, M. L., Baker, Z., Jose, S., Peixoto, N. Time-dependent Increase in the Network Response to the Stimulation of Neuronal Cell Cultures on Micro-electrode Arrays. J. Vis. Exp. (123), e55726, doi:10.3791/55726 (2017).

REFERENCES

Ai, L., Mueller, J. K., Grant, A., Eryaman, Y., & Legon, W. (2016). Transcranial focused ultrasound for BOLD fMRI signal modulation in humans. In *Proceedings of the Annual International Conference of the IEEE Engineering in Medicine and Biology Society, EMBS* (Vol. 2016-Octob, pp. 1758–1761). Institute of Electrical and Electronics Engineers Inc. https://doi.org/10.1109/EMBC.2016.7591057

Airan, R. D., Meyer, R. A., Ellens, N. P. K., Rhodes, K. R., Farahani, K., Pomper, M. G., … Green, J. J. (2017). Noninvasive Targeted Transcranial Neuromodulation via Focused Ultrasound Gated Drug Release from Nanoemulsions. *Nano Letters*, *17*(2), 652–659. https://doi.org/10.1021/acs.nanolett.6b03517

Alonso, A., Reinz, E., Leuchs, B., Kleinschmidt, J., Fatar, M., Geers, B., … Meairs, S. (2013). Focal delivery of AAV2/1-transgenes into the rat brain by localized ultrasound-induced BBB opening. *Molecular Therapy - Nucleic Acids*, *2*, e73. https://doi.org/10.1038/mtna.2012.64

Amiez, C., Joseph, J. P., & Procyk, E. (2006). Reward encoding in the monkey anterior cingulate cortex. *Cerebral Cortex*, *16*(7), 1040–1055. https://doi.org/10.1093/cercor/bhj046

Ammann, D., Chao, P., & Simon, W. (1987). Valinomycin-based K+ selective microelectrodes with low electrical membrane resistance. *Neuroscience Letters*, *74*(2), 221–226. https://doi.org/10.1016/0304-3940(87)90153-4

Apfel, R. E., & Holland, C. K. (1991). Gauging the likelihood of cavitation from short-

pulse, low-duty cycle diagnostic ultrasound. *Ultrasound in Medicine and Biology*, *17*(2), 179–185. https://doi.org/10.1016/0301-5629(91)90125-G

Árnadóttir, J., & Chalfie, M. (2010). Eukaryotic Mechanosensitive Channels. *Annual Review of Biophysics*, *39*(1), 111–137. https://doi.org/10.1146/annurev.biophys.37.032807.125836

Bachtold, M. R., Rinaldi, P. C., Jones, J. P., Reines, F., & Price, L. R. (1998). Focused ultrasound modifications of neural circuit activity in a mammalian brain. *Ultrasound in Medicine and Biology*, *24*(4), 557–565. https://doi.org/10.1016/S0301-5629(98)00014-3

Baeza-Lehnert, F., Saab, A. S., Gutiérrez, R., Larenas, V., Díaz, E., Horn, M., … Barros, L. F. (2019). Non-Canonical Control of Neuronal Energy Status by the Na + Pump. *Cell Metabolism*, *29*(3), 668-680.e4. https://doi.org/10.1016/j.cmet.2018.11.005

Barros, L. F., Ruminot, I., San Martín, A., Lerchundi, R., Fernández-Moncada, I., & Baeza-Lehnert, F. (2020). Aerobic Glycolysis in the Brain: Warburg and Crabtree Contra Pasteur. *Neurochemical Research*. https://doi.org/10.1007/s11064-020-02964-w

Blackmore, J., Shrivastava, S., Sallet, J., Butler, C. R., & Cleveland, R. O. (2019). Ultrasound Neuromodulation: A Review of Results, Mechanisms and Safety. *Ultrasound in Medicine and Biology*, *45*(7), 1509–1536. https://doi.org/10.1016/j.ultrasmedbio.2018.12.015

Boyden, E. S. (2011, May 3). A history of optogenetics: The development of tools for controlling brain circuits with light. *F1000 Biology Reports*. Faculty of 1000 Ltd.

https://doi.org/10.3410/B3-11

Brohawn, S. G. (2015). How ion channels sense mechanical force: Insights from mechanosensitive K2P channels TRAAK, TREK1, and TREK2. *Annals of the New York Academy of Sciences, 1352*(1), 20–32. https://doi.org/10.1111/nyas.12874

Butson, C. R., & McIntyre, C. C. (2005). Tissue and electrode capacitance reduce neural activation volumes during deep brain stimulation. *Clinical Neurophysiology, 116*(10), 2490–2500. https://doi.org/10.1016/j.clinph.2005.06.023

Bystritsky, A., & Korb, A. S. (2015). A Review of Low-Intensity Transcranial Focused Ultrasound for Clinical Applications. *Current Behavioral Neuroscience Reports, 2*(2), 60–66. https://doi.org/10.1007/s40473-015-0039-0

Cesare, P., Moriondo, A., Vellani, V., & Mcnaughton, P. A. (1999). *Colloquium Paper This paper was presented at the National Academy of Sciences colloquium ’ ’The Neurobiology of Pain* (Vol. 96). Retrieved from www.pnas.org.

Chapman, R. A. (1967). Dependence on temperature of the conduction velocity of the action potential of the squid giant axon [39]. *Nature*. https://doi.org/10.1038/2131143a0

Choi, J. B., Lim, S. H., Cho, K. W., Kim, D. H., Jang, D. P., & Kim, I. Y. (2013). The effect of focused ultrasonic stimulation on the activity of hippocampal neurons in multi-channel electrode. In *International IEEE/EMBS Conference on Neural Engineering, NER* (pp. 731–734). https://doi.org/10.1109/NER.2013.6696038

Church, C. C., Labuda, C., & Nightingale, K. (2015). A Theoretical Study of Inertial Cavitation from Acoustic Radiation Force Impulse Imaging and Implications for the

Mechanical Index. *Ultrasound in Medicine and Biology*, *41*(2), 472–485. https://doi.org/10.1016/j.ultrasmedbio.2014.09.012

Colucci, V., Strichartz, G., Jolesz, F., Vykhodtseva, N., & Hynynen, K. (2009). Focused Ultrasound Effects on Nerve Action Potential in vitro. *Ultrasound in Medicine and Biology*, *35*(10), 1737–1747. https://doi.org/10.1016/j.ultrasmedbio.2009.05.002

Coussios, C. C., & Roy, R. A. (2008). Applications of acoustics and cavitation to noninvasive therapy and drug delivery. *Annual Review of Fluid Mechanics*, *40*, 395–420. https://doi.org/10.1146/annurev.fluid.40.111406.102116

Cressman, J. R., Ullah, G., Ziburkus, J., Schiff, S. J., & Barreto, E. (2009). The influence of sodium and potassium dynamics on excitability, seizures, and the stability of persistent states: I. Single neuron dynamics. *Journal of Computational Neuroscience*, *26*(2), 159–170. https://doi.org/10.1007/s10827-008-0132-4

Dalecki, D. (2004). Mechanical bioeffects of ultrasound. *Annual Review of Biomedical Engineering*. https://doi.org/10.1146/annurev.bioeng.6.040803.140126

DaSilva, A. F., Truong, D. Q., DosSantos, M. F., Toback, R. L., Datta, A., & Bikson, M. (2015). State-of-art neuroanatomical target analysis of high-definition and conventional tDCS montages used for migraine and pain control. *Frontiers in Neuroanatomy*, *9*(July), 89. https://doi.org/10.3389/fnana.2015.00089

Deffieux, T., Younan, Y., Wattiez, N., Tanter, M., Pouget, P., & Aubry, J. F. (2013). Low-intensity focused ultrasound modulates monkey visuomotor behavior. *Current Biology*, *23*(23), 2430–2433. https://doi.org/10.1016/j.cub.2013.10.029

Deng, Z.-D., Lisanby, S. H., & Peterchev, A. V. (2013). Controlling Stimulation Strength

and Focality in Electroconvulsive Therapy via Current Amplitude and Electrode Size and Spacing. *The Journal of ECT*, 1. https://doi.org/10.1097/yct.0b013e3182a4b4a7

Downs, M. E., Lee, S. A., Yang, G., Kim, S., Wang, Q., & Konofagou, E. E. (2018). Non-invasive peripheral nerve stimulation via focused ultrasound in vivo. *Physics in Medicine and Biology*, *63*(3), 035011. https://doi.org/10.1088/1361-6560/aa9fc2

Duck, F. A. (1997). The Meaning of Thermal Index (TI) and Mechanical Index (MI) Values. *BMUS Bulletin*, *5*(4), 36–40. https://doi.org/10.1177/1742271X9700500411

Duck, F. A. (2007, January 1). Medical and non-medical protection standards for ultrasound and infrasound. *Progress in Biophysics and Molecular Biology*. Pergamon. https://doi.org/10.1016/j.pbiomolbio.2006.07.008

Duck, F. A. (2008, December 1). Hazards, risks and safety of diagnostic ultrasound. *Medical Engineering and Physics*. Elsevier. https://doi.org/10.1016/j.medengphy.2008.06.002

Ellisman, M. H., Palmer, D. E., & André, M. P. (1987). Diagnostic levels of ultrasound may disrupt myelination. *Experimental Neurology*, *98*(1), 78–92. https://doi.org/10.1016/0014-4886(87)90073-2

Eytan, D., Brenner, N., & Marom, S. (2003). Selective adaptation in networks of cortical neurons. *The Journal of Neuroscience : The Official Journal of the Society for Neuroscience*, *23*(28), 9349–9356. https://doi.org/23/28/9349 [pii]

Fernández-Moncada, I., Ruminot, I., Robles-Maldonado, D., Alegría, K., Deitmer, J. W., & Barros, L. F. (2018). Neuronal control of astrocytic respiration through a variant

of the Crabtree effect. *Proceedings of the National Academy of Sciences of the United States of America*, *115*(7), 1623–1628. https://doi.org/10.1073/pnas.1716469115

Fettiplace, R., & Haydon, D. A. (1980). Water permeability of lipid membranes. *Physiological Reviews*. https://doi.org/10.1152/physrev.1980.60.2.510

Focused Ultrasound Foundation. (2016). An Overview of the Biological Effects of Focused Ultrasound. *Www.Fusfoundation.Org*, Accessed Jan. 5 2017. Retrieved from www.fusfoundation.org

Foley, J. L., Little, J. W., & Vaezy, S. (2008). Effects of high-intensity focused ultrasound on nerve conduction. *Muscle and Nerve*, *37*(2), 241–250. https://doi.org/10.1002/mus.20932

Franceschini, G., Bigoni, D., Regitnig, P., & Holzapfel, G. (2006). Brain tissue deforms similarly to filled elastomers and follows consolidation theory. *Journal of the Mechanics and Physics of Solids*, *54*, 2592–2620. Retrieved from https://graz.pure.elsevier.com/en/publications/brain-tissue-deforms-similarly-to-filled-elastomers-and-follows-c

Fry, F. J., Ades, H. W., & Fry, W. J. (1958). Production of reversible changes in the central nervous system by ultrasound. *Science*, *127*(3289), 83–84. https://doi.org/10.1126/science.127.3289.83

Fry, W. J., Barnard, J. W., Fry, F. J., Krumins, R. F., & Brennan, J. F. (1955, September 16). Ultrasonic lesions in the mammalian central nervous system. *Science*. American Association for the Advancement of Science.

https://doi.org/10.1126/science.122.3168.517

Fry, W. J., Wulff, V. J., Tucker, D., & Fry, F. J. (1950). Physical Factors Involved in Ultrasonically Induced Changes in Living Systems: I. Identification of Non-Temperature Effects. *Journal of the Acoustical Society of America*, *22*(6), 867–876. https://doi.org/10.1121/1.1906707

Fung, Y.-C. (1993). *Biomechanics*. New York, NY: Springer New York. https://doi.org/10.1007/978-1-4757-2257-4

Galford, J. E., & McElhaney, J. H. (1970). A viscoelastic study of scalp, brain, and dura. *Journal of Biomechanics*, *3*(2), 211–221. https://doi.org/10.1016/0021-9290(70)90007-2

Gavrilov, L. R., Gersuni, G. V., Ilyinski, O. B., Tsirulnikov, E. M., & Shchekanov, E. E. (1977). A study of reception with the use of focused ultrasound. I. Effects on the skin and deep receptor structures in man. *Brain Research*, *135*(2), 265–277. https://doi.org/10.1016/0006-8993(77)91030-7

Gavrilov, L. R., Gersuni, G. V., Ilyinsky, O. B., Tsirulnikov, E. M., & Shchekanov, E. E. (1977). A study of reception with the use of focused ultrasound. II. Effects on the animal receptor structures. *Brain Research*, *135*(2), 279–285. https://doi.org/10.1016/0006-8993(77)91031-9

Grossman, N., Bono, D., Dedic, N., Kodandaramaiah, S. B., Rudenko, A., Suk, H. J., … Boyden, E. S. (2017). Noninvasive Deep Brain Stimulation via Temporally Interfering Electric Fields. *Cell*, *169*(6), 1029-1041.e16. https://doi.org/10.1016/j.cell.2017.05.024

Gulick, D. W., Li, T., Kleim, J. A., & Towe, B. C. (2017). Comparison of Electrical and Ultrasound Neurostimulation in Rat Motor Cortex. *Ultrasound in Medicine and Biology*, *43*(12), 2824–2833. https://doi.org/10.1016/j.ultrasmedbio.2017.08.937

Guttman, R. (1966). Temperature characteristics of excitation in space-clamped squid axons. *The Journal of General Physiology*, *49*(5), 1007–1018. https://doi.org/10.1085/jgp.49.5.1007

Haar, G. Ter. (2010). Ultrasound bioeffects and safety. *Proceedings of the Institution of Mechanical Engineers, Part H: Journal of Engineering in Medicine*, *224*(2), 363–373. https://doi.org/10.1243/09544119JEIM613

Hakimova, H., Kim, S., Chu, K., Lee, S. K., Jeong, B., & Jeon, D. (2015). Ultrasound stimulation inhibits recurrent seizures and improves behavioral outcome in an experimental model of mesial temporal lobe epilepsy. *Epilepsy and Behavior*, *49*. https://doi.org/10.1016/j.yebeh.2015.04.008

Hameroff, S., Trakas, M., Duffield, C., Annabi, E., Gerace, M. B., Boyle, P., … Badal, J. J. (2013). Transcranial ultrasound (TUS) effects on mental states: A pilot study. *Brain Stimulation*, *6*(3), 409–415. https://doi.org/10.1016/j.brs.2012.05.002

Hamill, O. P., & Martinac, B. (2001). Molecular basis of mechanotransduction in living cells. *Physiological Reviews*. American Physiological Society. https://doi.org/10.1152/physrev.2001.81.2.685

Hamilton, F., Graham, R., Luu, L., Peixoto, N., Wagenaar, D., Madhavan, R., … Robinson, H. (2015). Time-Dependent Increase in Network Response to Stimulation. *PLOS ONE*, *10*(11), e0142399.

https://doi.org/10.1371/journal.pone.0142399

Han, S., Kim, M., Kim, H., Shin, H., & Youn, I. (2018). Ketamine Inhibits Ultrasound Stimulation-Induced Neuromodulation by Blocking Cortical Neuron Activity. *Ultrasound in Medicine and Biology*, *44*(3), 635–646. https://doi.org/10.1016/j.ultrasmedbio.2017.11.008

Harris, J. J., Jolivet, R., & Attwell, D. (2012, September 6). Synaptic Energy Use and Supply. *Neuron*. Neuron. https://doi.org/10.1016/j.neuron.2012.08.019

Hartmann, P., & Trettnak, W. (1996). Effects of polymer matrices on calibration functions of luminescent oxygen sensors on porphyrin ketone complexes. *Analytical Chemistry*, *68*(15), 2615–2620. https://doi.org/10.1021/ac960008k

Haswell, E. S., Phillips, R., & Rees, D. C. (2011, October 12). Mechanosensitive channels: What can they do and how do they do it? *Structure*. https://doi.org/10.1016/j.str.2011.09.005

Heinemann, S. H., Conti, F., Stühmer, W., & Neher, E. (1987). Effects of hydrostatic pressure on membrane processes: Sodium channels, calcium channels, and exocytosis. *Journal of General Physiology*, *90*(6), 765–778. https://doi.org/10.1085/jgp.90.6.765

Herrmann, C. S., Rach, S., Neuling, T., & Strüber, D. (2013). Transcranial alternating current stimulation: a review of the underlying mechanisms and modulation of cognitive processes. *Frontiers in Human Neuroscience*, *7*(MAY), 279. https://doi.org/10.3389/fnhum.2013.00279

Hinkle, P. C. (2005, January 7). P/O ratios of mitochondrial oxidative phosphorylation.

Biochimica et Biophysica Acta - Bioenergetics. Elsevier. https://doi.org/10.1016/j.bbabio.2004.09.004

Histed, M. H., Bonin, V., & Reid, R. C. (2009). Direct Activation of Sparse, Distributed Populations of Cortical Neurons by Electrical Microstimulation. *Neuron*, *63*(4), 508–522. https://doi.org/10.1016/j.neuron.2009.07.016

Hynynen, K., McDannold, N., Sheikov, N. A., Jolesz, F. A., & Vykhodtseva, N. (2005). Local and reversible blood-brain barrier disruption by noninvasive focused ultrasound at frequencies suitable for trans-skull sonications. *NeuroImage*, *24*(1), 12–20. https://doi.org/10.1016/j.neuroimage.2004.06.046

Ingram, J. M., Zhang, C., Xu, J., & Schiff, S. J. (2013). FRET excited ratiometric oxygen sensing in living tissue. *Journal of Neuroscience Methods*, *214*(1), 45–51. https://doi.org/10.1016/j.jneumeth.2013.01.002

Jiang, Q., Li, G., Zhao, H., Sheng, W., Yue, L., Su, M., … Zheng, H. (2018). Temporal neuromodulation of retinal ganglion cells by low-frequency focused ultrasound stimulation. *IEEE Transactions on Neural Systems and Rehabilitation Engineering*, *26*(5), 969–976. https://doi.org/10.1109/TNSRE.2018.2821194

Juan, E. J., González, R., Albors, G., Ward, M. P., & Irazoqui, P. (2014). Vagus nerve modulation using focused pulsed ultrasound: Potential applications and preliminary observations in a rat. *International Journal of Imaging Systems and Technology*, *24*(1), 67–71. https://doi.org/10.1002/ima.22080

Kamimura, H. A. S., Wang, S., Chen, H., Wang, Q., Aurup, C., Acosta, C., … Konofagou, E. E. (2016). Focused ultrasound neuromodulation of cortical and

subcortical brain structures using 1.9 MHz. *Medical Physics*, *43*(10), 5730–5735. https://doi.org/10.1118/1.4963208

Kamimura, H., Wang, S., Chen, H., Wang, Q., Aurup, C., Acosta, C., … Konofagou, E. (2015). Pupil dilation and motor response elicitation by ultrasound neuromodulation. In *2015 IEEE International Ultrasonics Symposium, IUS 2015*. Institute of Electrical and Electronics Engineers Inc. https://doi.org/10.1109/ULTSYM.2015.0070

Kawamata, T., Mori, T., Sato, S., & Katayama, Y. (2007). Tissue hyperosmolality and brain edema in cerebral contusion. *Neurosurgical Focus*. https://doi.org/10.3171/foc.2007.22.5.6

Khraiche, M. L., Phillips, W. B., Jackson, N., & Muthuswamy, J. (2008). Ultrasound induced increase in excitability of single neurons. In *Proceedings of the 30th Annual International Conference of the IEEE Engineering in Medicine and Biology Society, EMBS'08 - "Personalized Healthcare through Technology"* (Vol. 2008, pp. 4246–4249). IEEE Computer Society. https://doi.org/10.1109/iembs.2008.4650147

Kim, H. B., Swanberg, K. M., Han, H. S., Kim, J. C., Kim, J. W., Lee, S., … Park, J. H. (2017). Prolonged stimulation with low-intensity ultrasound induces delayed increases in spontaneous hippocampal culture spiking activity. *Journal of Neuroscience Research*, *95*(3), 885–896. https://doi.org/10.1002/jnr.23845

Kim, H., Chiu, A., Lee, S. D., Fischer, K., & Yoo, S. S. (2014a). Focused ultrasound-mediated non-invasive brain stimulation: Examination of sonication parameters. *Brain Stimulation*, *7*(5), 748–756. https://doi.org/10.1016/j.brs.2014.06.011

Kim, H., Chiu, A., Lee, S. D., Fischer, K., & Yoo, S. S. (2014b). Focused ultrasound-

mediated non-invasive brain stimulation: Examination of sonication parameters. *Brain Stimulation*, *7*(5), 748–756. https://doi.org/10.1016/j.brs.2014.06.011

King, R. L., Brown, J. R., Newsome, W. T., & Pauly, K. B. (2013). Effective parameters for ultrasound-induced in vivo neurostimulation. *Ultrasound in Medicine and Biology*, *39*(2), 312–331. https://doi.org/10.1016/j.ultrasmedbio.2012.09.009

King, R. L., Brown, J. R., & Pauly, K. B. (2014). Localization of ultrasound-induced invivo neurostimulation in the mouse model. *Ultrasound in Medicine and Biology*, *40*(7), 1512–1522. https://doi.org/10.1016/j.ultrasmedbio.2014.01.020

Koroleva, V. I., Vykhodtseva, N. I., & Elagin, V. A. (1986). Cortical and subcortical spreading depression in rats produced by focused ultrasound. *Neurophysiology*, *18*(1), 43–48. https://doi.org/10.1007/BF01052490

Kubanek, J., Shukla, P., Das, A., Baccus, S. A., & Goodman, M. B. (2018). Ultrasound elicits behavioral responses through mechanical effects on neurons and ion channels in a simple nervous system. *Journal of Neuroscience*, *38*(12), 3081–3091. https://doi.org/10.1523/JNEUROSCI.1458-17.2018

Lee, J. C. F., Callaway, J. C., & Foehring, R. C. (2005). Effects of temperature on calcium transients and Ca2+-dependent afterhyperpolarizations in neocortical pyramidal neurons. *Journal of Neurophysiology*, *93*(4), 2012–2020. https://doi.org/10.1152/jn.01017.2004

Lee, S., Lee, C., Park, J., & Im, C. H. (2020). Individually customized transcranial temporal interference stimulation for focused modulation of deep brain structures: a simulation study with different head models. *Scientific Reports*, *10*(1), 11730.

https://doi.org/10.1038/s41598-020-68660-5

Lee, W., Chung, Y. A., Jung, Y., Song, I. U., & Yoo, S. S. (2016). Simultaneous acoustic stimulation of human primary and secondary somatosensory cortices using transcranial focused ultrasound. *BMC Neuroscience, 17*(1), 68. https://doi.org/10.1186/s12868-016-0303-6

Lee, W., Kim, H. C., Jung, Y., Chung, Y. A., Song, I. U., Lee, J. H., & Yoo, S. S. (2016). Transcranial focused ultrasound stimulation of human primary visual cortex. *Scientific Reports, 6,* 34026. https://doi.org/10.1038/srep34026

Lee, W., Kim, H., Jung, Y., Song, I. U., Chung, Y. A., & Yoo, S. S. (2015). Image-guided transcranial focused ultrasound stimulates human primary somatosensory cortex. *Scientific Reports, 5,* 8743. https://doi.org/10.1038/srep08743

Lee, W., Lee, S. D., Park, M. Y., Foley, L., Purcell-Estabrook, E., Kim, H., … Yoo, S. S. (2016). Image-Guided Focused Ultrasound-Mediated Regional Brain Stimulation in Sheep. *Ultrasound in Medicine and Biology*, *42*(2), 459–470. https://doi.org/10.1016/j.ultrasmedbio.2015.10.001

Legon, W., Ai, L., Bansal, P., & Mueller, J. K. (2018). Neuromodulation with single-element transcranial focused ultrasound in human thalamus. *Human Brain Mapping*, *39*(5), 1995–2006. https://doi.org/10.1002/hbm.23981

Legon, W., Rowlands, A., Opitz, A., Sato, T. F., & Tyler, W. J. (2012). Pulsed Ultrasound Differentially Stimulates Somatosensory Circuits in Humans as Indicated by EEG and fMRI. *PLoS ONE, 7*(12). https://doi.org/10.1371/journal.pone.0051177

Legon, W., Sato, T. F., Opitz, A., Mueller, J., Barbour, A., Williams, A., & Tyler, W. J. (2014a). Transcranial focused ultrasound modulates the activity of primary somatosensory cortex in humans. *Nature Neuroscience*, *17*(2), 322–329. https://doi.org/10.1038/nn.3620

Legon, W., Sato, T. F., Opitz, A., Mueller, J., Barbour, A., Williams, A., & Tyler, W. J. (2014b). Transcranial focused ultrasound modulates the activity of primary somatosensory cortex in humans. *Nature Neuroscience*, *17*(2), 322–329. https://doi.org/10.1038/nn.3620

Lele, P. P. (1963). The effects of focused ultrasonic radiation on the peripheral nerves, with observations on local heating. *Ultrasonics*, *1*(4), III. https://doi.org/10.1016/0041-624x(63)90202-6

Li, G. F., Zhao, H. X., Zhou, H., Yan, F., Wang, J. Y., Xu, C. X., … Zheng, H. R. (2016). Improved Anatomical Specificity of Non-invasive Neuro-stimulation by High Frequency (5 MHz) Ultrasound. *Scientific Reports*, *6*. https://doi.org/10.1038/srep24738

Li, Y., Zhou, W., Li, X., Zeng, S., Liu, M., & Luo, Q. (2007). Characterization of synchronized bursts in cultured hippocampal neuronal networks with learning training on microelectrode arrays. *Biosensors & Bioelectronics*, *22*(12), 2976–2982. https://doi.org/10.1016/j.bios.2006.12.018

Lipsman, N., Mainprize, T. G., Schwartz, M. L., Hynynen, K., & Lozano, A. M. (2014). Intracranial Applications of Magnetic Resonance-guided Focused Ultrasound. *Neurotherapeutics*. Springer New York LLC. https://doi.org/10.1007/s13311-014-

0281-2

Martin, E., Werner, B., Bauer, R., van Leyen, K., Coluccia, D., & Fandino, J. (2014). Clinical neurological HIFU applications: the Zurich experience. *Translational Cancer Research*, *3*(5), 449–458. https://doi.org/10.21037/3156

Martinac, B. (2004). Mechanosensitive ion channels: Molecules of mechanotransduction. *Journal of Cell Science*, *117*(12), 2449–2460. https://doi.org/10.1242/jcs.01232

Mathiesen, C., Caesar, K., Thomsen, K., Hoogland, T. M., Witgen, B. M., Brazhe, A., & Lauritzen, M. (2011). Activity-dependent increases in local oxygen consumption correlate with postsynaptic currents in the mouse cerebellum in vivo. *Journal of Neuroscience*, *31*(50), 18327–18337. https://doi.org/10.1523/JNEUROSCI.4526-11.2011

McDannold, N., Arvanitis, C. D., Vykhodtseva, N., & Livingstone, M. S. (2012). Temporary disruption of the blood-brain barrier by use of ultrasound and microbubbles: Safety and efficacy evaluation in rhesus macaques. *Cancer Research*, *72*(14), 3652–3663. https://doi.org/10.1158/0008-5472.CAN-12-0128

Mehić, E., Xu, J. M., Caler, C. J., Coulson, N. K., Moritz, C. T., & Mourad, P. D. (2014a). Increased anatomical specificity of neuromodulation via modulated focused ultrasound. *PLoS ONE*, *9*(2). https://doi.org/10.1371/journal.pone.0086939

Mehić, E., Xu, J. M., Caler, C. J., Coulson, N. K., Moritz, C. T., & Mourad, P. D. (2014b). Increased anatomical specificity of neuromodulation via modulated focused ultrasound. *PLoS ONE*, *9*(2), e86939. https://doi.org/10.1371/journal.pone.0086939

Menz, M. D., Oralkan, O., Khuri-Yakub, P. T., & Baccus, S. a. (2013). Precise Neural Stimulation in the Retina Using Focused Ultrasound. *Journal of Neuroscience*, *33*(10), 4550–4560. https://doi.org/10.1523/JNEUROSCI.3521-12.2013

Menz, M., Ye, P., Firouzi, K., Pauly, K. B., Khuri-Yakub, B., & Baccus, S. (2017). Physical mechanisms of ultrasonic neurostimulation of the retina, 231449. https://doi.org/10.1101/231449

Menz, Michael D., Oralkan, Ö., Khuri-Yakub, P. T., & Baccus, S. A. (2013). Precise neural stimulation in the retina using focused ultrasound. *Journal of Neuroscience*, *33*(10), 4550–4560. https://doi.org/10.1523/JNEUROSCI.3521-12.2013

Menz, Mike D., Ye, P., Firouzi, K., Nikoozadeh, A., Pauly, K. B., Khuri-Yakub, P., & Baccus, S. A. (2019). Radiation Force as a Physical Mechanism for Ultrasonic Neurostimulation of the Ex Vivo Retina. *The Journal of Neuroscience : The Official Journal of the Society for Neuroscience*, *39*(32), 6251–6264. https://doi.org/10.1523/JNEUROSCI.2394-18.2019

Mihran, R. T., Barnes, F. S., & Wachtel, H. (1990). Temporally-specific modification of myelinated axon excitability in vitro following a single ultrasound pulse. *Ultrasound in Medicine and Biology*, *16*(3), 297–309. https://doi.org/10.1016/0301-5629(90)90008-Z

Min, B.-K., Bystritsky, A., Jung, K.-I., Fischer, K., Zhang, Y., Maeng, L.-S., … Yoo, S.-S. (2011). Focused ultrasound-mediated suppression of chemically-induced acute epileptic EEG activity. *BMC Neuroscience*, *12*(1), 23. https://doi.org/10.1186/1471-2202-12-23

Monti, M. M., Schnakers, C., Korb, A. S., Bystritsky, A., & Vespa, P. M. (2016, November 1). Non-Invasive Ultrasonic Thalamic Stimulation in Disorders of Consciousness after Severe Brain Injury: A First-in-Man Report. *Brain Stimulation*. Elsevier Inc. https://doi.org/10.1016/j.brs.2016.07.008

Mueller, J., Legon, W., Opitz, A., Sato, T. F., & Tyler, W. J. (2014). Transcranial focused ultrasound modulates intrinsic and evoked EEG dynamics. *Brain Stimulation*, *7*(6), 900–908. https://doi.org/10.1016/j.brs.2014.08.008

Ng, A., & Swanevelder, J. (2011). Resolution in ultrasound imaging. *Continuing Education in Anaesthesia, Critical Care & Pain*, *11*(5), 186–192. https://doi.org/10.1093/bjaceaccp/mkr030

Nightingale, K., Soo, M. S., Nightingale, R., & Trahey, G. (2002). Acoustic radiation force impulse imaging: In vivo demonstration of clinical feasibility. *Ultrasound in Medicine and Biology*, *28*(2), 227–235. https://doi.org/10.1016/S0301-5629(01)00499-9

Nitsche, M. A., Cohen, L. G., Wassermann, E. M., Priori, A., Lang, N., Antal, A., … Pascual-Leone, A. (2008, July 1). Transcranial direct current stimulation: State of the art 2008. *Brain Stimulation*. Elsevier Inc. https://doi.org/10.1016/j.brs.2008.06.004

Orr, A. W., Helmke, B. P., Blackman, B. R., & Schwartz, M. A. (2006, January). Mechanisms of mechanotransduction. *Developmental Cell*. https://doi.org/10.1016/j.devcel.2005.12.006

Owen, J. A., Barreto, E., & Cressman, J. R. (2013). Controlling Seizure-Like Events by

Perturbing Ion Concentration Dynamics with Periodic Stimulation. *PLoS ONE*, *8*(9), e73820. https://doi.org/10.1371/journal.pone.0073820

Palmeri, M. L., & Nightingale, K. R. (2011). Acoustic radiation force-based elasticity imaging methods. *Interface Focus*, *1*(4), 553–564. https://doi.org/10.1098/rsfs.2011.0023

Perkins, K. L., Arranz, A. M., Yamaguchi, Y., & Hrabetova, S. (2017). Brain extracellular space, hyaluronan, and the prevention of epileptic seizures. *Reviews in the Neurosciences*, *28*(8), 869–892. https://doi.org/10.1515/revneuro-2017-0017

Perlmutter, J. S., & Mink, J. W. (2006). Deep brain stimulation. *Annual Review of Neuroscience*. https://doi.org/10.1146/annurev.neuro.29.051605.112824

Plesset, M. S., & Prosperetti, A. (1977). Bubble Dynamics and Cavitation. *Annual Review of Fluid Mechanics*, *9*(1), 145–185. https://doi.org/10.1146/annurev.fl.09.010177.001045

Polanía, R., Nitsche, M. A., & Ruff, C. C. (2018, February 1). Studying and modifying brain function with non-invasive brain stimulation. *Nature Neuroscience*. Nature Publishing Group. https://doi.org/10.1038/s41593-017-0054-4

Prieto, M. L., Oralkan, Ö., Khuri-Yakub, B. T., & Maduke, M. C. (2013). Dynamic Response of Model Lipid Membranes to Ultrasonic Radiation Force. *PLoS ONE*, *8*(10), e77115. https://doi.org/10.1371/journal.pone.0077115

Reed, T., & Cohen Kadosh, R. (2018, November 2). Transcranial electrical stimulation (tES) mechanisms and its effects on cortical excitability and connectivity. *Journal of Inherited Metabolic Disease*. Springer Netherlands. https://doi.org/10.1007/s10545-

018-0181-4

Rehni, A. K., & Dave, K. R. (2018, December 1). Impact of Hypoglycemia on Brain Metabolism During Diabetes. *Molecular Neurobiology*. Humana Press Inc. https://doi.org/10.1007/s12035-018-1044-6

Rossi, S., Hallett, M., Rossini, P. M., Pascual-Leone, A., Avanzini, G., Bestmann, S., … Ziemann, U. (2009, December 1). Safety, ethical considerations, and application guidelines for the use of transcranial magnetic stimulation in clinical practice and research. *Clinical Neurophysiology*. Elsevier. https://doi.org/10.1016/j.clinph.2009.08.016

Ruaro, M. E., Bonifazi, P., & Torre, V. (2005). Toward the neurocomputer: image processing and pattern recognition with neuronal cultures. *IEEE Transactions on Bio-Medical Engineering*, *52*(3), 371–383. https://doi.org/10.1109/TBME.2004.842975

Sanguinetti, J. L., Hameroff, S., Smith, E. E., Sato, T., Daft, C. M. W., Tyler, W. J., & Allen, J. J. B. (2020). Transcranial Focused Ultrasound to the Right Prefrontal Cortex Improves Mood and Alters Functional Connectivity in Humans. *Frontiers in Human Neuroscience*, *14*. https://doi.org/10.3389/fnhum.2020.00052

Sheikov, N., McDannold, N., Sharma, S., & Hynynen, K. (2008). Effect of Focused Ultrasound Applied With an Ultrasound Contrast Agent on the Tight Junctional Integrity of the Brain Microvascular Endothelium. *Ultrasound in Medicine and Biology*, *34*(7), 1093–1104. https://doi.org/10.1016/j.ultrasmedbio.2007.12.015

Silver, I. A., & Erecinska, M. (1994). Extracellular glucose concentration in mammalian

brain: Continuous monitoring of changes during increased neuronal activity and upon limitation in oxygen supply in normo-, hypo-, and hyperglycemic animals. *Journal of Neuroscience*, *14*(8), 5068–5076. https://doi.org/10.1523/jneurosci.14-08-05068.1994

Simonova, Z., Svoboda, J., Orkand, P., Bernard, C., Lassmann, H., & Sykova, E. (1996). *Changes of Extracellular Space Volume and Tortuosity in the Spinal Cord of Lewis Rats With Experimental Autoimmune Encephalomyelitis*. *Physiol. Res* (Vol. 45).

Syeda, R., Florendo, M. N., Cox, C. D., Kefauver, J. M., Santos, J. S., Martinac, B., & Patapoutian, A. (2016). Piezo1 Channels Are Inherently Mechanosensitive. *Cell Reports*, *17*(7), 1739–1746. https://doi.org/10.1016/j.celrep.2016.10.033

Terney, D., Chaieb, L., Moliadze, V., Antal, A., & Paulus, W. (2008). Increasing Human Brain Excitability by Transcranial High-Frequency Random Noise Stimulation. *Journal of Neuroscience*, *28*(52), 14147–14155. https://doi.org/10.1523/JNEUROSCI.4248-08.2008

Thomas, C. R., Farny, C. H., Coussios, C. C., Roy, R. A., & Holt, R. G. (2005). Dynamics and control of cavitation during high-intensity focused ultrasound application. *Acoustics Research Letters Online*, *6*(3), 182–187. https://doi.org/10.1121/1.1901744

Thompson, S. M., Masukawa, L. M., & Prince, D. A. (1985). Temperature dependence of intrinsic membrane properties and synaptic potentials in hippocampal CA1 neurons in vitro. *Journal of Neuroscience*, *5*(3), 817–824. https://doi.org/10.1523/jneurosci.05-03-00817.1985

Tian, G. F., & Baker, A. J. (2000). Glycolysis prevents anoxia-induced synaptic transmission damage in rat hippocampal slices. *Journal of Neurophysiology*, *83*(4), 1830–1839. https://doi.org/10.1152/jn.2000.83.4.1830

Treat, L. H., McDannold, N., Vykhodtseva, N., Zhang, Y., Tam, K., & Hynynen, K. (2007). Targeted delivery of doxorubicin to the rat brain at therapeutic levels using MRI-guided focused ultrasound. *International Journal of Cancer*, *121*(4), 901–907. https://doi.org/10.1002/ijc.22732

Tsui, P. H., Wang, S. H., & Huang, C. C. (2005). In vitro effects of ultrasound with different energies on the conduction properties of neural tissue. *Ultrasonics*, *43*(7), 560–565. https://doi.org/10.1016/j.ultras.2004.12.003

Tufail, Y., Matyushov, A., Baldwin, N., Tauchmann, M. L., Georges, J., Yoshihiro, A., … Tyler, W. J. (2010). Transcranial Pulsed Ultrasound Stimulates Intact Brain Circuits. *Neuron*, *66*(5), 681–694. https://doi.org/10.1016/j.neuron.2010.05.008

Tyler, W. J. (2011). Noninvasive neuromodulation with ultrasound? A continuum mechanics hypothesis. *The Neuroscientist : A Review Journal Bringing Neurobiology, Neurology and Psychiatry*, *17*(1), 25–36. https://doi.org/10.1177/1073858409348066

Tyler, W. J. (2012). The mechanobiology of brain function. *Nature Reviews. Neuroscience*, *13*(12), 867–878. https://doi.org/10.1038/nrn3383

Tyler, W. J., Tufail, Y., Finsterwald, M., Tauchmann, M. L., Olson, E. J., & Majestic, C. (2008a). Remote excitation of neuronal circuits using low-intensity, low-frequency ultrasound. *PLoS ONE*, *3*(10). https://doi.org/10.1371/journal.pone.0003511

Tyler, W. J., Tufail, Y., Finsterwald, M., Tauchmann, M. L., Olson, E. J., & Majestic, C. (2008b). Remote excitation of neuronal circuits using low-intensity, low-frequency ultrasound. *PLoS ONE*, *3*(10). https://doi.org/10.1371/journal.pone.0003511

Wahab, R. A., Choi, M., Liu, Y., Krauthamer, V., Zderic, V., & Myers, M. R. (2012). Mechanical bioeffects of pulsed high intensity focused ultrasound on a simple neural model. *Medical Physics*, *39*(7), 4274–4283. https://doi.org/10.1118/1.4729712

Walsh, V., & Cowey, A. (2000). Transcranial magnetic stimulation and cognitive neuroscience. *Nature Reviews Neuroscience*, *1*(1), 73–80. https://doi.org/10.1038/35036239

Wang, T. R., Dallapiazza, R., & Elias, W. J. (2015). Neurological applications of transcranial high intensity focused ultrasound. *International Journal of Hyperthermia*, *31*(3), 285–291. https://doi.org/10.3109/02656736.2015.1007398

Wattiez, N., Constans, C., Deffieux, T., Daye, P. M., Tanter, M., Aubry, J. F., & Pouget, P. (2017). Transcranial ultrasonic stimulation modulates single-neuron discharge in macaques performing an antisaccade task. *Brain Stimulation*, *10*(6), 1024–1031. https://doi.org/10.1016/j.brs.2017.07.007

Watts, M. E., Pocock, R., & Claudianos, C. (2018, June 22). Brain energy and oxygen metabolism: Emerging role in normal function and disease. *Frontiers in Molecular Neuroscience*. Frontiers Media S.A. https://doi.org/10.3389/fnmol.2018.00216

Wheaton, W. W., & Chandel, N. S. (2011, March). Hypoxia. 2. Hypoxia regulates cellular metabolism. *American Journal of Physiology - Cell Physiology*. American Physiological Society. https://doi.org/10.1152/ajpcell.00485.2010

Wright, C. J., Rothwell, J., & Saffari, N. (2015). Ultrasonic stimulation of peripheral nervous tissue: An investigation into mechanisms. In *Journal of Physics: Conference Series* (Vol. 581, p. 012003). Institute of Physics Publishing. https://doi.org/10.1088/1742-6596/581/1/012003

Wright, Christopher J., Haqshenas, S. R., Rothwell, J., & Saffari, N. (2017). Unmyelinated Peripheral Nerves Can Be Stimulated in Vitro Using Pulsed Ultrasound. *Ultrasound in Medicine and Biology*, *43*(10), 2269–2283. https://doi.org/10.1016/j.ultrasmedbio.2017.05.008

Ye, P. P., Brown, J. R., & Pauly, K. B. (2016). Frequency dependence of ultrasound neurostimulation in the mouse brain. *Ultrasound in Medicine and Biology*, *42*(7), 1512–1530. https://doi.org/10.1016/j.ultrasmedbio.2016.02.012

Yoo, S. S., Kim, H., Min, B. K., Franck, E., & Park, S. (2011). Transcranial focused ultrasound to the thalamus alters anesthesia time in rats. *NeuroReport*, *22*(15), 783–787. https://doi.org/10.1097/WNR.0b013e32834b2957

Younan, Y., Deffieux, T., Larrat, B., Fink, M., Tanter, M., & Aubry, J.-F. (2013a). Influence of the pressure field distribution in transcranial ultrasonic neurostimulation. *Medical Physics*, *40*(8), 082902. https://doi.org/10.1118/1.4812423

Younan, Y., Deffieux, T., Larrat, B., Fink, M., Tanter, M., & Aubry, J. F. (2013b). Influence of the pressure field distribution in transcranial ultrasonic neurostimulation. *Medical Physics*, *40*(8), 082902. https://doi.org/10.1118/1.4812423

Young, R. R., & Henneman, E. (1961). Functional effects of focused ultrasound on mammalian nerves. *Science*, *134*(3489), 1521–1522. https://doi.org/10.1126/science.134.3489.1521

Zangen, A., Roth, Y., Voller, B., & Hallett, M. (2005). Transcranial magnetic stimulation of deep brain regions: Evidence for efficacy of the H-Coil. *Clinical Neurophysiology*, *116*(4), 775–779. https://doi.org/10.1016/j.clinph.2004.11.008

BIOGRAPHY

Monica La Russa Gertz graduated from Madonna Academy in 1985. She dropped out of college to raise her daughter in 1989. She began working for Enterprise Rent-A-Car in 1995 as a part-time file clerk and left the company as a corporate manager in Marketing and Communications in 2005 to return to school. She received her Bachelor of Science in chemistry from George Mason University in 2011. She started the Ph.D. program in neuroscience at GMU in 2013 and became a candidate in 2015. She was the first winner of the NSF Graduate Research Fellowship in the history of GMU and was selected as an "Outstanding Student" by the College of Science. She was president of the GMU Neuroscience Graduate Student Organization where she hosted several events. In 2018, she participated in an internship at Weill Cornell Medical College which resulted in a NASA publication and a position as a postdoctoral associate in the department of genetic medicine.

Gertz ML, Chin C, Tomoiaga D, MacKay M, Chang C, Butler D, Afshinnekoo E, Bezdan D, Schmidt M, Mozary C, Melnick A, Garrett-Bakelman F, Crucian B, Lee S, Zwart SR, Smith SM, Meydan C, Mason CE, Multi-omic, Single-Cell, and Biochemical Profiles of Astronauts Guide Pharmacological Strategies for Returning to Gravity. Cell Reports. (In Press) https://doi.org/10.1016/j.celrep.2020.108429.

Gertz ML, Baker Z, Jose S, Peixoto N. Time-dependent Increase in the Network Response to the Stimulation of Neuronal Cell Cultures on Micro-electrode Arrays. J Vis Exp. 2017 May 29; (123):55726. doi: 10.3791/55726. PMID: 28605385; PMCID: PMC5608154. https://pubmed.ncbi.nlm.nih.gov/28605385/

Cressman JR, Drown C, Gertz ML, Ionic Imbalance, Clinical and Genetic Aspects of Epilepsy. INTECH Open Access Publisher. 2011 ISBN: 978-953-307-700-0. DOI: 10.5772/1138

Jawaid S, Gertz M, Corsino C, Cheung J, Seidle H, Couch RD. Human hydroxymethylglutaryl-coenzyme A reductase (HMGCR) and statin sensitivity. Indian J Biochem Biophys. 2010 Dec;47(6):331-9. PMID: 21355415. https://pubmed.ncbi.nlm.nih.gov/21355415/